Process Studies on the Generation of Near-Inertial Internal Gravity Waves by Wind

Georg Sebastian Voelker

University of Bremen, February 2017

The work for this thesis was supervised by

Dr. Maren Walter
Prof. PhD Bruce R. Sutherland
Prof. Dr. Dirk J. Olbers
Prof. PhD Paul G. Myers
Dr. Christian Mertens

This thesis was supported by the Deutsche Forschungsgemeinschaft (DFG) through the International Research Training Group "Processes and impacts of climate change in the North Atlantic Ocean and the Canadian Arctic" (IRTG 1904 ArcTrain).

Abstract

The generation of internal gravity waves in the ocean associated to wind stress forcing is studied with the aid of two numerical models. In a non-linear, axisymmetric and Boussinesq model the response to an idealized stationary wind stress pulse is investigated. The major generation mechanisms for internal gravity waves, inertial pumping, excites radially outward propagating low mode wave packets. The energy radiated relative to the wind work is found to be only about 0.02 %, which is $2-3$ orders of magnitude lower than generally observed.

In addition to the detailed axisymmetric simulation, a simplified hybrid slab model based on the classical slab model of Pollard and Millard (1970) is considered. In particular, the inertial pumping resulting from the divergent, horizontal, near-inertial response of the surface slab is regarded the boundary condition to the internal gravity wave field below the mixed layer. In a set of idealized experiments, laterally moving wind stress fronts are the most efficient driver for vertical motion depending on their translation speed. The application of the hybrid slab model to the North Atlantic for the years 1989 and 1996 as examples of opposite phases of the North Atlantic Oscillation shows latitude bands with characteristic ratio of energy radiated as internal gravity waves to the wind work. These are partly associated to the wind field structure in these meridional regimes. The ratio of total energies transferred equals to 9 % for both years.

In an application of the hybrid slab model to the axisymmetric setup it is found that the structure of the inertial oscillations of the axisymmetric simulation are well reproduced. However, the near-inertial response of the hybrid slab model has an 8 times larger amplitude and does not include non-linear effects. The ratio of radiated energy to the wind work for the stationary storm estimated with the hybrid slab model is about 1 %. This ratio is increased by a factor 30 when the same wind stress structure is moving across the domain with $21\,\mathrm{km\,h^{-1}}$.

Contents

1 Introduction **9**

2 An Axisymmetric Storm **15**

2.1 Model Description 15

2.1.1 Mathematical Formulation 15

2.1.2 Boundary Conditions and Background State 18

2.1.3 A Geostrophic Adjustment Process 19

2.1.4 Energetics of the System 23

2.2 Results and Discussion 26

2.2.1 Description of the The Control Run 26

2.2.2 Effects of the Surface Forcing Parameters 27

2.2.3 Geostrophic Adjustment of the Vortex 28

2.2.4 Internal Gravity Waves 30

2.2.5 Energetics 32

2.3 Summary and Conclusion 36

3 The Slab Model and the Hybrid Extension **39**

3.1 Description of Slab- and Hybrid Model 39

3.1.1 The Slab Model 39

3.1.2 Basic Properties of the Classical Slab Model 41

3.1.3 The Hybrid Solution 42

3.2 Data and Input Parameters 44

3.2.1 Wind Stress, Mixed Layer Depth and Buoyancy Data . . 44

3.2.2 The Damping Parameter r and the horizontal wavelength L_{h} 46

3.3 Results 46

3.3.1 Idealized Simulations 46

3.3.2 Simulations of the North Atlantic 49

3.4 Discussion 53

3.4.1 Meridional Regimes 53

3.4.2 The Two Years 57

3.4.3 Comparison to Previous Studies 58
3.5 Summary and Conclusions 59

4 Response of the Hybrid Model to a Cyclone 63
4.1 The Hybrid Model Setup 63
4.1.1 The Stationary, Axisymmetric Storm 65
4.1.2 The Moving Cyclone 66
4.2 Comparison of the two Models 66
4.3 The Influence of the Lateral Movement of the Storm 70
4.4 Conclusions 73

5 Outlook: 10 Years of Global Internal Wave Climate 75
5.1 Input Data and Model Setup 76
5.2 10 Years of Global Simulation 77
5.3 A New Approach to the Horizontal Length Scale 81
5.4 Conclusions 82

6 Summary and Conclusions 83

A Appendix to the Axisymmetric Simulation 89
A.1 A 4^{th} Order Wave Number Cutoff Filter 89

B Appendix to the Hybrid Model 91
B.1 Derivation of the Hybrid Slab Model (D. J. Olbers) 91
B.2 Technical Details of the Hybrid Slab Model Implementation . . 94
B.3 Design of the Fourier Filter in the Hybrid Model 97

Acknowledgments

There are many people who supported me and helped in the course of writing this thesis. First of all, I would like to thank Maren Walter and Christian Mertens for their guidance from the first to the last day. Their support is the foundation this thesis is build on. Very much appreciated is the help of Paul G. Myers and Bruce R. Sutherland who co-supervised my work over great distances. Moreover, they hosted me in Edmonton, Canada for a three months period. For that, I am particularly grateful. Also, I would like to thank Dirk Olbers for advice, fruitful discussions and for providing the material placed in the appendix. Furthermore, I would like to thank Janna Koehler for her support.

Last but not least, I wish to thank all members of the graduate school ArcTrain, both in Germany and Canada, for plenty of discussion, feedback and encouragement throughout the years.

Chapter 1

Introduction

One of the most striking features of the physics of the ocean is the generally stable stratification. Only small regions with weak density gradients allow for a vertical convection to great depths (Marshall and Schott, 1999). But how is that possible? If there are hot spots of convection in polar regions where cooled water becomes very dense and sinks to great depths, why does it not gradually fill up the "global bathtub" with cold water? The reduction of potential energy by this overturn must be balanced by some process continuously supplying energy to the global abyssal ocean.

The ocean's energy balance is characterized by a myriad of processes leading to an exchange of energy across all spatial and temporal scales. The winds, tidal motion, heat exchange with the atmosphere, evaporation and precipitation, geothermal heating as well as the variation of the atmospheric pressure supply energy to the ocean's reservoirs. These are the general circulation, mesoscale eddies, surface waves, the internal tides and internal waves (Fig. 1.1). Ultimately, this network of energy exchanges leads to turbulence and mixing of the ocean maintaining the ocean stratification (Wunsch and Ferrari, 2004).

In this context, the kinematic ocean response to the wind is a recurring subject of investigation. One of the earliest studies on the topic was the description of the ocean surface response to a steady wind stress formulated by Ekman (1905). 42 years later, Sverdrup formulated his well known theory on "Wind Driven Currents In A Baroclinic Ocean" (Sverdrup, 1947). Soon after, Stommel (1948) and Munk (1950) drew a picture of the wind driven circulation including the formation of gyres and western boundary currents. These milestones laid the foundation for the understanding of the role of the wind for the large scale ocean circulation. Another particular feature of the ocean response to the wind is the inertial oscillation - a nearly circular motion that is induced

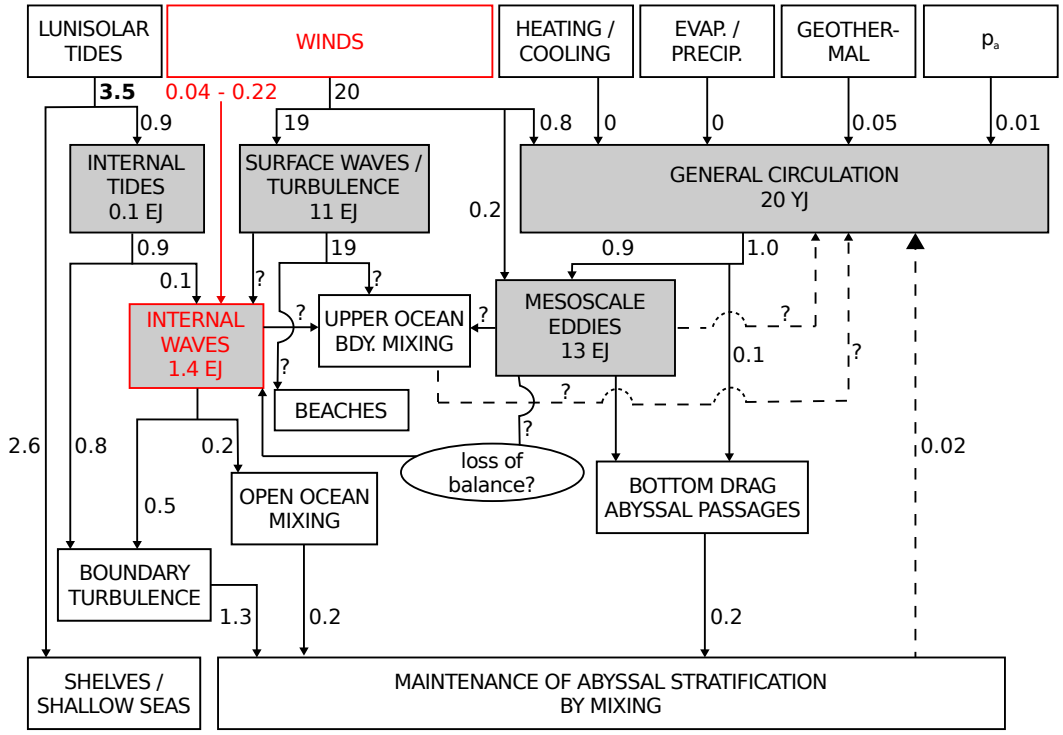

Figure 1.1: Overview of the energy sources (top), reservoirs (gray) and sinks in the ocean, adapted from Wunsch and Ferrari (2004). Energies are given in units of yottajoules $1\,\mathrm{YJ} = 10^{24}\,\mathrm{J}$ and exajoules $1\,\mathrm{EJ} = 10^{18}\,\mathrm{J}$. Fluxes between the boxes are in units of terrawatts $1\,\mathrm{TW} = 10^{12}\,\mathrm{W}$. All numbers are crude approximations and may have errors up to a factor of 10. The only accurate number is the tidal input of 3.5 TW (Munk and Wunsch, 1998). The internal wave energy is modified after (Thorpe, 2005), the wind power transferred to the internal gravity wave compartment shows 20% of the lowest and highest value estimated by Rimac et al. (2013).

when an initially accelerated water parcel is deflected by the Coriolis force. Currents at the surface but also within the stratified ocean were observed to oscillate with frequencies close to the Coriolis frequency f (Pollard, 1970). Pollard notes that in many observations the motion with the inertial frequency at the surface and at greater depths were correlated to the winds. Leaman and Sanford (1975), Leaman (1976) and Kundu (1976) found evidence of upward propagating phases with the inertial frequency in stratified environments and concluded that they observed internal gravity waves (IGWs).

Internal gravity waves are an oscillatory motion that results from vertical displacement of water parcels in a stratified environment. In particular, the two restoring forces, gravity (downward) and buoyancy (upward), result in a motion very much like a harmonic oscillator. The characteristic frequency to this

process is the buoyancy frequency $N = (-g/\rho_0 \partial\bar{\rho}/\partial z)^{\frac{1}{2}}$ which is the square root of the vertical gradient of the background density $\bar{\rho}$ multiplied by the gravitational constant g and normalized with a reference density ρ_0. IGWs can not exist at frequencies higher than or equal to N. Since this constraint is related to the local stratification it also implies spatial constraints e.g. where the density gradient is small or depth dependent. Additionally, the Earth's rotation, i.e. the presence of the Coriolis force, leads to the deflection of water parcels affected by an IGW. For frequencies smaller than N the almost purely vertical motion of the parcel changes to an elliptical trajectory and approaches the horizontal inertial oscillation as the frequency approaches the local Coriolis frequency f. Rotation therefore puts a second constraint as IGWs can not exist with frequencies smaller or equal to f.

Two of the most important properties of IGWs are that first, the angle of the group velocity with respect to the vertical depends on their frequency, the local Coriolis frequency and the local buoyancy frequency only. Second, their phase velocity is perpendicular to the group velocity. A downward radiating wave packet has therefore an upward propagating phase (Leaman and Sanford, 1975). Garrett and Munk (1972) found a theoretical description of the internal wave spectrum that was later proven to be applicable in a wide range of contexts and has been called universal many times (e.g. Lvov et al., 2004).

Internal gravity waves are one phenomenon of many occurring in the ocean. They generally have small amplitudes being overlaid by many other kinds of motion. Moreover, they are subject to complex 3-dimensional structure, interactions or generation mechanisms. Therefore, the modeling of IGWs is commonly used to isolate them from other motion or to isolate particular effects from others.

In general, the modeling of fluid dynamical systems is one of the most commonly used techniques in modern geophysical research. There are numerous possibilities on how to set up and run simulations - in particular with the computational power increasing rapidly (Griffies et al., 2000). Decisions on the complexity of the physics covered by the underlying equations, the horizontal and vertical discretization, parameterization of unresolved processes below the grid scale and many more have to be made (Griffies, 2004; Haidvogel and Beckmann, 1999). The result is a large number of distinct models each with its own strengths and weaknesses. General ocean circulation models may aim to reproduce the ocean, atmosphere or both locally or globally as close to nature

as possible. When simulating time series from decades to centennials or even millennia in a global setup - usually with reduced resolution - we often speak of climate models. They are base to all climate predictions, e.g. as published in the fifth IPCC assessment report (IPCC Working Group 1, 2014). In contrast to these, one might want to isolate a particular process in a simulation by approximating the governing equations of the model correspondingly. The techniques presented in this thesis include two numerical models distinct in their complexity and application - a non-linear axisymmetric simulation and a hybrid slab model. In order to put the two modeling approaches into context with each other, these are compared after being applied to the same scenario. Additionally, this allows for the identification of potential weaknesses by finding discrepancies between the model results.

Atmospheric structures with spatial scales between 5 km and 1000 km have been observed to be of great importance to climate and the ocean circulation (Condron and Renfrew, 2012; Jung et al., 2014). Also, the generation of near-inertial IGWs has been observed to be greatly impacted (Simmons and Alford, 2012). Many observations and simulations of individual moving cyclones, in particular hurricanes and typhoons, have been performed characterizing many aspects of the storm-ocean interaction (Price, 1981, 1983; Sanford et al., 1987; Shay et al., 1992; Firing et al., 1997; Prasad and Hogan, 2007; Sanford et al., 2007; Tsai et al., 2008; Zedler, 2009; Sanford et al., 2011). A special property of these storms is their almost cylindrical symmetry. Following on that, many experimental and theoretical studies with axisymmetric geometry were performed (e.g. Rotunno and Emanuel, 1987). The interaction of the ocean surface with the atmosphere is one of the key aspects (Emanuel, 1986).

Aiming at the characterization the internal generation of IGWs below but independent of the movement of the storm, simulations are performed using the fully non-linear, Boussinesq and axisymmetric Navier-Stokes equation. The action of the storm above the ocean is considered in a parameterization of the vertical momentum flux through the surface. Due to the ocean being at rest initially, this setup is closely related to the axisymmetric spin up of a stratified fluid (Duck and Foster, 2001; Moulin and Flór, 2004). At later model times, the ocean evolution can be considered a geostrophic adjustment process towards an equilibrated vortex. A theoretical analysis of the geostrophic adjustment process related to an axisymmetric vortex was done by Schubert et al. (1980). In contrast to previous considerations, the energy transferred to IGWs is measured directly from the simulations in the model presented here.

Moreover, the linear and non-linear processes during the transient adjustment phase, i.e. the generation processes for radiated IGWs are identified.

In order to reproduce and interpret their observations of inertial motions in the ocean surface mixed layer, Pollard and Millard (1970) introduced the so called slab model and simulated the inertial oscillations induced close to the surface. This model predicts the local near-inertial response of the vertically integrated velocity of the mixed layer using the wind stress as a forcing and a Rayleigh damping as a simplified sink of energy. D'Asaro (1985) extended the model by subtracting a time dependent Ekman component to isolate the inertial response. Taking into account the spectral solution method suggested by Alford (2001) this formulation is an often applied model. Its use ranges from comparison with and interpretation of local measurements (Pollard and Millard, 1970; Kundu, 1976; Käse and Olbers, 1980; Fu, 1981; Weller, 1982; D'Asaro, 1985; Paduan et al., 1989; Levine and Zervakis, 1995; Alford and Gregg, 2001; Pinkel, 2005; Plueddemann and Farrar, 2006; Chaigneau et al., 2008; Alford et al., 2013) to estimates of the global wind work (Alford, 2001; Watanabe and Hibiya, 2002; Furuichi et al., 2008). The formulation of a frequency dependent attenuation of the induced surface motion has received little attention so far (Alford, 2003; Alford et al., 2012).

More recent applications have benefited from satellite observations and reanalysis products to estimate a global wind stress forcing in the ocean (Alford, 2001; Watanabe and Hibiya, 2002; Furuichi et al., 2008). Also, satellite supported measurements contain spectral information about the wind stress (Gille, 2005). Direct estimates of the Rayleigh damping parameter needed as an assumption for the slab model can be obtained from satellite tracked drifter trajectories (Park et al., 2009). Likewise, this study relies on reanalysis products and the characterization of the wind forcing and the ocean response based on remote sensing techniques.

Olbers et al. (2012) proposed to use the slab model as a boundary condition to a stratified layer underneath the surface mixed layer to estimate the energy flux radiated as IGWs. In particular inertial pumping velocities (Gill, 1984), i.e. vertical velocities at the base of the mixed layer, are derived from a grid of point wise calculated slab model results. Their lateral structure and magnitude are combined with the local buoyancy frequency at the mixed layer base to obtain an estimate of the radiation energy flux from the mixed layer base into the deep ocean. In contrast to previous formulations, this method

allows for quantification of the radiation energy flux from the mixed layer into the internal wave field of the stratified ocean below. However, assumptions on the horizontal wave number spectrum as well as the local buoyancy frequency at the mixed layer base must be made. Parts of this thesis present an analysis of the classical slab model with focus on the implications for the hybrid extension. Subsequently, a range of excitation mechanisms that lead to strong vertical pumping velocities are characterized using idealized scenarios and the analysis of the parameter dependencies of the hybrid extension. Based on these, a local application of the model with respect to the North Atlantic is evaluated and put into context with the previously identified mechanisms and dependencies.

The question for the global wind energy input has been raised and studied many times using a number of modeling approaches (e.g. Alford, 2001; Watanabe and Hibiya, 2002; Alford, 2003; Furuichi et al., 2008; Rimac et al., 2013). However, these estimates remain a challenge since the results from the different studies show a large spread and have large errors. Both, a better understanding of the underlying processes and more robust global estimates of wind energy ultimately transferred to IGWs may lead to a more accurate picture. Statistical analysis of long time series may give insight to the change of the energy transfer in a changing climate. Moreover, they may open the possibility to evaluate effects associated to regional differences in atmospheric structures or recurring global patterns such as the El Niño Southern Oscillation.

This thesis is structured so that the reader may be guided from small to large spatial scales. First, the ocean response to an idealized, stationary storm is studied using a non-linear, axisymmetric model (Chapter 2). Then, the hybrid slab model is introduced and applied to the North Atlantic while highlighting the effects of a range of characteristic wind structures (Chapter 3). More analysis of the energy transfers involved is done by applying the hybrid slab model to a scenario comparable to the setup used for the axisymmetric simulation (Chapter 4). This analysis is then extended by comparing the near-inertial responses to a stationary and a moving storm. Differences with respect to the momentum transfer to the ocean are highlighted. An outlook towards a global prediction of energy transfers into the internal gravity wave field is highlighted with 10 years of data (Chapter 5). Some improvements based on the previous analyses are made, others are suggested for future application.

Chapter 2

An Axisymmetric Storm

The starting point of this thesis is the response of the ocean to an idealized, stationary storm. Storms have been reported to play a major role in the global distribution of the wind work (e.g. Price, 1983; Gill, 1984; Alford, 2001; Furuichi et al., 2008; Dippe et al., 2015). However, physical storms have a complex structure and show complex interactions with the ocean surface. In the present setup it is attempted to idealize the wind stress associated with a storm so that the processes leading to the generation of IGWs can be isolated. Therefore, an axisymmetric, non-linear Boussinesq model is set up (Section 2.1). The cylindrical symmetry gives the possibility to observe processes that are independent of the lateral movement of the wind structures. The geostrophic adjustment of the ocean, the flow structure and the spectral structure are analyzed (Section 2.2). Additionally, the energetics of the system are analytically predicted (Section 2.1) and analyzed in dependency on the given mixed layer depth (Section 2.2).

2.1 Model Description

2.1.1 Mathematical Formulation

A non-linear, axisymmetric and Boussinesq code is used to model the ocean response to an axisymmetric wind stress acting on the surface (Fig. 2.1). The code is adapted from that used by McMillan and Sutherland (2010) and Holdsworth and Sutherland (2013). In particular, the axisymmetric Navier-Stokes equations are numerically solved for the perturbation density ρ, azimuthal vorticity $\zeta = \partial u/\partial z - \partial w/\partial r$ and the azimuthal velocity v. The governing equations are

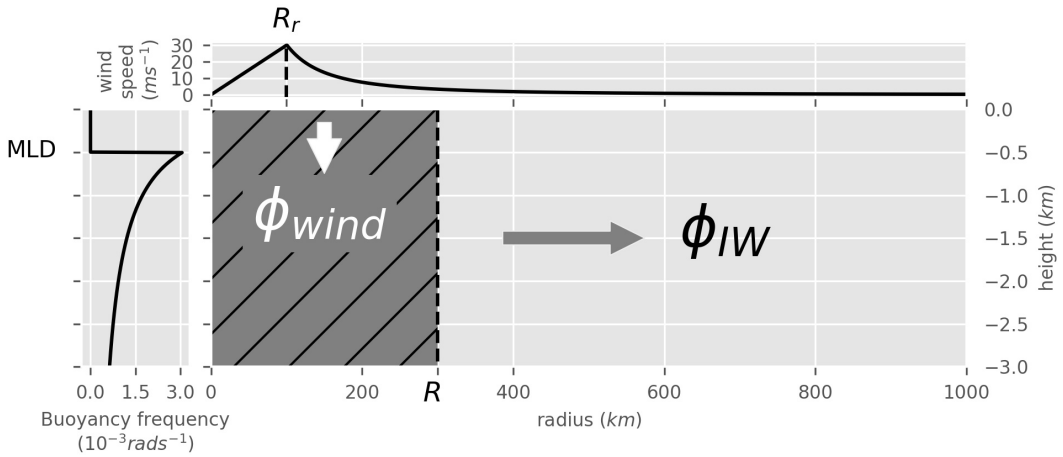

Figure 2.1: Schematic of the model setup from Voelker et al. (2016). A wind cyclone with a Rankine vortex structure prescribes the surface boundary conditions (upper panel). The stratification follows Gill (1984) (left panel). The wind work ϕ_{wind} and the radiated energy flux ϕ_{IW} are estimated.

$$\frac{\partial \zeta}{\partial t} = -ur\frac{\partial}{\partial r}\left(\frac{\zeta}{r}\right) - w\frac{\partial \zeta}{\partial z} + \frac{1}{r}\frac{\partial}{\partial z}\left(v^2 + fvr\right) + \frac{g}{\rho_0}\frac{\partial \rho}{\partial r} + D_1\left(\boldsymbol{\nu}, \zeta\right), \tag{2.1}$$

$$\frac{\partial v}{\partial t} = -u\frac{\partial v}{\partial r} - w\frac{\partial v}{\partial z} - \frac{1}{r}\left(uv + fur\right) + D_1\left(\boldsymbol{\nu}, v\right), \tag{2.2}$$

$$\frac{\partial \rho}{\partial t} = -u\frac{\partial \rho}{\partial r} - w\frac{\partial \rho}{\partial z} - w\frac{\partial \bar{\rho}}{\partial z} + D_0\left(\boldsymbol{\kappa}, \rho\right), \tag{2.3}$$

in which the variables u and w are the radial and vertical velocity respectively, f is the Coriolis frequency, and g is the gravitational constant. The background and reference densities are denoted by $\bar{\rho}(z)$ and ρ_0. $D_n(\boldsymbol{\alpha}, X)$ is the dissipation operator with dissipation constant $\boldsymbol{\alpha} = (\alpha_r, \alpha_z)$ acting upon a field X. Explicitly,

$$D_n(\boldsymbol{\alpha}, X) = \alpha_r\left(\frac{1}{r}\frac{\partial}{\partial r}\left(r\frac{\partial X}{\partial r}\right) - \frac{n^2 X}{r^2}\right) + \alpha_z\frac{\partial^2 X}{\partial z^2}, \tag{2.4}$$

where the order n, equal to 0 or 1 depending on the field X, refers to the order of the Bessel function of the first kind associated with the operator. The rate of diffusion of the azimuthal vorticity and velocity depend on the turbulent viscosity $\boldsymbol{\nu} = (\nu_r, \nu_z)$. The turbulent diffusivity $\boldsymbol{\kappa} = (\kappa_r, \kappa_z)$ determines the effective diffusion of heat and salt through changes to the density perturbation. Being turbulent flows, it is assumed $\boldsymbol{\nu} = \boldsymbol{\kappa}$.

A stream function $\psi(r, z)$ is defined implicitly such that

$$u = -\frac{\partial \psi}{\partial z} \qquad \text{and} \qquad w = \frac{1}{r}\frac{\partial}{\partial r} r\psi. \tag{2.5}$$

It is determined by inverting the vorticity diagnostic equation

$$\Delta_r \psi - \frac{\psi}{r^2} = -\zeta \tag{2.6}$$

with $\Delta_r = r^{-1}\partial/\partial_r(r\partial/\partial_r) + \partial^2/\partial_z^2$ being the scalar Laplacian operator in axisymmetric cylindrical coordinates.

By design, consideration of the azimuthal vorticity leads to a set of equations independent of the pressure p. Pressure itself is found from the diagnostic equation derived from the divergence of the radial and vertical velocity components of the momentum equations as well as the condition for incompressibility:

$$\begin{aligned}\frac{1}{\rho_0}\Delta_r p = &-\left(\frac{\partial u}{\partial r}\right)^2 - \left(\frac{\partial w}{\partial z}\right)^2 - 2\frac{\partial w}{\partial r}\frac{\partial u}{\partial z} - 2\frac{u^2}{r^2} + \frac{1}{r}\frac{\partial}{\partial r}(v^2 + rfv) \\ &- \frac{g}{\rho_0}\frac{\partial \rho}{\partial z} + \frac{1}{r}\frac{\partial}{\partial r}\left[rD_1\left(\boldsymbol{\nu}, u\right)\right] - \frac{\partial}{\partial z}D_0\left(\boldsymbol{\nu}, w\right)\end{aligned} \tag{2.7}$$

The governing equations are discretized and solved on a staggered grid with a second-order finite-difference scheme. The prognostic equations are advanced with a leap-frog time stepping scheme in which time splitting errors are minimized by performing an Euler backstep at regular intervals (McMillan and Sutherland, 2010).

Explicitly, Eqs. (2.6) and (2.7) are solved using a Fourier-sine-transform in the vertical and a Bessel-transform in the radial direction. The latter is defined by

$$F_n(k) = \int_0^\infty r J_n(kr) f(r) dr. \tag{2.8}$$

Here, J_n denotes the Bessel function of the first kind of order n. In the literature, this transform is also referred to as Hankel-transform of order n. Differentiation of the stream function ψ yields the vertical and radial velocity (Eq. 2.5) needed for advancing the field variables in time in Eqs. (2.1) to (2.3). A fourth-order exponential wave number cutoff filter suppresses ringing in the transforms, as described in the appendix.

2.1.2 Boundary Conditions and Background State

On the inner radial and bottom boundaries free-slip, no normal flow conditions are imposed. Explicitly, this is done by setting $\psi = 0$ on the corresponding boundaries. A 10 point flow relaxation scheme at the outer radial boundary inhibits the reflection of internal waves back into the domain (Jensen, 1998). The radial wind stress τ_r and azimuthal wind stress τ_θ are coupled to the ocean surface velocities by the relation

$$\tau_r = \nu_z \rho_0 \left(\frac{\partial u}{\partial z}\right)_{z=0} \qquad \tau_\theta = \nu_z \rho_0 \left(\frac{\partial v}{\partial z}\right)_{z=0} \tag{2.9}$$

The wind stress is computed from the wind at 10 m height with the bulk formulation

$$\boldsymbol{\tau} = \rho_{air} C_{10} \boldsymbol{U} |\boldsymbol{U}|, \tag{2.10}$$

$$\boldsymbol{U} = \begin{pmatrix} u_{10} \\ v_{10} \end{pmatrix} - \begin{pmatrix} u \\ v \end{pmatrix}_{z=0}, \tag{2.11}$$

in which the density of air is denoted by ρ_{air} and the constant drag coefficient by C_{10}. The stress then scales with the square of the velocity difference between the wind at 10 m height (u_{10}, v_{10}) and the surface velocity of the model ocean $(u, v)|_{z=0}$. The radial wind component is zero at all times. Combined with the discretized representation of Eq. (2.9), this yields a coupled system of equations for $(u, v)|_{z=0}$. It is solved analytically to obtain the wind stress and the surface velocity while maintaining a rigid lid condition at the surface: $w|_{z=0} = 0$. The surface boundary condition for the azimuthal vorticity is therefore given by $\zeta|_{z=0} = \tau_r (\nu_z \rho_0)^{-1}$.

An idealized storm is simulated by imposing a time-dependent radial profile of azimuthal wind above the surface. For simplicity, a Rankine vortex is chosen so that the wind has a constant vertical vorticity within a radius R_r and zero vorticity beyond. In particular, the wind magnitude increases linearly from zero at the origin to its maximum at R_r and decreases with an inverse radial dependency beyond. With this profile, the wind is acting over a well-defined area close to the radius R_r. The time evolution of the wind is set by linearly increasing its magnitude from zero to its maximum for quarter the storm duration, $\Delta T_s/4$, keeping it constant for $\Delta T_s/2$ and linearly decreasing its magnitude to zero for $\Delta T_s/4$. In most runs, the storm duration is set to

$\Delta T_s = 48$ hours. Note that at zero wind conditions, following the model storm, there is a slight drag slowing down the surface currents. However, because the surface currents remain slow the effect is negligible and the wind stress is approximately zero. For comparison, a wind pulse with double duration of ΔT_s, i.e. the increasing, constant-speed and decreasing phases, is tested. The influence of the vortex radius, R_r, is also examined by doubling its value.

The background density profile $\bar{\rho}(z)$ is defined so that the buoyancy frequency N corresponds to the form used by Gill (1984). In particular

$$N(z) = \begin{cases} 0, & \text{if } 0 > z > -H_m \\ \frac{S}{z_0 - z}, & \text{if } z \geq -H_m \end{cases} \tag{2.12}$$

with $S = N_0(z_0 - z_{ref})$. Here, H_m is the mixed layer depth, which is set to 50 m in most simulations. Thus the buoyancy frequency is equal to N_0 at the reference height $z_{ref} = -50$ m. The scaling height is set to $z_0 = 150$ m and the depth of the domain is $H = 3000$ m. Results are computed as they depend upon H_m as well as the maximum wind speed, v_{10}, the vortex radius, R_r, and the storm duration , ΔT_s. All model-related constants and reference parameters are summarized in Table 2.1.

2.1.3 A Geostrophic Adjustment Process

In order to characterize the adjustment to a geostrophically balanced flow, one can consider the linearized form of the governing equations for small perturbations from the initially stationary basic state:

$$\frac{\partial u'}{\partial t} - fv' = -\frac{1}{\rho_0}\frac{\partial p'}{\partial r} + D_1(\boldsymbol{\nu}, u') \tag{2.13}$$

$$\frac{\partial v'}{\partial t} + fu' = F + D_1(\boldsymbol{\nu}, v') \tag{2.14}$$

$$\frac{\partial w'}{\partial t} + \frac{g\rho'}{\rho_0} = -\frac{1}{\rho_0}\frac{\partial p'}{\partial z} + D_0(\boldsymbol{\nu}, w') \tag{2.15}$$

$$\frac{\partial \rho'}{\partial t} - w'\frac{\rho_0}{g}N^2 = D_0(\boldsymbol{\kappa}, \rho') \tag{2.16}$$

$$0 = \frac{\partial w}{\partial z} + \frac{1}{r}\frac{\partial (ru')}{\partial r}, \tag{2.17}$$

in which primes denote perturbed quantities and $F(r,t) = \partial/\partial z(\tau_\theta/\rho_0)$ denotes the surface wind stress forcing. After some algebra and assuming $N^2(z) \neq 0$ the coupled linear equations are combined into a single equation:

Table 2.1: Model setup related parameters. The radial wind profile has a Rankine vortex shape with radius R_r, where the wind is strongest. Wind speeds refer to the wind at 10 m height. The reference values for varying parameters are given in parenthesis.

parameter	value		comment
fixed parameters			
ρ_0	1027	kg m^{-3}	reference density of sea water
ρ_{air}	1.2	kg m^{-3}	density of air
f	10^{-4}	rad s^{-1}	Coriolis frequency
ν_r	1	m^2 s^{-1}	radial kinematic viscosity
ν_z	0.03	m^2 s^{-1}	vertical kinematic viscosity
Pr	1		Prandtl number
C_{10}	10^{-3}		drag coefficient
r_{max}	1000	km	maximum radius
n_r	1024		number of radial grid points
Δr	976.56	m	radial resolution
H	3000	m	depth of domain
n_z	128		number of vertical grid points
Δz	23.44	m	vertical resolution
t_{end}	40	days	duration of simulations
Δt	18	s	time step
n_t	20		# of time steps between Euler backsteps
varying parameters			
R_r	$50-100$ (50)	km	radius of Rankine vortex
$v_{10}(r=R_r)$	$30-60$ (30)	m s^{-1}	maximum wind velocity
H_{m}	$25-1000$ (50)	m	mixed layer depth
ΔT_{s}	$48-96$ (48)	hours	storm duration

$$\frac{\partial}{\partial t}\left[\frac{1}{r}\frac{\partial(rv')}{\partial r}-\frac{fg}{\rho_0}\frac{\partial}{\partial z}\left(\frac{\rho'}{N^2}\right)\right]=\frac{1}{r}\frac{\partial}{\partial r}\left[rF+rD_1(\boldsymbol{\nu},v')\right]-\frac{fg}{\rho_0}\frac{\partial}{\partial z}\left(\frac{D_0(\boldsymbol{\kappa},\rho')}{N^2}\right). \tag{2.18}$$

Note that the first term in the expression in square brackets, $r^{-1}\partial/\partial r(rv')$, is the vertical component of the vorticity; the second term represents the spin-up by vortex stretching. Thus in the absence of forcing and dissipation, Eq. (2.18) is a local potential vorticity conservation law. For simplicity, a dissipationless system is assumed for the theory that follows in this section. Thus, Eq. (2.18) becomes

$$\frac{\partial}{\partial t}\left[\frac{1}{r}\frac{\partial(rv')}{\partial r}-\frac{fg}{\rho_0}\frac{\partial}{\partial z}\left(\frac{\rho'}{N^2}\right)\right]=\frac{1}{r}\frac{\partial(rF)}{\partial r}. \tag{2.19}$$

This can be readily integrated in time from zero to infinity to determine the terminal stationary state after geostrophic adjustment. The final state is characterized by $u_\infty = w_\infty = 0$ and

$$v_\infty = \frac{1}{f\rho_0}\frac{\partial p_\infty}{\partial r}, \qquad \rho_\infty = -\frac{1}{g}\frac{\partial p_\infty}{\partial z}, \tag{2.20}$$

in which the subscript ∞ denotes the stationary state as time approaches infinity. Assuming a stationary initial state one integrates in depth and time to get

$$\frac{\partial}{\partial r}\left(\frac{\partial(r\,\langle v_\infty\rangle)}{r\partial r}\right) + \frac{f^2}{H}\left[\frac{1}{N^2}\frac{\partial v_\infty}{\partial z}\right]_{-H}^{0} = \frac{1}{H}\frac{\partial}{\partial r}\left[\frac{1}{r}\frac{\partial}{\partial r}\left(r\int_{-H}^{0}\int_{0}^{\infty} F dt dz\right)\right]. \tag{2.21}$$

Here, $\langle v_\infty\rangle$ denotes the depth-averaged terminal azimuthal velocity and H is the depth of the domain. Due to a forcing in which there is negligible stress on the surface after a finite time and a free-slip condition at the bottom of the domain, one can assume zero friction at those boundaries, as $t \to \infty$. Consequently, the second term on the left-hand side vanishes. The resulting equation is integrated in r and z to obtain

$$\langle v_\infty\rangle = \frac{1}{H}\int_{-H}^{0}\int_{0}^{\infty} F dt dz + c(r) = \frac{1}{H}\int_{-H}^{0}\int_{0}^{\infty} F dt dz \tag{2.22}$$

The condition on the integration constant with respect to z, $c(r)$, is set so that $\partial/\partial r[r^{-1}\partial/\partial r(rc)]$ vanishes. This is true for any linear combination of functions proportional to r^{-1} and r. Requiring a bounded solution for zero and infinite radius leads to the conclusion that $c(r) \equiv 0$.
Given a wind stress pulse resulting from the sudden manifestation of a Rankine vortex in the atmosphere and assuming the wind is much faster than the ocean surface velocity one has

$$\langle v_\infty\rangle = \frac{1}{H}\int_{-H}^{0}\int_{0}^{\infty} F dt dz = \frac{\rho_{air} C_{10} v_{10}^2 \Delta T_s}{6\rho_0 H}\begin{cases}\frac{r^2}{R_r^2}, 0 < r \le R_r\\ \frac{R_r^2}{r^2}, r > R_r\end{cases} \tag{2.23}$$

The above relation predicts the depth-averaged terminal azimuthal velocity with linear theory and zero internal stresses. The latter assumption in combination with a rigid lid approximation generally leads to a surface confined flow with unphysically large amplitude. To interpret the above result, it helps to consider that the internal stresses diffuse the flow through the water column and thereby change the kinetic and available potential energy density as well as

the vorticity distribution (Eq. 2.18). The corresponding diffusion time scales with vertical scale L_z and horizontal scale L_h are $T_h = L_h^2/\nu_h$ for horizontal diffusion and $T_z = L_z^2/\nu_z$ for vertical diffusion.

For a rough estimate, the viscosities from Table 2.1, the vertical scaling height $L_z = z_0 = 150\,\mathrm{m}$ and the radius of the Rankine vortex $L_h = R_r = 50\,\mathrm{km}$ are used. The vertical length scale is chosen to be the scaling depth of the stratification (Eq. 2.12) as it sets the vertical scale of variation of the azimuthal velocity in the vortex. One then arrives at the characteristic damping time scales of $T_h = 79.27\,\mathrm{years}$ and $T_z = 8.68\,\mathrm{days}$. Since the horizontal time scale is several orders of magnitude larger than the vertical time scale, it is concluded that vertical diffusion is dominant in this setup.

Note that even though the energy densities and vorticity of the flow are affected by the diffusion, the volume transport remains unchanged. Consequently, the predicted value of the depth-averaged terminal azimuthal velocity (Eq. 2.23) can be regarded as the depth-independent terminal velocity of a system with dominant vertical diffusion.

This analysis reveals some fundamental properties of the flow. Most importantly, with a rigid lid approximation in place, the horizontal Reynolds stress $\boldsymbol{\tau}$ is the only mechanism that initially transports momentum into the ocean interior. Only when a gradient of velocity or density is established underneath the surface can advection and buoyancy act. That also implies that the forcing on the stratified region is predominantly horizontal rather than vertical through turbulence in the mixed surface layer.

In the present simulation the time scale for the vertical diffusion scheme has been chosen so that vortex formation and internal gravity wave radiation can be observed in reasonable model time while keeping the dissipation of the radiated waves negligibly small. The resulting depth evolution of the azimuthal velocity and thus the geostrophic adjustment follows two mechanisms with distinct time scales. As argued above, the flow is initially controlled by the diffusive coupling to the interior. Subsequently, the vertical evolution follows the vertical advection time scales in the mixed and stratified region. After the flow reaches an approximate geostrophic balance in the horizontal, it diffuses vertically with the vertical diffusion time scale.

2.1.4 Energetics of the System

The energetics of the system are described in terms of the wind work Φ_{wind}, the energy radiated laterally by internal waves Φ_{IW}, the energy transferred to the vortex underlying the model storm E_{v}, and the dissipated energy D. Assuming an energetically isolated system, the energy balance is set up so that

$$\Phi_{\text{wind}} = E_{\text{v}} - \Phi_{\text{IW}} - D. \tag{2.24}$$

The wind work, mechanical energy of the central vortex, as well as radiated energy fluxes due to waves are calculated from the model results. The dissipation can then be deduced from the other components of the energy balance (Eq. 2.24) without explicit knowledge about the transient states. For comparison, the three terms are predicted from the previously derived theory and scaling analysis.

A general formula for the integrated wind power, i.e. the wind work, is

$$\Phi_{\text{wind}} = \int_0^T \int_0^{R_c} \int_0^{2\pi} \boldsymbol{\tau} \cdot \boldsymbol{u} \; r d\theta dr dt, \tag{2.25}$$

in which $\boldsymbol{\tau} \cdot \boldsymbol{u}$ is the product of the wind stress and the ocean surface velocity. The integrals are evaluated over a disk of radius R_c and a model time T. Given a forcing time $\Delta T_{\text{s}} = 2\,\text{days}$ and the characteristic scales of wind stress $\tau \sim 1\,\text{N/m}^2$, azimuthal velocity $v \sim 0.1\,\text{m/s}$ and radial length scale $R_r \sim 50\,\text{km}$, the magnitude of the wind power can be estimated. It yields a value of the order $\Phi_{wind} \sim 100\,\text{TJ}$. Considering that this energy is imparted over a circle with a radius $R_r = 50\,\text{km}$ and a time span of 2 days, it is equivalent to the normalized wind work of the order $10^{-2}\,\text{MJ m}^{-2}$ and the average wind power of the order or $10^{-2}\,\text{W m}^{-2}$. This agrees well with observations of hurricanes (Sanford et al., 2011) but is one order of magnitude larger than modeled climatological energy fluxes in mid-latitude regions (Alford, 2001; Furuichi et al., 2008).
The energy associated with internal waves leaving a cylinder with radius R_c after a time T can be estimated using the radial energy flux $u\,p$:

$$\Phi_{\text{IW}} = \int_0^T \int_{-H}^0 \int_0^{2\pi} up \; R_c \; d\theta dz dt \tag{2.26}$$

The radial energy flux $u\,p$ is approximated by the energy density times the radial group velocity for monochromatic waves. As a first order estimate of the energy transport, a dominant oscillatory vertical motion at the radius,

R_r, beneath the wind maximum, is considered. From linear theory for internal modes in uniform stratification characterized by constant buoyancy frequency $N = N_{\max} = 0.01\,\mathrm{rad/s}$, one may predict the resulting energy transport (e.g. Sutherland, 2010). In particular, for waves of frequency σ and vertical mode number m, the energy flux ϕ_{IW} is

$$\phi_{\mathrm{IW}} = \rho_0 |A_w|^2 \frac{1}{\sigma k_3} \frac{(N^2 - \sigma^2)^{\frac{3}{2}}}{(\sigma^2 - f^2)^{\frac{1}{2}}}, \tag{2.27}$$

in which A_w denotes the amplitude of the vertical velocity. Even though linear theory assumes a constant amplitude A_w, one can consider a transiently excited quasi-monochromatic wave packet whose amplitude at a fixed radius changes in time as a Gaussian such that $A_w = A_{w0} \exp(-(t - t_0)^2/(2s_t^2))$, where s_t characterizes the duration of the packet at $r = R_r$. Integrating (Eq. 2.27) over times $T \ll s_t$ and over the cylinder with the radius R_r yields an expression for the total radiated energy:

$$\Phi_{\mathrm{IW}} = \frac{2\pi^{\frac{3}{2}} R_r \rho_0 |A_{w0}|^2 s_t (H - H_{\mathrm{m}})}{\sigma k_3} \frac{(N^2 - \sigma^2)^{\frac{3}{2}}}{(\sigma^2 - f^2)^{\frac{1}{2}}} \tag{2.28}$$

By energy conservation for a radially propagating small-amplitude wave packet, its amplitude A_w decreases as one over the square root of the radius, r. Hence, the expression $r|A_w|^2$ is approximately constant. Thus the energy flux evaluated at $r = R_r$ in Eq. (2.28) is representative of the flux at arbitrary radii $R_c > R_r$.

Taking $H_{\mathrm{m}} = 50\,\mathrm{m}$, $A_{w0} = 10^{-4}\,\mathrm{m/s}$, $k_3 = \pi/H$ (for a mode-1 wave) and setting σ and s_t to the forcing time scales, that is $s_t = 2\,\mathrm{days}$ and $\sigma = 2\pi/12\,\mathrm{hours}$, one obtains an estimate of the order $\Phi_{IW} \sim 176\,\mathrm{GJ}$. The amplitude of the vertical velocity A_{w0} used here represents typical values from the control run of the model. Relative to the wind work, the energy radiated corresponds to a transfer of $0.17\,\%$. However, the assumption of a uniform stratification with a constant buoyancy frequency equal to the value of maximum buoyancy frequency in the simulation leads most likely to an overestimate of the energy. Note that Eq. (2.28) has a singularity at $\sigma = f = 10^{-4}\,\mathrm{rad\,s^{-1}}$ and is therefore sensitively dependent on the forcing frequency. Typical frequencies of low mode waves observed in the simulations are very close to f only for horizontal wavelengths larger than 130 km (Fig. 2.6). The predicted order of magnitude corresponds to values of σ ranging from about $1.034\,f$ to $1.8\,f$. Larger frequencies are associated to smaller radial energy fluxes.

This estimate assumes that the primary mechanism transferring energy to internal gravity waves is the excitation of vertical mode-1 waves through forced vertical motion in the stratified water column. In the previous section it was concluded that the dominant forcing on the stratified region is the vertical momentum transfer through horizontal stresses. Buoyancy production through heat exchange between the ocean surface and the atmosphere as well as turbulent motion in the mixed region are strong drivers for vertical velocities (Bars et al., 2015; Lecoanet et al., 2015). Consequently, the sole consideration of wind induced surface stress may lead to small vertical velocities and little energy transfer to internal gravity waves.

The energy transferred to the vortex beneath the wind forcing is obtained by integrating the mechanical energy density within a cylinder of radius R_c enclosing the vortex.

$$E_{\mathrm{v}} = \left[\int_{-H}^{0} \int_{0}^{R_c} \int_{0}^{2\pi} (\mathcal{E}_{\mathrm{KE}} + \mathcal{E}_{\mathrm{APE}})\, r d\theta dr dz \right]_{t=T} \tag{2.29}$$

This is done at a late time T so that excited internal gravity waves are radiated away and the result isolates the energy of the vortex. Note that the mechanical energy density is expanded in kinetic and available potential energy density. The former is given by

$$\mathcal{E}_{\mathrm{KE}} = \frac{\rho}{2}(u^2 + v^2 + w^2). \tag{2.30}$$

The latter is estimated using the relation (Kang and Fringer, 2010)

$$\mathcal{E}_{\mathrm{APE}} = \frac{g^2\rho^2}{2\rho_0 N^2} + \frac{g^3\rho^3}{6\rho_0^2 N^6}\frac{\partial}{\partial z}\left(N^2\right). \tag{2.31}$$

A prediction for the energy stored in the geostrophic vortex at late times can be obtained by using the late-time azimuthal velocity $\langle v_\infty \rangle$ (Eq. 2.23), spatially integrated so that

$$E_v = \int_{-H}^{0} \int_{0}^{2\pi} \int_{0}^{\infty} \frac{\rho_0}{2} \langle v_\infty \rangle^2 \, r dr d\theta dz = \frac{\pi}{6\rho_0 H} \left(\frac{2}{3} \rho_{air} C_{10} v_{10}^2 \Delta T_{\mathrm{s}} R_r \right)^2. \tag{2.32}$$

Evaluating Eq. (2.32) leads to an estimate of approximately $E_{\mathrm{v}} \sim 1\,\mathrm{TJ}$.

In summary, an energy transfer from the wind input to internal gravity waves and a geostrophically balanced vortex of the order 0.01% and 1% relative to

the wind work is predicted, respectively. Neglecting vertical turbulent motion and consequent mixing and considering energy transfer due to stress only leads to a predicted dissipation of more than 90% of the wind work.

2.2 Results and Discussion

2.2.1 Description of the The Control Run

All simulations performed show qualitatively the same wave and vortex generation mechanisms. These are discussed here with regard to a control run in which the mixed layer depth is $H_{\mathrm{m}} = 50\,\mathrm{m}$ and the critical radius of the Rankine vortex radial wind profile is $R_r = 50\,\mathrm{km}$. The associated maximal wind speed at 10 m height is $v_{10} = 30\,\mathrm{m\,s^{-1}}$. The time evolution of the wind is set by linearly increasing its magnitude from zero to its maximum for quarter the storm duration $\Delta T_{\mathrm{s}}/4$, keeping it constant for $\Delta T_{\mathrm{s}}/2$ and linearly decreasing its magnitude to zero over another $\Delta T_{\mathrm{s}}/4$. In the control run, the storm duration is set to $\Delta T_{\mathrm{s}} = 48\,\mathrm{hours}$.

During the first phase of the forcing the azimuthal surface velocity is accelerated due to the surface stress of the growing model storm. Consequently, the centripetal and the Coriolis force accelerate the fluid radially outward. Upwelling and downwelling are induced respectively at radii smaller and larger than the radius, R_r, of the Rankine vortex (Fig. 2.2a). This motion forms immediately after the stress starts acting on the surface and leads to velocities with amplitudes up to 3 m/s within 12 hours. Correspondingly, a bottom intensified positive pressure anomaly develops at radii smaller than R_r. At larger radii a bottom-intensified negative pressure anomaly is formed. During the decrease of the wind stress forcing in the Coriolis effect starts to counteract the described motion (Fig. 2.2b). The inertial oscillations reverse the flow and cause inertial pumping with largest amplitudes close to R_r. The vertical motion is forced throughout the whole water column including the stratified region below the mixed layer depth. This inertial pumping corresponds to the generation mechanism for internal gravity waves suggested in the previous section. Induced dominant mode-1 internal gravity waves are observed (Fig. 2.2c). A second generation mechanism arises from the bottom pressure anomaly close to R_r. Being forced by the return flow of the surface inertial oscillation it oscillates with the Coriolis frequency and generates upward propagating internal gravity waves with higher vertical modes (Fig. 2.2d).

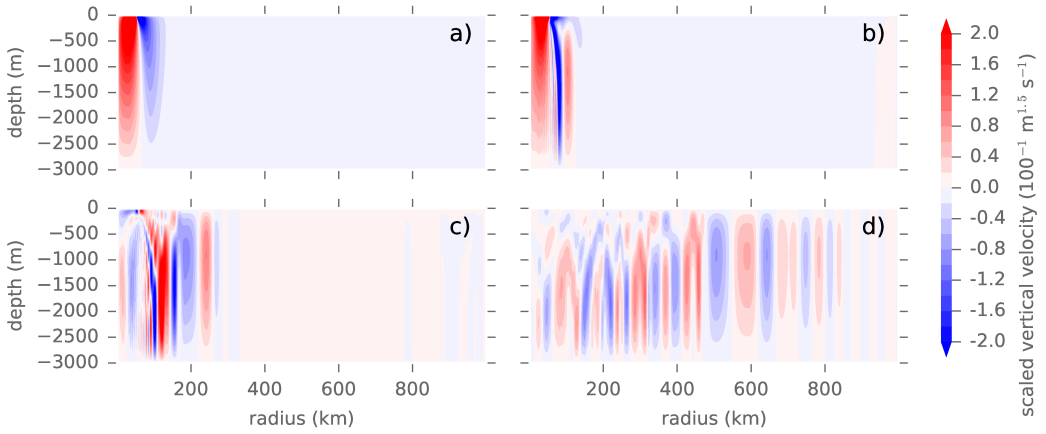

Figure 2.2: Snapshots of vertical velocity for the control run at model time a) 12h b) 22.5h c) 50h and d) 150h. For scaling reasons the vertical velocity was multiplied by the square root of the radius. This corresponds to the asymptotic behavior of the Bessel function of first kind and order 0 for large radii. The figure is adapted from Voelker et al. (2016).

2.2.2 Effects of the Surface Forcing Parameters

The inertial period corresponding to the inertial frequency $f = 10^{-4}\,\mathrm{rad\,s^{-1}}$ is approximately 0.73 days. In comparison, the duration of the pulse is $\Delta T_s = 2$ days. However, the ramp-up and ramp-down phases, each of which is 0.5 days, correspond to linear changes in the wind and thus, changes in the square of the wind stress amplitude. The effective forcing time is approximately twice the inertial period. Thus, the near inertial oscillations are most strongly excited. For comparison, an experiment with double the duration of the forcing in all phases is conducted. The longer pulse acts over a time of approximately 3.5 inertial periods. Therefore, the wind stress is effectively out of phase with the inertial oscillation at the end of the pulse. It is observed that the wind forcing counteracts the inertial oscillation of the formed vortex, which is reduced correspondingly and the radiation of columnar internal gravity waves is less pronounced. Hence, the time scales of the wind pulse appear to be important to the wave generation mechanism.

Comparing the control run with a simulation with double the wind speed, $v_{10} = 60\,\mathrm{m\,s^{-1}}$, or double the radius of the vortex, $R_r = 100\,\mathrm{km}$, one can observe that the described flow structure and generation mechanisms of internal gravity waves are qualitatively independent of the wind speed and the vortex radius.

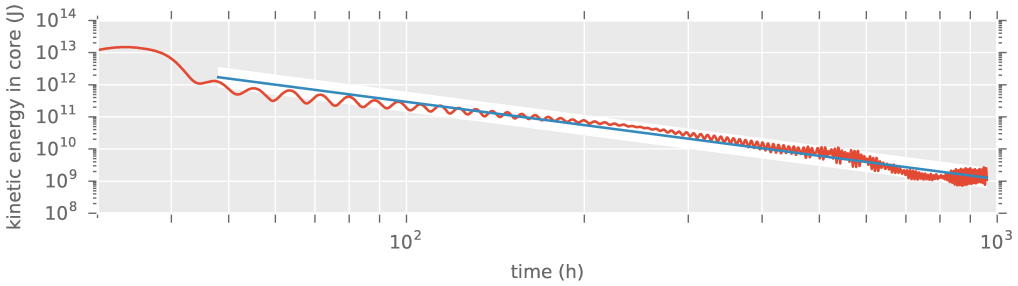

Figure 2.3: Decay of the kinetic energy within the cylinder of radius $R_c \approx 250\,\mathrm{km}$ in the control run with log-log scaling. The start of the decay, that is the time the wind stress becomes zero, is set to $t = 48\,\mathrm{h}$. It is indicated by the black line. The blue line shows a linear fit revealing a power law $E_\mathrm{v} = At^B$ with $B = -2.41 \pm 0.02$. The white shading corresponds to the 95% confidence interval.

Table 2.2: Table of scaling exponents from the fit function $E = At^B$ of the kinetic energy in the vortex in dependency of the mixed layer depth, H_m. The errors are the 95 % from log-log fit to the time evolution of the kinetic energy of the vortex.

H_m	B
25	-2.40 ± 0.02
50	-2.41 ± 0.02
100	-2.42 ± 0.02
200	-2.39 ± 0.02
500	-2.19 ± 0.02
1000	-1.30 ± 0.02
3000	-0.64 ± 0.03

2.2.3 Geostrophic Adjustment of the Vortex

Geostrophic adjustment occurs during three different phases. The first phase is the development of the disturbance in the water column during the ramp up of the wind stress on the surface. During this phase the surface and consequently the subsurface layers are accelerated and the above described inertial oscillation develops. The second phase is characterized by inertial pumping, the advection of the azimuthal velocity through the mixed layer and the generation and radiation of internal gravity waves. This phase starts right after the ramp-up of the forcing and quickly ends after ramping down as the inertial oscillation damps out. It can therefore be best described as acting on a time scale comparable to the duration of the forcing. Overlapping the second adjustment

phase, the decay of the mechanical energy of the vortex towards the geostrophic balance starts right after the end of the forcing (at time $t = 48$ hours). This adjustment is dominated by the vertical diffusion through the stratified region and therefore acts with the associated diffusion time scale. In the control run, the kinetic energy within the radius $R_c = 250$ km decays following a power law $E = At^B$ with $B = -2.41 \pm 0.02$ (Fig. 2.3). The time for decay of the kinetic energy after the wind stress stops (at time $t = 48$ hours) to half its value is approximately 16 hours. However, during the 40 day period of the simulation generally the equilibrium with a vertically homogeneous azimuthal velocity is not reached.

The scaling exponent B is constant for mixed mixed layer depths shallower than $H_\mathrm{m} \leq 200$ m. Deeper mixed layers and correspondingly lower stratification leads to a deeper extent of the vortex at the end of the second adjustment phase. In the runs with deeper mixed layers, $H_\mathrm{m} > 200$ m, the decay of the kinetic energy of the vortex is slower (Table 2.2). For comparison, a run with no stratification throughout the model ocean depth ($N \equiv 0\,\mathrm{rad\,s^{-1}}$) was performed. In that case, the development of a vertically constant component of the vertical velocity on a time scale shorter than the forcing duration is observed. Moreover, in the absence of stratification there is no radiative phase. The energy stored in the inertial oscillation can not be transferred to internal gravity waves. Instead, the oscillation damps out with the diffusion time scales only. The corresponding scaling exponent is then $B = -0.64 \pm 0.03$.

An increased radius of the vortex, $R_r = 100$ km, leads to the same scaling exponent, $B = -2.43 \pm 0.04$, as in the control run. In contrast, a larger maximum wind speed, $v_{10} = 60\,\mathrm{m\,s^{-1}}$, is associated with a faster decay ($B = 2.71 \pm 0.02$) and a wind stress pulse with double duration, i.e. $\Delta T_\mathrm{s} = 4$ days, leads to a slower change of the kinetic energy of the vortex ($B = 1.94 \pm 0.03$).

In summary, there are three overlapping stages of adjustment in the simulations, each with a distinct time scale. The first is the spin-up of the vortex and the inertial oscillation with the forcing time scale. In the second stage, the inertial oscillation decays until it reaches a horizontal geostrophic balance. This process is associated to the radiation of internal gravity waves. At last, the vortex diffuses in the vertical until a vertically constant vortex is established. The diffusion time scale is typically longer than the end of the model time.

2.2.4 Internal Gravity Waves

Generation and Propagation of Waves

Whereas at radii close to the Rankine vortex radius, R_r, the inertial oscillation dominates the flow, it is characterized by radially outward propagating internal gravity wave packets with distinct radial group velocities in the far field (Fig. 2.4). These are generated by two different mechanisms. The first and more dominant is the generation by inertial pumping. The inertial oscillation associated with the spin-up of the vortex beneath the wind forcing induce a return flow in the interior and a corresponding up- and downwelling with largest amplitudes close to the radius of the vortex, R_r. This vertical oscillation stretches throughout all the water column and induces near-inertial vertical mode-1 internal gravity waves. The second generation mechanism is related to a bottom intensified pressure anomaly associated to the spin-up of the vortex. It oscillates with the return flow of the inertial oscillation and locally generates upward propagating internal gravity waves with higher vertical mode structure. Both generation mechanisms are associated to the second adjustment phase described above. The wave packets show distinct group velocities in the far field where higher vertical mode wave packets have lower radial group velocity. Higher vertical modes are generated not only at the critical radius but are also excited by non-linear processes in the lower mode wave packet (Fig. 2.4).

Since the duration of the pulse, ΔT_s, determines the excitation of the near-inertial oscillation it has dramatic effects on the generation of internal gravity waves. In the simulation with double the duration of the pulse with respect to the control run, in which $\Delta T_s = 2\,\text{days}$, the excitation of internal waves was significantly reduced.

An increased radius of the Rankine vortex, $R_r = 100\,\text{km}$, leads to an increase in radial lengths scales. It is observed that this is related to an increased radiation of waves with higher vertical mode. However, a change in the radial group velocities of the excited internal gravity waves is not observed. Thus, the radial wave numbers of the waves must be determined by the vertical structure and the forcing time scales.

In simulations with deeper mixed layers, and consequently with reduced stratification, waves propagating with reduced radial group velocities are observed

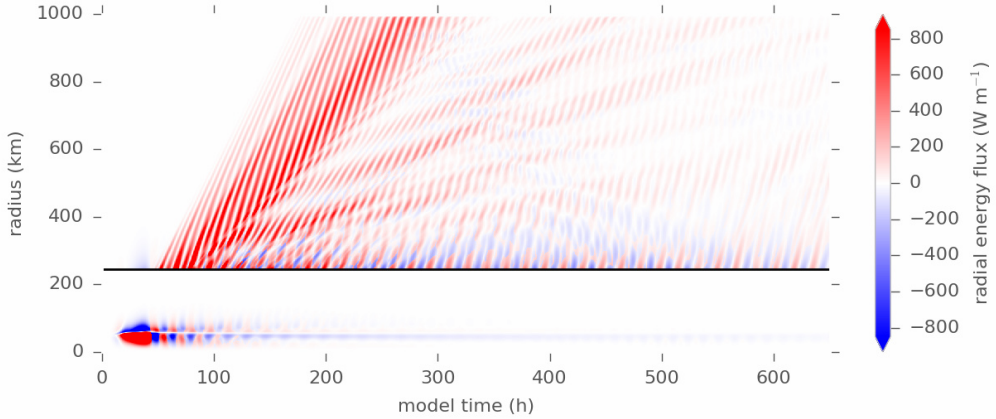

Figure 2.4: Radial time series plot of the azimuthally integrated radial energy flux $\int_0^{2\pi} \phi_{\mathrm{IW}}\, r d\theta$ as a function of time and radius for control run with the reference parameters listed in Table 2.1. The maximal value in depth is shown. Near and far field have separate color scales. The color bar corresponds to the far field (upper panel). The characteristic beams are wave packets with distinct vertical modes and group velocities.

(Fig. 2.5). Consequently the wave packets with different vertical mode structure separate at smaller radii and pass through the radius R_c as separate wave packets. Moreover, continually generated higher mode wave packets superimpose when the radial extent of the packets is larger than the radial distance between two successively generated wave packets.

Spectra

The spectral structure of the induced internal gravity waves is analyzed in terms of the radial wave-number-frequency spectrum for the vertical velocity at the mixed layer depth, $z = -H_{\mathrm{m}}$, (Fig. 2.6a). Note that the cylindrical symmetry of the radiating waves requires a Fourier-Bessel-transform (Eq. 2.8) in the radial direction. The spectrum is characterized by distinct lines with largest amplitudes close to the inertial frequency. The structure of these lines resembles the dispersion relation associated with vertical normal modes in the stratification prescribed by Eq. (2.12) (Fig. 2.6b). The difference between the predicted spectrum and the numerically obtained dispersion relation may be related to the transient nature of the excitation of internal gravity waves. The vertical structure of the waves does not entirely coincide with the decomposition into the vertical modes. For example, a mode-1 wave with a wave number $k_{\mathrm{r}} = 0.8 \cdot 10^{-3}\,\mathrm{m}^{-1}$ has a predicted frequency of $10.4 \cdot 10^{-4}\,\mathrm{rad\,s}^{-1}$ but was

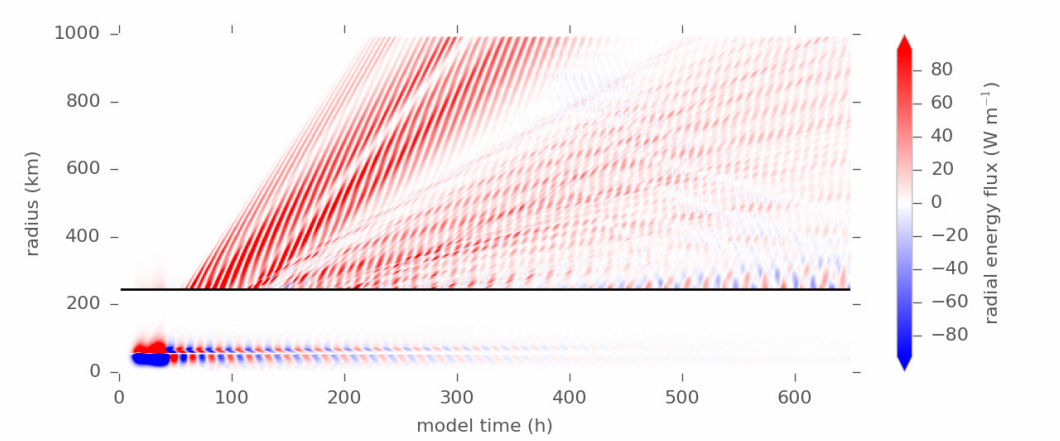

Figure 2.5: Same as Fig. 2.4 but with $H_m = 500\,\mathrm{m}$. The radiated wave packets are characterized by weaker stratification and thus smaller group velocities. The associated energy fluxes are an order of magnitude smaller. Consequently the wave packets separate over shorter time scales. Due to the decreased radial group velocity a superposition of higher mode internal gravity waves occurs.

measured with $\sigma \approx 12 \cdot 10^{-4}\,\mathrm{rad\,s^{-1}}$. High probability densities at low wave numbers and frequencies equal to f correspond to the inertial oscillation of the vortex.

2.2.5 Energetics

Energetics of the Control Run

The energetics of the model reflect the above-described adjustment process. The wind work is equal to the integral of the product of the wind shear stress exerted on the surface with the surface velocity itself. In the control simulation, it is approximately $\Phi_{\mathrm{wind}} \approx 401\,\mathrm{TJ}$ (Table 2.4). This corresponds to the predicted order of magnitude (Eq. 2.25). The mechanical energy stored in the vortex below the forcing region by the end of control run is approximately $E_{\mathrm{v}} \approx 47\,\mathrm{TJ}$. As discussed in Section 2.2.3, this energy depends on the vertical extent of the vortex at the time it is observed. Its magnitude by the end of the simulation time represents the state of adjustment rather than the terminal value. The measured mechanical energy is an order of magnitude higher than predicted (Eq. 2.32) but also subject to further dissipation. The total energy radiated as internal gravity waves in the control run is approximately $\Phi_{\mathrm{IW}} \approx 61\,\mathrm{GJ}$. That result corresponds to the predicted order of magnitude (Eq. 2.28) and is controlled mainly by the buoyancy frequency and the magnitude of

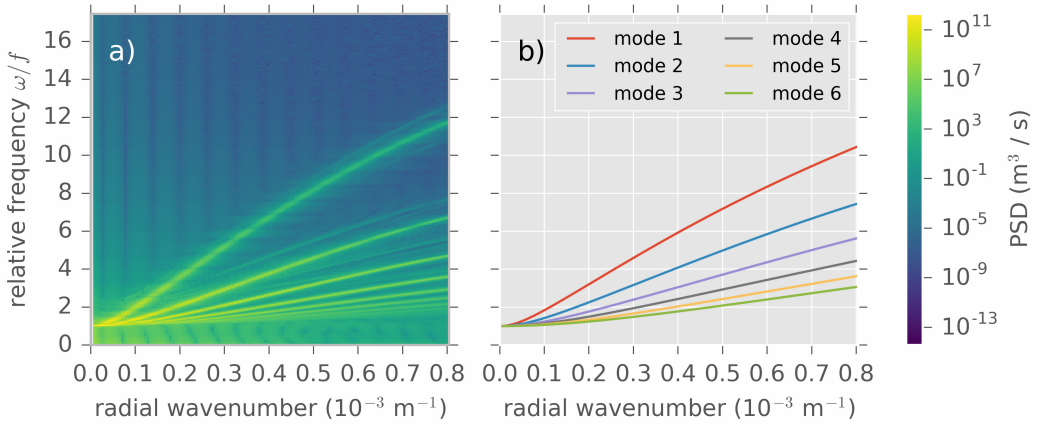

Figure 2.6: (a) Wave-number-frequency spectrum of the vertical velocity from the control run at the mixed layer depth. In accordance with the symmetry, a Fourier-Bessel-transform was used in radial direction (Eq. 2.8). The vertical velocity was multiplied with a 2-dimensional Hanning window to avoid ringing in the spectrum. (b) Numerically obtained dispersion relation for the first six vertical normal modes. The x-axes were limited to a maximum of 4 times the Nyquist wave number to account for attenuation due to resolution.

the vertical velocity. Based on these results and the energy balance (Eq. 2.24), the residual dissipation is about $D \approx 354\,\mathrm{TJ}$, or equivalently $D/\Phi_{\mathrm{wind}} \approx 88\,\%$ of the wind energy input.

The Wind Amplitude, Radial Length Scale and Forcing Time Scale

Here it is reminded that the surface velocity scales with the wind stress, which scales with the square of the wind velocity (Eqs. 2.10 and 2.10). Hence, the wind power which is the product of the wind stress and the surface velocity, scales with the fourth power of the wind velocity. Doubling the wind speed therefore leads to a wind work of 5657 TJ, an increase by a factor of approximately 14. The excited inertial oscillation has a larger amplitude and therefore takes a longer time to damp out. The radiated energy fluxes are increased by a factor larger than 20 (Table 2.3).

Increasing the critical radius of the Rankine vortex by a factor 2, so that $R_r = 100\,\mathrm{km}$, leads to a larger area on which the wind stress acts. Correspondingly, the wind work is increased to 1416 TJ (Table 2.3). The proportion of energy radiated as internal gravity waves relative to the wind work is only

Table 2.3: Energetics of model runs with the same mixed layer depth H_m but varied maximal wind speed v_{10}, radius of the Rankine vortex wind profile R_r or duration of the pulse, ΔT_s. The dissipation D is the residual of all other terms (Eq. 2.24). The first line is the control run with reference parameters $H_m = 50\,\mathrm{m}$, $R_r = 50\,\mathrm{km}$, $v_{10} = 30\,\mathrm{m\,s^{-1}}$ and $\Delta T_s = 2\,\mathrm{days}$.

$\boldsymbol{H}_m$ (m)	$\boldsymbol{\Phi}_{wind}$ (TJ)	$\mathbf{E}_v/\boldsymbol{\Phi}_{wind}$ (%)	$\boldsymbol{\Phi}_{IW}/\boldsymbol{\Phi}_{wind}$ (%)	$\mathbf{D}/\boldsymbol{\Phi}_{wind}$ (%)	**varied parameter**
50	401	12	-0.015	-88	control run
50	5657	10	-0.024	-90	$v_{10} = 60\,\mathrm{m\,s^{-1}}$
50	1416	9	-0.02	-91	$R_r = 100\,\mathrm{km}$
50	911	20	-0.004	-80	$\Delta T_s = 4\,\mathrm{days}$

slightly increased (from 0.015 % to 0.019 %). This increase is related to an increased radiation of waves with higher vertical mode.

The wind pulse supplying energy to the surface in the control run consists of three phases. First, the wind is linearly ramped up within quarter its total duration, $\Delta T_s/4$, then it is constant at its maximum for $\Delta T_s/2$ and finally it is ramped down linearly in the last quarter of the duration $\Delta T_s/4$. In the control run the duration of the pulse is $\Delta T_s = 2\,\mathrm{days}$. Forcing with a twice as long wind pulse ($\Delta T_s = 4\,\mathrm{days}$) leads to a wind work of 911 TJ. Compared to the control run with $\Phi_{wind} = 401\,\mathrm{TJ}$, this increase corresponds to the longer forcing time. However, the out-of phase excitation of the inertial oscillation as described above halves the energy radiated as internal gravity waves compared to the control run. Instead a significantly larger portion is imparted into the vortex. The increase from 12 % in the control run to 20 % is not associated to the stage of the geostrophic adjustment, i.e. to the vertical diffusion of the vortex, but to a correspondingly raised azimuthal velocity.

The Role of the Mixed Layer Depth

It is observed that with increasing mixed layer depth (and consequently decreasing maximum stratification), the energy inferred into the system decreases from 410 TJ at $H_m = 25\,\mathrm{m}$ to 348 TJ in the run with $H_m = 1000\,\mathrm{m}$. At the same time, higher azimuthal vorticities (Eq. 2.1) are observed. It is interpreted that a reduced stratification allows for a faster spin-up of the center vortex and the associated vertical velocity due to reduced restoring forces in the vertical. However, the increased positive radial velocity acts as a negative feedback on the azimuthal velocity via the Coriolis effect. Consequently, the

azimuthal velocities are generally smaller and less energy is transferred (Eq. 2.25).

The mechanical energy stored in the vortex at the end of the model run is observed to decrease from 53 TJ (at $H_{\mathrm{m}} = 25\,\mathrm{m}$) to 14 TJ (at $H_{\mathrm{m}} = 1000\,\mathrm{m}$). However, this value depends on the state of the geostrophic adjustment as described above. A deeper mixed layer and a correspondingly reduced stratification below the mixed layer base is associated with increased azimuthal vorticities or equivalently larger radial and vertical velocities. Hence, the vertical advection of the azimuthal velocity is stronger for deeper mixed layers and the vortex expands in depth on shorter time scales. Consequently, the vertical extent of the center vortex at the end of the model run depends on the mixed layer depth of the run. This effect masks the quantification of the energy transferred to the vortex in its equilibrium state.

A reduced stratification has a positive feedback on the vertical velocities and thus on the inertial pumping amplitude as described above. However, one finds that the total energy radiated reduces from 65 GJ at $H_{\mathrm{m}} = 25\,\mathrm{m}$ to 13 GJ at $H_{\mathrm{m}} = 1000\,\mathrm{m}$. This decrease is associated with the decreased maximum stratification as the mixed layer depth increases.

Dissipation is implemented using a harmonic mixing operator (Eq. 2.4). Therefore, it depends solely on the internal shear stresses. These are largest close to the surface where the wind stress imparts a strong shear. Therefore, most of the dissipation is associated with shallow depth and qualitatively independent of the mixed layer depth. The absolute value of the dissipated energy ranges between 327 TJ and 357 TJ and decreases with the mixed layer depth.

In order to quantify the scaling of the different components of the energy balance with the stratification at the mixed layer depth, a run with zero stratification was compared to all other scenarios. The corresponding values for Φ_{wind}, E_{v}, Φ_{IW}, and D were considered base values associated with $N(H_m) \equiv 0$. Based on the results, an asymptotic fit to the energies was found assuming the form

$$E = E_0 \left[1 + e^A (\mu N(H_m))^B\right]. \tag{2.33}$$

Here, E and E_0 represent any of the above named energies and its base value. μ is a unity constant with unit s. Dividing by the the base value from Eq.

Table 2.4: Energetics of model runs with different H_m. The dissipation D is the residual of all other terms (Eq. 2.24). The last row indicates a run with zero stratification throughout the water column.

H_m (m)	Φ_{wind} (TJ)	E_v/Φ_{wind} (%)	Φ_{IW}/Φ_{wind} (%)	D/Φ_{wind} (%)
25	410	13	-0.016	-87
50	401	12	-0.015	-88
100	387	10	-0.013	-90
200	371	8	-0.01	-92
500	354	5	-0.006	-95
1000	348	4	-0.004	-96
3000	340	4	-0.0000	-96

Table 2.5: Parameter results and base values from scaling fits (Eq. 2.33). The last column corresponds to the zero stratification run. Errors are given by 95% confidence intervals from the linear fit.

	A (1)	**B** (1)	$\mathbf{E_0}$ (TJ)
Φ_{wind}	3.86±0.17	1.21±0.03	340.40
E_v	8.72±1.17	1.67±0.22	12.65
Φ_{IW}	24.21±0.23	0.86±0.04	$9.51{\cdot}10^{-11}$
D	1.65±0.52	0.91±0.10	327.75

(2.33) and subtracting 1 allows for fitting the parameters A and B by using a log-log procedure. In such a scenario B directly determines the scaling behavior with respect to the maximum buoyancy frequency of the water column $N(H_m)$. Fit results are summarized in Table 2.5 and visualized in Fig. 2.7. The errors of the fits for the energy remaining in the center vortex are higher since the scaling effect is masked by the not yet terminated adjustment process. Correspondingly, the values for the dissipation have increased errors.

2.3 Summary and Conclusion

We examined the generation of internal gravity waves by a stationary cyclonic wind stress pulse in a non-linear, axisymmetric and Boussinesq model. The radial wind profile is characterized by the Rankine vortex structure with a critical radius $R_r = 50\,\mathrm{km}$ and a maximum wind speed $v_{10} = 30\,\mathrm{m\,s^{-1}}$. A wind pulse with a duration of $\Delta T_s = 2\,\mathrm{days}$ is considered. Stratification profiles with decreasing buoyancy frequency with depth following Gill (1984) are used. The mixed layer depth varies between $H_m = 50\,\mathrm{m}$ and $H_m = 1000\,\mathrm{m}$.

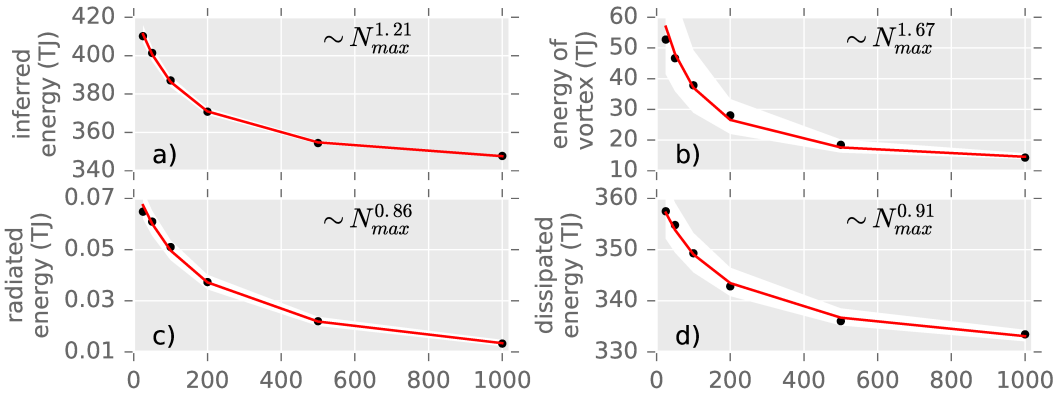

Figure 2.7: Energy input (a), energy transferred to the vortex (b), energy radiated as internal waves (c) and energy dissipated (d) as function of mixed layer depth. The energy dissipated is calculated as the residual of the energy balance (Eq. 2.24). Scaling laws in terms of powers of the maximum buoyancy frequency throughout the water column are indicated (Eq. 2.33). White shadings depict the 95% confidence intervals of the fits. For a list of all fit parameters see Table 2.5.

In general the evolution of the flow can be considered in three overlapping phases. During the linear increase of the wind velocity from zero to its maximum at time $t = \Delta T_s/4$ and the subsequent period of constant wind, the ocean surface is accelerated in azimuthal and consequently in radially outward direction. A radial flow and a corresponding return flow in the interior evolves immediately. The second phase, that is after roughly one inertial period is characterized by the oscillation of the radial motion with the inertial frequency and the associated inertial pumping. Low vertical mode internal gravity waves are excited by the corresponding vertical motion through the stratified ocean. Additionally, the oscillation of a bottom-intensified pressure anomaly associated to the excited vortex excites upward propagating higher mode waves. The inertial oscillation damps out as internal gravity wave packets are radiated radially outward and the vortex reaches an approximate geostrophic balance in the horizontal. The third adjustment phase starts right after the end of the wind forcing at $t = \Delta T_s$. It is characterized by the diffusion of the vortex in the vertical until it reaches the geostrophic equilibrium.

The wave-number-frequency spectrum at the mixed layer base reveals that the generated wave packets follow distinct dispersion relations similar to vertical normal modes.

Around 90% of the energy inferred by the wind is dissipated close to the surface.

This is due to the vertical momentum transfer through internal stresses only. Around 10% of the wind energy stays within the vortex and only about 0.01% of the energy is radiated from the vortex as internal gravity waves. Increasing the mixed layer depth or equivalently decreasing the maximum stratification leads to a reduction of the energy radiated as internal gravity waves and stored in the vortex. However, the latter is biased by the state of adjustment towards the geostrophic equilibrium at the end of the model time.

The energy radiated as internal gravity waves relative to the wind power is several orders of magnitude lower than 10 % - 30 %, as typically observed in the ocean and general circulation models (D'Asaro et al., 1995; Alford et al., 2012; Rimac et al., 2016). It is interpreted that other processes that drive vertical motion like surface heat fluxes, turbulent motion, mixed region collapse and storm translation are essential to the internal gravity wave generation. In particular the wake behind a laterally translating storm was reported to contain elevated internal gravity wave energy levels in similar but 3-dimensional setups (Price, 1983; Niwa and Hibiya, 1997).

Chapter 3

The Slab Model and the Hybrid Extension

In the previous Chapter an idealized simulation of the ocean response to an isolated storm was presented. Inertial pumping was identified to generate the most energetic internal gravity waves in the model results. Thus the question arises whether this mechanism can be simulated on a larger scale using realistic atmospheric wind stresses. The classical slab model as introduced by Pollard and Millard (1970) is an often used model to simulate inertial currents in local, regional and global contexts. Here it is revisited (Section 3.1.1) and its basic properties and parameter dependencies are explored (Section 3.1.2). The formulation of the hybrid extension proposed by Olbers et al. (2012) is briefly introduced (Section 3.1.3). It assumes the divergence of horizontal velocities to be the boundary condition to a stratified layer underneath the mixed layer base and predicts the corresponding energy flux. The generation of IGWs by this inertial pumping is investigated using a range of idealized surface stress scenarios and a regional application of the model to the North Atlantic (Section 3.3). Putting those into context with each other allows for the identification of regions with distinct wind stress structures and a characteristic ratio of the computed energy fluxes (Section 3.4).

3.1 Description of Slab- and Hybrid Model

3.1.1 The Slab Model

Since introduced by Pollard and Millard (1970) and revisited by D'Asaro (1985), their slab model equations have been widely used to estimate the wind work done on the ocean surface mixed layer. They assume a homogeneous slab of depth H_m with constant density ρ and a wind stress that decays from a surface value $\boldsymbol{\tau}_0$ to zero at the base of the mixed layer. The physics is reduced to the corresponding Reynolds stress term, the Coriolis effect and a damping

term. The latter parameterizes the sinks of kinetic energy in the mixed layer such as turbulent motion, entrainment or radiation of internal waves at the mixed layer base. Integrated over the mixed layer the governing equation reads as follows:

$$\frac{\partial}{\partial t}\boldsymbol{u} + f\ \mathsf{R}\boldsymbol{u} + r\ \boldsymbol{u} = \boldsymbol{\xi}. \tag{3.1}$$

$\boldsymbol{u}(x, y, t)$ is the depth averaged horizontal velocity in the mixed layer with time derivative $d\boldsymbol{u}/dt$. f is the Coriolis frequency and r a damping parameter. The source term $\boldsymbol{\xi} = (\xi_x, \xi_y) = \boldsymbol{\tau}_0/\rho H_\mathrm{m}$ contains the constant density ρ, the time dependent mixed layer depth $H_\mathrm{m}(t)$ and wind stress components. Furthermore, R is a 90° rotation operator in the counter clockwise direction. The rigid lid approximation is made so that the vertical velocity vanishes at the surface, i.e. $w|_{z=0} \equiv 0$. Moreover, it is assumed that the mixed layer depth H_m varies much slower than the horizontal velocities so that $\partial/\partial t(H_\mathrm{m}\boldsymbol{u}) \approx H_\mathrm{m}\partial/\partial t(\boldsymbol{u})$. Thus, H_m can be regarded constant in the time derivative.

The slab mixed layer equation is solved in Fourier space. In particular, taking the transform of Eq. (3.1) in time and horizontal yields:

$$[(i\sigma + r)\mathbb{1} + f\ \mathsf{R}]\ \hat{\boldsymbol{u}} = \hat{\boldsymbol{\xi}}, \tag{3.2}$$

with Fourier transform

$$\hat{\boldsymbol{u}}(\boldsymbol{k}_\mathrm{h}, \sigma) = \iiint_{\mathbb{R}^3} \boldsymbol{u}(\boldsymbol{x}, t)\ e^{-i(\boldsymbol{k}_\mathrm{h}\cdot\boldsymbol{x} + \sigma t)}\ d\boldsymbol{x}\ dt.$$

Here, σ represents the angular frequency and $\mathbb{1}$ the unity operator. Note that the operator on the left hand side of Eq. (3.2) has a matrix representation with the non-zero determinant $(i\sigma + r)^2 + f^2$. It can therefore be inverted and a transfer operator T can be defined by $\mathsf{T}^{-1} = (i\sigma + r)\mathbb{1} + f\mathsf{R}$. Left multiplication by the transfer operator leads to:

$$\hat{\boldsymbol{u}} = \mathsf{T}\ \hat{\boldsymbol{\xi}} = \frac{(i\sigma + r)\mathbb{1} - f\ \mathsf{R}}{(i\sigma + r)^2 + f^2}\ \hat{\boldsymbol{\xi}}. \tag{3.3}$$

The solution given by Eq. (3.3) also includes the well known Ekman solution to the constant component of the wind stress or equivalently the zero frequency response. It is constant in time and therefore affects only the zero frequency response. Consequently, it has no effect on excitation of internal waves with frequencies between the inertial and buoyancy frequencies. For reasons of consistency no distinction between near-inertial and Ekman components is made.

The horizontal slab velocities are then evaluated taking the inverse Fourier transform of Eq. (3.3).

The wind power is evaluated by considering the kinetic energy balance of the surface slab. The total energy budget is obtained by multiplying Eq. (3.1) with the velocity vector $\boldsymbol{u}$. In particular:

$$\frac{d}{dt}\left(H_{\mathrm{m}}\,\frac{\rho}{2}\boldsymbol{u}\cdot\boldsymbol{u}\right)=\boldsymbol{\tau}_0\cdot\boldsymbol{u}-r\,\left(\rho H_{\mathrm{m}}\right)\,\boldsymbol{u}\cdot\boldsymbol{u}. \tag{3.4}$$

Whereas the term $-r\,\left(\rho H_{\mathrm{m}}\right)\,|\boldsymbol{u}|^2$ describes the energy loss associated to the Rayleigh damping, the first term describes the wind power:

$$\phi_{\mathrm{wind}}(t)=\boldsymbol{\tau}_0(t)\cdot\boldsymbol{u}(t). \tag{3.5}$$

The slab model velocities (Eq. 3.3) resonate at the frequency $\sigma=-f$. However, this resonance is of minor importance in a typically pink to red wind stress spectrum. Instead, the wind power scales with the damping parameter r. Hence, a generally variable damping leads to a variability in the simulated wind power. Therefore, the damping parameter must be chosen with care.

3.1.2 Basic Properties of the Classical Slab Model

For the analysis of the resonance, a complex notation of the slab mixed layer system is used. The governing equation (Eq. 3.1) reads then

$$\frac{\partial}{\partial t}(u+iv)+(if+r)(u+iv)=\xi_x+i\xi_y \tag{3.6}$$

with u, v, f, r and ξ_i being the two velocity components, the local Coriolis frequency, the damping parameter and the components of the forcing function, respectively. Using this notation has the advantage that the rotation associated with the Coriolis force is equivalent to multiplication with the imaginary unit i. The assumption of a periodic and monochromatic forcing $\xi_x+i\xi_y=\xi_0\exp(i\omega t)$ is made. Solving the system gives

$$u+iv=\frac{\xi_x+i\xi_y}{r+i(f+\omega)}. \tag{3.7}$$

The corresponding expression for the wind power ϕ_{wind} and kinetic energy density $\mathcal{E}_{\mathrm{KE}}$ are

$$\phi_{\text{wind}}(t) = \rho H_{\text{m}} \frac{r(\xi_x^2 + \xi_y^2)}{r^2 + (f+\omega)^2}, \tag{3.8}$$

$$\mathcal{E}_{\text{KE}}(t) = \frac{\rho}{2} \frac{\xi_x^2 + \xi_y^2}{r^2 + (f+\omega)^2}, \tag{3.9}$$

Recovering the vector notation, this is equivalent to

$$\phi_{\text{wind}}(t) = \rho H_{\text{m}} \frac{r|\boldsymbol{\xi}|^2}{r^2 + (f+\omega)^2}, \tag{3.10}$$

$$\mathcal{E}_{\text{KE}}(t) = \frac{\rho}{2} \frac{|\boldsymbol{\xi}|^2}{r^2 + (f+\omega)^2}. \tag{3.11}$$

Dividing by the square of the wind stress vector yields the transfer functions for the wind power and the kinetic energy density. Both transfer functions have a resonance peak at the forcing frequency $\omega = -f$. The resonance peak of the wind power scales with $1/r$ and has a full width at half maximum (FWHM) of r. Beyond the resonance it scales with r. In contrast, the kinetic energy density peaks at the same frequency but with the scaling r^{-2}. However, it is independent of the damping parameter in the asymptotic limits, i.e. at $(\omega+f)^2 \approx \omega^2 \gg r^2$. Note that this resonance is subject to the amplitude of the forcing at its frequency ω. Given the assumption $r \ll f$ and the consequently small FWHM the resonance affects only a small interval in the spectral transfer. For the typically pink to red wind stress spectrum (Gille, 2005) the wind power (Eq. 3.10) scales with r. Thus, the resonant energy transfer is strongly dependent on the damping parameter. Only in the limit $r \to 0$ the response takes the shape of a delta distribution and is limited to the spectral power of the wind stress at the frequency $-f$. For a damping time scale of the order $r^{-1} \sim 1\,\text{day}$ this behavior is not observed.

Another parameter supplied to the slab model is the mixed layer depth H_{m}. In particular, the forcing function $\boldsymbol{\xi}$ is inversely dependent on H_{m} (cf. Section 3.1.1). Hence, the wind power is proportional to H_{m}^{-1} and the kinetic energy density scales with H_{m}^{-2}.

3.1.3 The Hybrid Solution

According to Eq. (3.3) the average mixed layer velocity depends on the damping parameter, Coriolis effect, mixed layer depth and wind stress. Consequently the horizontal divergence of the field is generally non-zero. The continuity equation, integrated from the mixed layer depth $H_{\text{m}}$to the surface yields:

$$w|_{z=-H_\mathrm{m}} = H_\mathrm{m}\ \boldsymbol{\nabla}\cdot\boldsymbol{u}. \tag{3.12}$$

Again, the rigid lid approximation is used. Consequently, any divergent near-inertial surface velocity field $\boldsymbol{u}$ induces inertial pumping. These vertical oscillations can be considered as boundary condition to a stratified layer below the mixed layer base. A corresponding analysis of the dynamics of the stratified ocean underneath the mixed layer is presented in the Appendix B.1. The resulting hybrid model has been evaluated and compared to a linearized pressure resolving model (Jurgenowski et al., 2017, in preparation). The Fourier transformed local vertical energy flux $\phi_{\mathrm{IW,F}}$ and its integral $\Phi_{\mathrm{IW,F}}$ are given by:

$$\phi_{\mathrm{IW,F}} = -\rho\frac{F(\sigma)}{k_\mathrm{h}}\ \left(\hat{w}(\boldsymbol{k}_\mathrm{h}, H_\mathrm{m}, \sigma)\hat{w}^*(\boldsymbol{k}_\mathrm{h}, H_\mathrm{m}, \sigma)\right), \tag{3.13}$$

$$\Phi_{\mathrm{IW,F}} = -\rho\int_f^N\iint_{\mathbb{R}^2}\frac{F(\sigma)}{k_\mathrm{h}}\ \left(\hat{w}(\boldsymbol{k}_\mathrm{h}, H_\mathrm{m}, \sigma)\hat{w}^*(\boldsymbol{k}_\mathrm{h}, H_\mathrm{m}, \sigma)\right)\ d\boldsymbol{k}_\mathrm{h}\ d\sigma. \tag{3.14}$$

Here, the asterisk denotes the complex conjugate so that

$$\left(\hat{w}(\boldsymbol{k}_\mathrm{h}, H_\mathrm{m}, \sigma)\hat{w}^*(\boldsymbol{k}_\mathrm{h}, H_\mathrm{m}, \sigma)\right)$$

is the power spectral density of the vertical velocity at the mixed layer base. N is the local buoyancy frequency below the mixed layer, the Coriolis frequency f is assumed to be locally constant. The factor $F(\sigma) = \sigma^{-1}(N^2-\sigma^2)^{\frac{1}{2}}(\sigma^2-f^2)^{\frac{1}{2}}$ emerges from the multiplication of the vertical group velocity with the total energy density. The vertical velocity is computed from the slab model results using Eq. (3.12).

Here one may assume a dominant horizontal wave number k_h with the corresponding wave length $L_\mathrm{h} = 2\pi/k_h$ in the vertical velocity. Furthermore, the window function $\hat{h}(\sigma) = \sqrt{F(\sigma)/(N-|f|)}$ is defined so that:

$$\phi_{\mathrm{IW,F}} = -\rho\frac{L_\mathrm{h}}{2\pi}(N-|f|)\hat{h}^2\left(\hat{w}(\boldsymbol{k}_\mathrm{h}, H_\mathrm{m}, \sigma)\hat{w}^*(\boldsymbol{k}_\mathrm{h}, H_\mathrm{m}, \sigma)\right). \tag{3.15}$$

Utilizing Parseval's theorem for the total energy transfer the vertical energy flux ϕ_{IW} and the total vertical energy transfer Φ in physical space are deduced:

$$\phi_{\mathrm{IW}} = -\rho\frac{L_\mathrm{h}}{2\pi}(N-|f|)\left|h(t) * w(\boldsymbol{x}, H_\mathrm{m}, t)\right|^2, \tag{3.16}$$

$$\Phi_{\mathrm{IW}} = \int\iint_{\mathbb{R}^2}\phi_{\mathrm{IW}}\ d\boldsymbol{x}\ dt. \tag{3.17}$$

where h is the inverse Fourier transform of $\hat{h}$ and $d\boldsymbol{x}$ represents the horizontal surface element. The asterisk $*$ denotes the convolution in time. Note that $\hat{h}(\sigma)$ is a normalized window within the interval (f, N). The above convolution is then equivalent to a Fourier frequency filter acting on $w(\boldsymbol{x}, H_{\mathrm{m}}, t)$. Note that the filtered vertical velocity $h(t) * w(\boldsymbol{x}, H_{\mathrm{m}}, t)$ implicitly depends on the filter interval (f, N) as well as the shape of the filter window (Fig. B.3). However, the effects are negligible given the assumptions $f \ll N$ in combination with a red spectrum of the wind stress. Therefore, the vertical energy flux ϕ_{IW} is approximately linearly dependent on the buoyancy frequency N. A more detailed description of the Fourier filter can be found in the Appendix B.3. Given *a priori* assumptions about horizontal scales and stratification, this formulation now permits estimates of the energy flux into the stratified ocean below the mixed layer.

3.2 Data and Input Parameters

3.2.1 Wind Stress, Mixed Layer Depth and Buoyancy Data

The slab model is forced by the ratio of the local wind stress and the mixed layer depth. In addition, the stratification at the base of the mixed layer is needed to evaluate the energy flux into the interior. The wind stress data should have a temporal resolution of at least 1 h to ensure reasonable coverage of the previously described resonance at $\sigma = -f$ (Rimac et al., 2013). Moreover a spatial resolution higher than 50 km is necessary since the horizontal resolution of the vertical velocity puts limits on the estimate of dominant horizontal wave numbers with expected wavelengths of the order 100 km.

Wind stress fields from the NCEP-CFSR reanalysis (Saha et al., 2010) were chosen to force the slab model. A horizontal resolution of 0.3° with hourly values ensures computation of horizontal gradients and dominant wave numbers as well as the full coverage of the resonance peak in the slab equation (Eq. 3.3). The years 1989 and 1996 have been chosen as examples for conditions with high and low NAO index respectively (Hurrell and Deser, 2009). Positive NAO phases are characterized by stronger wind stresses in the North Atlantic between 40°N and 60°N. Thus a stronger ocean response is expected. This difference serves as benchmark for the importance of the wind stress magnitude on ratios of energy fluxes.

Since the energy flux through the ocean surface is proportional to the horizontal velocity in the mixed layer, which is inversely proportional to the mixed layer depth (Eqs. 3.5 and 3.5), the choice for a data set of the mixed layer depth H_{m} is crucial for energy flux considerations. Unphysically deep and missing values in deep convection areas in the NCEP-CFSR reanalysis excluded the use of a data set consistent with the wind stress forcing. Instead the MIMOC climatology (Schmidtko et al., 2013) was used. In accordance with the approximation of a slowly varying mixed layer depth high frequency responses like diurnal cycles and individual entrainment events are not represented. As these effects are neglected, this study focuses on spatial averages and seasonal cycles. The MIMOC climatology makes use of the objective mixed layer pressure algorithm based on density profiles (Holte and Talley, 2009) and delivers monthly averaged values with 0.5° horizontal resolution. Moreover, it preserves synoptic features and the influence of the bathymetry while filtering transient phenomena like eddies and internal gravity waves. The data points were set to mid-month dates and linearly interpolated in time and space to obtain hourly time series in the slab model calculation. This avoids strong ringing effects in the corresponding Fourier transforms in time and minimizes its noise. However, the linear interpolation of monthly averages weakens the seasonal cycle and adds a bias to the annual mean of the energy influxes.

In accordance with the mixed layer depth data the MIMOC data set provides the corresponding optimally interpolated conservative temperature and absolute salinity profiles. They have vertical resolution from 5 dbar to 50 dbar increasing with depth. The buoyancy frequency is calculated using finite differences and the Thermodynamic Equation of Seawater 2010 (McDougall and Barker, 2011). Overturns within the mixed layer may lead to negative values for the linearly interpolated square of the buoyancy frequency at the mixed layer depth. To circumvent the numerical effect the buoyancy frequency is vertically interpolated to a 5 dbar grid and the closest positive value below the mixed layer depth is chosen. The resulting stratification is then associated with the mixed layer base.

Table 3.1: Parameterization for horizontal wave length with function $L_\mathrm{h} = \alpha lat + \beta$. The errors indicate double standard deviations from linear fits.

year	α [$\frac{\mathrm{km}}{^\circ\mathrm{lat}}$]	β [km]
1989	4.1 ± 0.8	231.0 ± 31.2
1996	2.9 ± 0.7	277.3 ± 24.6

3.2.2 The Damping Parameter r and the horizontal wavelength L_h

In order to evaluate the damping parameter r, 61 moored time series of wind and surface currents were analyzed following the procedure of Alford (2001). However, the results showed a large spread in optimal damping parameters. Additionally, damping time scales evaluated from drifter trajectories (Park et al., 2009) suggested an almost constant parameter throughout the North Atlantic. Hence a constant damping time $r^{-1} = 5\,\mathrm{days}$ was chosen. More details on the procedure and comparison of the data sets can be found in the Appendix B.2.

The dominant wavelength was estimated from boxed Fourier transforms of the simulated vertical velocity. These were done at 45 locations in the North Atlantic with latitudes ranging from 15°N to 45°N. From the results, a linear parameterization depending on the latitude was derived for both years. The results vary between approximately 250 km and 500 km (Table 3.1). This is within the range of results found with general circulation models (Rimac et al., 2013; Simmons and Alford, 2012) and in surface drifter tracks (Park et al., 2009). Details on the boxed Fourier transform analysis are described in the appendix.

3.3 Results

3.3.1 Idealized Simulations

Six idealized simulations were performed to isolate the effects of a spatially and temporally varying wind stress as well as an increase in the local Coriolis frequency with latitude (Fig. 3.1). For simplicity, symmetry in the x-direction was assumed and the northward component of the wind stress was set to zero at all times. In runs (a), (b), (e) and (f) a northward advancing wind stress front was simulated by a Gaussian wind stress peak with standard deviation $s_x = 20\,\mathrm{km}$ and a fixed northward speed. The time the peak travels through

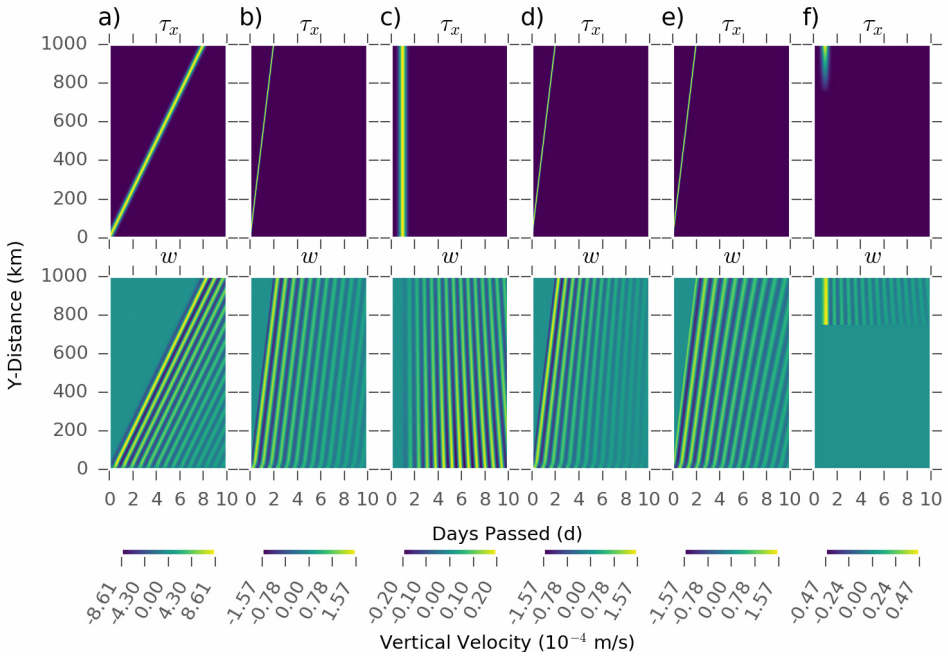

Figure 3.1: Wind stress (upper panel) and vertical velocity (lower panel) of concept runs for a slowly moving wind stress front (a), a fast moving wind stress front (b), a homogeneous wind stress pulse (c), a fast wind stress front with varying Coriolis frequency (d), a fast wind stress front with inversely varying Coriolis frequency (e) and a stationary wind stress pulse with spatial gradient (f). The color bars show the amplitude of the corresponding vertical velocity.

a domain with 1000 km length is set to 8 days (a) and 2 days (b, d, e). That results in velocities v_{atm} with values of 1.45 m/s and 5.79 m/s, respectively. Simulations (c) to (f) allow for a varying Coriolis frequency. The latitude at the southern edge of the domain is 45°N (a-d, f) or 45°S (e). The beta effect is quantified using a spatially homogeneous pulse of wind with Gaussian amplitude and a standard deviation in time of $s_t = 5$ hours (c). The last simulation (f) is equivalent to (c) but imposes a gradient on the wind stress. In particular it is zero everywhere except in the northern most quarter of the domain where it increases linearly to the maximum wind stress at the northern boundary. The maximum wind stress is 1 N/m^2 in all cases. The mixed layer depth is constant with $H_\mathrm{m} = 50$ m.

Translation of Atmospheric Structures The translation of lateral wind stress structures is simulated using advancing wind stress fronts as described above. The mechanism of excitation of vertical oscillations is the time shifted acceleration of the horizontal velocities along the track of the advancing front. Every point within the domain experiences the same excitation but has a time

and phase shift depending on the speed v_{atm} of the front. This phase shift leads to a divergence of the meridional velocity with a wavelength $L_\mathrm{h} = 2\pi v_{atm}/f$. The local temporal evolution of the wind stress corresponds to a Gaussian profile with standard deviation $s_t = s_x/v_{atm}$. For comparison two atmospheric velocities are tested (see above). In the first case (a) the speed is chosen so that the width of the peak is about half the inertial period. Thus, the horizontal velocities are forced through half an inertial rotation but not slowed down during the second half. This is very efficient and results in large vertical velocities with a correspondingly large energy flux ratio of 64.4% (Fig. 3.1a; Table 3.2 (a)). The fast atmospheric front (b) injects about one third of the energy and excites vertical velocities with less than one fifth of the previously observed magnitude. The corresponding energy flux ratio is approximately 26% (Fig. 3.1b; Table 3.2 (b)).

The Beta Effect The beta effect was quantified using a spatially uniform wind stress pulse and taking into account the change of the Coriolis frequency along the y-axis with $\beta = df/dy$. Note that the hybrid extension does not include the beta effect but quantifies the local energy flux for a locally constant Coriolis frequency. This is equivalent to a stepwise constant f. The homogeneous wind stress pulse excites an inertial oscillation at all points synchronously. The phase shift between the oscillations linearly grows with time due to the slightly different rotation frequencies. Correspondingly, the divergence of the meridional velocity and thus the amplitude of vertical oscillations increases on a time scale proportional to β^{-1}. The damping of the oscillations with damping time scale r^{-1} limits this growth. Consequently, lines of constant phase rotate counter clockwise in a t-y-diagram (Fig. 3.1c). The time dependent phase shift has a corresponding length scale $L_\mathrm{h} = (\beta t)^{-1}$. Both the average energy radiated and the energy flux ratio are an order of magnitude lower compared to an advancing wind stress front (Table 3.2). Note that in low latitudes where the time scale of the beta effect is shorter than the damping time scale, phase shifts eventually cancel out and cause a beat like structure of vertical oscillations.

Influence of the Beta Effect on an Advancing Front Adding the beta effect to the previously described simulation of a fast wind stress front does not effect the magnitude of the excited vertical oscillation. Instead, the gradient in rotation frequency alters the phase shift of the horizontal velocities and leads to a faster decay of vertical oscillations (Fig. 3.1d). Also, the characteristic horizontal wavelength increases. The corresponding downward energy

Table 3.2: Energy flux into the ocean and energy flux ratios from idealized runs. (a) - (f) are averaged over the whole domain in space and time. (g) is spatially averaged over the interval of the wind stress gradient.

		$f = f(y)$	$\langle \phi_{\mathrm{IW}} \rangle_{t,y}$ ($\mathrm{W/m^2}$)	$\frac{\langle \phi_{\mathrm{IW}} \rangle_{t,y}}{\langle \phi_{\mathrm{wind}} \rangle_{t,y}}$ (1)
(a)	slow front	no	$-6.19 \cdot 10^{-4}$	0.644
(b)	fast front	no	$-9.47 \cdot 10^{-5}$	0.260
(c)	homogeneous pulse	yes	$-4.62 \cdot 10^{-6}$	0.014
(d)	fast front	yes	$-8.02 \cdot 10^{-5}$	0.224
(e)	fast front	inverse	$-1.20 \cdot 10^{-4}$	0.322
(f)	gradient pulse	yes	$-1.17 \cdot 10^{-6}$	0.015

flux leaving the mixed layer reduces by approximately 3.6% (Table 3.2).

Considering a southward translation of the wind stress, here simulated by changing the sign of f equivalent to performing the experiment on the southern hemisphere leads to an opposite result. Rather than reducing, phase shifts increase and vertical oscillations decay slower with decreasing horizontal wavelength (Fig. 3.1e). The corresponding energy flux increases by 6.2%.

Spatial Gradients of Atmospheric Structures Imposing a gradient in atmospheric forcing leads to a divergence of meridional velocities due to the position dependent magnitude of excited inertial oscillations. A stationary forcing with a constant gradient leads to a synchronous vertical displacement. The resulting vertical velocity depends solely on the strength of the gradient. The lateral length scale L_{h} is set by the lateral extent of the gradient. In the present simulation the wind stress has a gradient of $4 \cdot 10^{-6}\,\mathrm{N\,m^{-3}}$ on a domain with size 250 km. The ratio of average energy fluxes over the gradient domain is then 1.5% (Table 3.2). A stronger gradient leads to an increase in local energy flux into the ocean as well as the energy flux ratio by an order of magnitude but within a more confined area (not shown).

3.3.2 Simulations of the North Atlantic

In general, the two years 1989 and 1996 show similar spatial and temporal patterns in both the energy fluxes into the mixed layer and the vertical energy fluxes from the mixed layer into the internal wave field (Figs. 3.2 and 3.3). The amplitude of the wind power is about one order of magnitude larger compared to the radiated energy flux. Moreover spatial patterns tend to be more confined in the outflux. Filaments and rather sharp horizontal gradients are

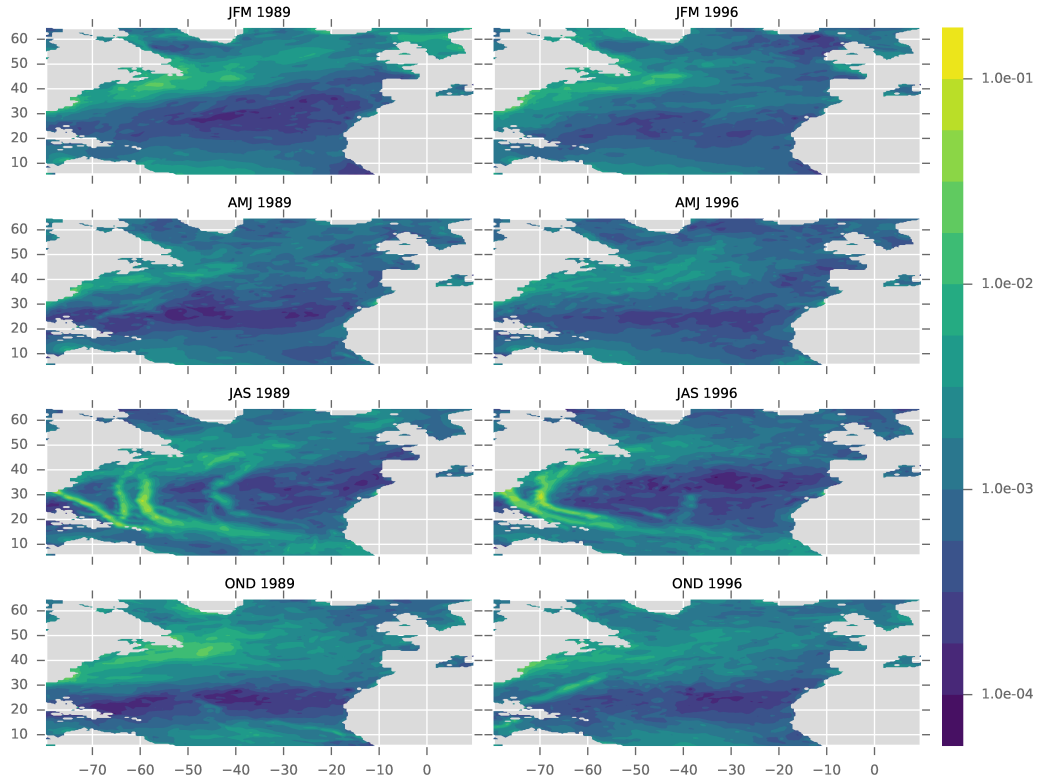

Figure 3.2: Seasonally averaged vertical energy flux into the mixed layer for 1989 (left) and 1996 (right) computed with the slab model. The unit of the color scale is W m^{-2}.

visible. Both energy fluxes indicate a range of characteristic meteorological regimes.

Tropics Here, the tropical regime is defined as the latitudinal band between the equator and 20°N. It is characterized by moderate energy fluxes with values around 1 mW m^{-2} (Fig. 3.2). The wind power has low seasonal variability beyond the hurricane season from July to October (monthly plots are not shown). In contrast, the energy flux from the mixed layer into the ocean has very low magnitude with values around 0.05 mW m^{-2}. Values from both years are very similar. Seasonal differences between 1989 and 1996 can be found in the different distinct Hurricane storm tracks.

Subtropics The subtropics are defined by the latitudinal band between 20°N and 40°N. In general, both energy fluxes are lowest compared to all other regions in the North Atlantic. However, within this regime Hurricanes and tropical depressions have the highest intensity and thus the strongest energy fluxes

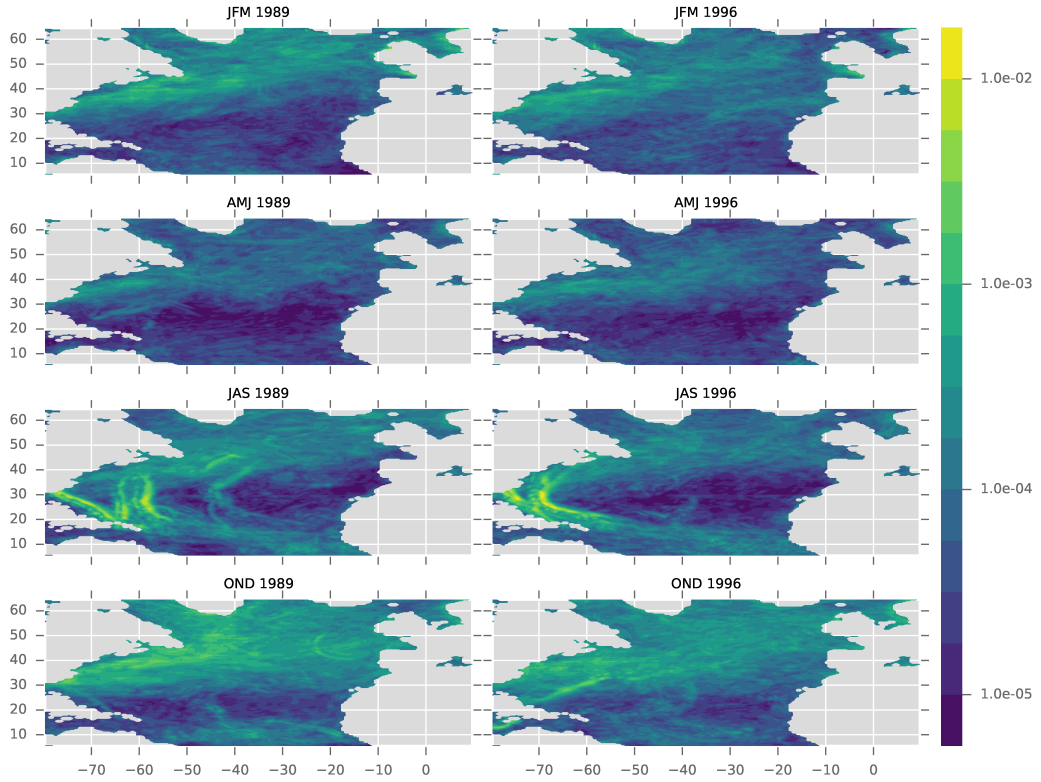

Figure 3.3: Seasonally averaged vertical energy flux from the mixed layer into the internal wave field for 1989 (left) and 1996 (right) computed with the hybrid extension. The unit of the color scale is W m^{-2}.

are observed. The energy in- and outfluxes have values of up to 100 mW m^{-2} and 10 mW m^{-2}, respectively. As in the tropics, the years 1989 and 1996 are similar in extent and magnitude in the patterns of both energy fluxes beyond the Hurricane tracks.

Mid-Latitudes and Subpolar Regions North of 40°N the mid-latitudes are dominated by large energy fluxes associated with large scale storms. In all seasons patches of wind power with values around 10 mW m^{-2} are distributed over large areas of the region. The positive NAO year (1989) exhibits larger amplitudes and stronger gradients. The energy flux into the ocean shows the same features with amplitudes an order of magnitude smaller. In subpolar regions north of approximately 55°N both fluxes visibly decrease.

Zonal and Temporal Means The different meridional regimes and differences between the two years as well as the energy in- and outfluxes can be summarized using zonal means (Fig. 3.4). Higher amplitudes in the mid-latitudes and subpolar regime for 1989 as well as much reduced energy outfluxes in the

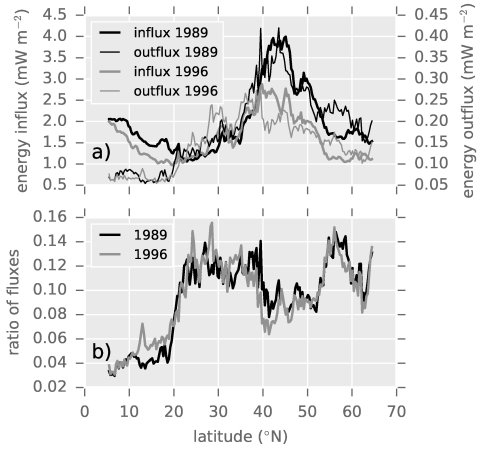

Figure 3.4: (a) Zonally averaged energy fluxes into the mixed layer (thick lines) and out of the mixed layer (thin lines). Note that fluxes into the internal wave field correspond to the right axis with scaled magnitude. (b) Ratios of fluxes from upper panel.

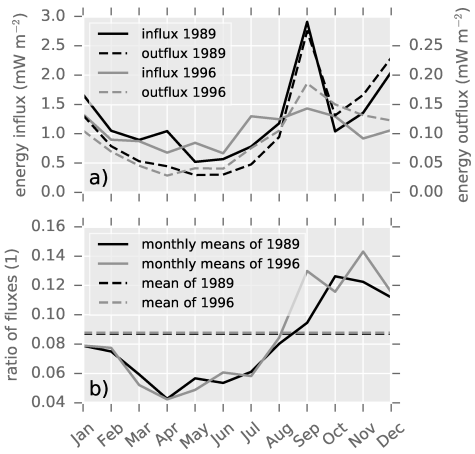

Figure 3.5: (a) Monthly fluxes into the mixed layer (solid) and out of the mixed layer (dashed) averaged over the whole domain. Note that fluxes into the internal wave field correspond to the right axis with scaled magnitude. (b) Ratios of monthly fluxes (solid) and ratios of average fluxes (dashed).

tropical regime are now quantitatively visible. Stronger winds north of 40°N in 1989 lead to increased energy fluxes by approximately 50%. Despite the differences between the two years, the ratios of energy outflux to influx show a similar structure. Every regime has a typical ratio of energy fluxes. Whereas the tropics and subtropics have a rather constant ratio of around 5% and 12% respectively, the mid-latitudes and subpolar region has a pronounced increase from 8% at 40°N to approximately 14% at 58°N. This is where mixed layers depths are deepest. It then drops to 8% at 63°N.

Both vertical energy fluxes through the surface and the mixed layer base show a dominant annual cycle with elevated levels during autumn and winter (Fig. 3.5). During 1989, the annual cycle is more pronounced and the average flux is larger by up to a factor of 2 compared to 1996. There is a characteristic rise in energy fluxes during the hurricane season, narrower and stronger in 1989 than in 1996.

Even though the two years exhibit very distinct annual cycles the ratios of monthly energy fluxes agree closely. Both show a minimum between March and May of around 4% and a maximum of approximately 13% between September

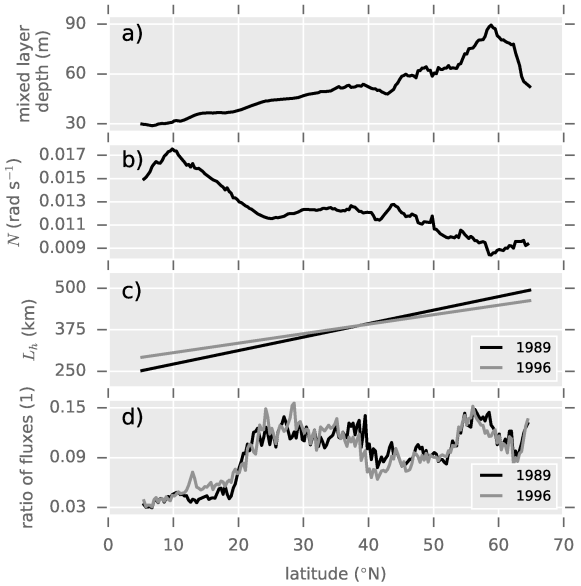

Figure 3.6: Zonal averages of (a) mixed layer depth (b) difference between sub-mixed-layer buoyancy and Coriolis frequency (c) horizontal length scales L_h; and (d) ratios of yearly averaged out- to influxes

and October. The average ratio of the mean energy fluxes amounts to 9% for both years.

3.4 Discussion

The ratio of zonally averaged energy fluxes shows different regimes depending on latitude. In this section the aim is to interpret the differences in the context of a range of factors. The temporal and spatial structure of the wind field as well as the beta effect prescribe the generation mechanism of vertical velocities at the mixed layer base as previously explored. Also the wind's frequency spectrum influences the results due to resonant response effects. Moreover, there are three parameters that the ratio depends on: the mixed layer depth, the buoyancy frequency N and horizontal wavelength $L_\mathrm{h} = 2\pi/k_\mathrm{h}$.

3.4.1 Meridional Regimes

Mixed Layer Depth The energy flux into the mixed layer is directly proportional to the depth averaged velocity and thus inversely proportional to the mixed layer depth. The zonal average of the climatologic mixed layer depth is shallow around 30 m at 5°N, increases almost linearly to approximately 65 m at 54°N and peaks at values of around 90 m near 59°N. North of the maximum

it drops to 50 m at 65°N (Fig. 3.6a). A similar pattern is observed in the low values of the flux ratios in subtropical regions and the strong transition at 53°N with the subsequent peak at approximately 58°N. It is worth mentioning that the deep mixed layers around 59°N correspond to typical winter conditions of the subpolar gyre including deep convection areas (de Boyer Montégut et al., 2004). Also note that the zonally averaged energy flux into the mixed layer does not reflect an inverse behavior since the dependence on the wind stress magnitude masks the effect.

The slab model assumes a depth $H_{\mathrm{m}}(t)$ at which an internal Reynolds stress τ, equaling the wind stress at the surface, vanishes. However, this assumption does not define a unique depth. The additional assumption that this depth corresponds to the mixed layer depth is only true if the mixed layer has been mixed solely by dissipation of wind power. For instance during convection events the zero-stress depth associated with the wind stress may be only a fraction of the mixed layer depth. If the zero-stress level is overestimated by approximating it with the mixed layer depth the wind power is underestimated and the energy flux ratio is overestimated accordingly. This is most likely for large areas in the North Atlantic where deep mixed layers are common throughout the winter. Some observations have been reported that implied a depth penetration of the wind induced shear below the mixed layer depth (Dohan and Davis, 2011; Forryan et al., 2015). Instead of eroding the pycnocline, the internal stress resulted in the broadening of a transition layer and consequently in the reduction of the mixed layer depth. Hence the preceding assumption may lead to an over- or underestimation of the wind power in the slab model. Here, it is important to recall that the vertical velocity at the mixed layer base is independent of the mixed layer depth. Thus, even though the energy flux into the mixed layer scales with the inverse mixed layer depth this effect cancels in the hybrid extension for the calculation of the energy flux into the internal wave field but remains present in all energy flux ratios. Therefore, the interpretation of the elevated ratios of zonally averaged energy fluxes around 58°N is difficult and possibly an artifact related to deep convection areas.

Sub-Mixed-Layer Buoyancy Frequency The ratio of energy fluxes is approximately linearly dependent on the buoyancy frequency N (Eq. 3.16). Its zonal average peaks at $18{\cdot}10^{-3}\,\mathrm{rad\,s^{-1}}$ at 10°N and decreases to $9{\cdot}10^{-3}\,\mathrm{rad\,s^{-1}}$, a relative decrease of 50% (Fig. 3.6b). The energy flux ratio does not exhibit any corresponding behavior, presumably because the effect is masked by the

relative increase of the mixed layer depth and the horizontal length scale (see below).

Horizontal Length Scale L_h is parameterized with a linear increase of values from around 275 km at 5°N to approximately 475 km at 65°N (Fig. 3.6c). This relative increase is similar to the relative decrease in the buoyancy frequency N. Thus the effects mask each other and are barely visible in the energy outflux from the mixed layer into the internal gravity wave field as well as the energy flux ratio.

However, there are several sources of uncertainty associated with this parameter. By considering dominant wavelengths an effective length scale was computed from the horizontal wave number distributions. In general, there is little knowledge about these forced horizontal wave number spectra. They depend very much on the generation mechanism of the induced vertical velocity and thus on the temporal and spatial structure of the wind as described in the previous section. Also the parameterization from the boxed Fourier transform analysis is problematic. With residues up to 25% in zonal averages it might have larger deviations from local values. Considering typical values of 100 km to 1000 km (Rimac et al., 2016; Simmons and Alford, 2012) one may anticipate an error up to a factor of 2 in all computed outfluxes.

Wind Field Structure As mentioned above the temporal and spatial structures of the wind stress field are major drivers for wave-like structures at the base of the mixed layer. It forces the local horizontal wave number spectrum but also the magnitude of the vertical velocity.

The tropics are generally characterized by rather steady winds with stable direction and low seasonal variability. Only tropical cyclones and hurricanes traveling northward have fast moving gradients and fronts. Quasi-steady structures with temporal variability paired with a strong gradient in the Coriolis frequency suggest that the generation of vertical oscillations is dominated by the beta effect. Consequently, low energy fluxes from the mixed layer into the internal wave field as well as low energy flux ratios are expected. Correspondingly, the simulation of the North Atlantic shows low seasonal variability (not shown) and low ratios of average energy fluxes south of 20°N (Fig. 3.4). During the sporadic occurrence of tropical pressure systems the energy flux ratios increase (Figs. 3.2 and 3.3). A small difference between the two years is

observed - possibly related to the El Niño Southern Oscillation (not shown). However, the difference is well within the error margins.

Subtropical regions are characterized by the gradient between conditions in tropical and mid-latitude regions. Wind speeds are generally low. The most prominent features are strong tropical storms and fronts associated with pressure systems from mid-latitude regions. The latter have reduced movement speed due to larger Rossby radii of deformation at lower latitudes. Therefore, generally low energy fluxes with a seasonal cycle characteristic for mid-latitudes superimposed by strong seasonal peaks associated with hurricanes are expected. Moreover, the slow moving fronts suggest higher ratios of average energy fluxes. Accordingly, the present simulations of the North Atlantic show this behavior in the seasonal cycle (not shown). The elevated ratios of zonally averaged energy fluxes are particularly prominent (Fig. 3.4). The highest energy fluxes observed are associated with the hurricanes occurring in this domain (Figs. 3.2 and 3.3).

Mid-latitude regions are renowned for alternating pressure systems with high seasonal variability. These pressure systems inhibit fast moving fronts and are particularly affected by the Northern Atlantic Oscillation. Thus, elevated energy fluxes into and out of the mixed layer as well as a dominant seasonal cycles with differences between opposite NAO phases is predicted. The higher speed of the fronts suggest reduced energy flux ratios. The results of the simulations agree well with this prediction. However, a maximum in the ratio of zonally averaged energies at latitudes around 55°N is found. It is associated with deep mixed layers in deep convection areas (see above).

The excitation of inertial oscillations in the mixed layer is resonant at $\sigma = -f$. Thus regions with elevated levels in the wind stress frequency spectra close to the inertial frequency induce stronger energy fluxes. In consequence, differences in the frequency spectra across relatively small horizontal length scales may lead to an elevated flux into the internal gravity wave field. Due to the effectively small frequency interval in which resonant excitation is dominant this effect strongly depends on the shape of the forcing spectrum.

3.4.2 The Two Years

In the context of the preceding discussion the observed differences between the two simulated years is illustrated below.

Annual Cycles Both years exhibit annual cycles in energy in- and outfluxes similar to those observed by Alford and Whitmont (2007). The winter months January and October through December are characterized by elevated energy fluxes due to increased storm activity in the northern North Atlantic. In contrast the months March through June show calm weather conditions with relatively low energy fluxes (Fig. 3.5).

Distinct from the background, the seasonal cycle of 1989 shows a sharp peak in September whereas the seasonal cycle of 1996 exhibits a more broad elevation of energy fluxes from July through October. These features are triggered by a few isolated tropical storms and hurricanes that insert large amounts of energy into the subtropical North Atlantic Ocean. The difference is due to the intermittent occurrence of events during the hurricane season.

The ratios of energy fluxes show a characteristic annual cycle with a particularly low amplitude from April to May and a high amplitude from September through November (Fig. 3.5). Both years are similar in amplitude and phase of the annual cycle. The annual cycles of the averaged wind stress magnitude, the mixed layer depth and the sub-mixed-layer buoyancy frequency fail to explain this observation. This gives rise to a relation to the spatial structures of the wind stress. However, the exact mechanism could not be identified in the present study.

Spatial Structures The years 1989 and 1996 had particularly strong NAO^+ and NAO^- phases, respectively (Hurrell and Deser, 2009). Accordingly, stronger wind stress amplitudes and subsequently stronger energy fluxes north of 40°N in the winter of 1989 (Fig. 3.4a) are observed. Even though the spatial distributions differ, the zonally averaged energy fluxes south of 40°N are remarkably similar between the two years (Figs. 3.2 and 3.3). Based on the above presented analysis, the agreement between the years in the tropical and subtropical regions is interpreted as an effect of similar structures and magnitudes in the wind stress fields as well as the input parameters.

The ratios of zonally averaged energy fluxes agree well between the two years (Fig. 3.4b). Following the previous arguments the low ratios of energy fluxes in the tropics originate in the steady wind stress structure as well as the shallow mixed layer and smaller horizontal scales. In mid-latitude and subpolar regions the intermittent structure of fast moving atmospheric systems determines the energy transfer. However, mixed layer depth estimates in deep convection areas may cause underestimates of the wind power. Between 20°N and 40°N no relationship between the ratios of energy fluxes and input parameters was observed. Instead, the ratios of energy fluxes are dominated by the spatial structure of the wind stress as described above. This structure appears similar in both years.

3.4.3 Comparison to Previous Studies

Three versions of the slab model have been established since its introduction by Pollard and Millard (1970). The original formulation which serves as mathematical basis of the present study includes the full ocean response to a Reynolds surface stress damped by a linear friction term and rotated by the Coriolis effect. It has been tested successfully with mooring data (Paduan et al., 1989; Pollard, 1980). However, Plueddemann and Farrar (2006) pointed out that the model overestimates the near inertial kinetic energy in the mixed layer due to missing damping at high frequencies. These results were reproduced by Kilbourne and Girton (2015). All versions of the slab model, including the present hybrid model approach, suffer from the same problem since the assessment of a frequency dependent damping was not done in detail. Consequently, the achieved estimates of energy flux ratios may be systematically too low. Alford (2003) attempted to modify the equations from Pollard and Millard (1970) in order to introduce a time dependent friction. However, high frequency damping remained unchanged. D'Asaro (1985) adapted the formulation by Pollard and Millard and suggested to subtract the stationary solution of (Eq. 3.1). Alford (2001) added a spectral solution scheme to the very same formulation. By doing so the wind power is underestimated by $r\rho H_{\mathrm{m}}|\boldsymbol{\xi}|^2/(r^2+f^2)$. This effect does not occur in the present estimate of the energy flux radiated from the mixed layer base and might explain the difference between the here-estimated average energy flux ratio of 9% and the ratio estimated by studies based on D'Asaro (1985) and Alford (2001), that is 12% - 33% estimated by Alford et al. (2012).

Given that the slab model wind power is proportional to the damping parameter r but the kinetic energy density in the mixed layer is not, the energy flux ratio is proportional to the damping time scale r^{-1}. Consequently estimates from different studies utilizing the slab model are difficult to compare when the chosen damping parameters vary considerably across the domain.

Several attempts to quantify ratios of average energy fluxes using general circulation models (Rimac et al., 2013, 2016; Furuichi et al., 2008), large eddy simulations (Skyllingstad et al., 2000) and direct observations (D'Asaro et al., 1995; Alford et al., 2012) have been made. They range from 11.4% (Rimac et al., 2016) to (37±10)% (D'Asaro et al., 1995). The slab model in the here-presented form suffers from a range of systematic errors and approximations. Given the resulting error margins, the here-concluded estimate agrees with, for example, the estimates of Rimac et al. (2016) or the lower bounds estimated by Alford et al. (2012), though the comparison reveals relatively small average energy flux ratios.

It has been shown that the vertical propagation of near-inertial oscillations depends on the horizontal vorticity (Kunze, 1985; Young and Ben Jelloul, 1997; Elipot et al., 2010; Whitt and Thomas, 2015). That means that the eddy field modifies the vertical energy propagation associated with near-inertial oscillations. These effects are not included in the present study and adds a bias compared to measurements and eddy resolving models.

3.5 Summary and Conclusions

A slab model following Pollard and Millard (1970) has been set up. NCEP-CFSR reanalysis fields of wind stress with 0.3° lateral and 1 h temporal resolution and the MIMOC climatology for mixed layer depth were used to force the model. It was then extended by a formulation for the downward energy flux from the mixed layer base inferred from vertical oscillations on the mixed layer base (Olbers et al., 2012). A range of idealized experiments as well as a simulation of the North Atlantic were performed. The area of consideration is affected by meteorological forcing on various time and spatial scales. Different NAO conditions were compared. Buoyancy frequencies at the mixed layer base were estimated using interpolation of the MIMOC absolute salinity and conserved temperature fields. This way it was possible to isolate effects based on differences in both magnitude and structure of the various input parameters

and forcing data.

Northward propagating wind stress pulses with Gaussian shape were used to study inertial pumping caused by a moving wind front. The vertical oscillations are excited due to a phase shift in the local inertial oscillation based on the width of the front and its moving speed. Whereas wind fronts with a typical atmospheric translation speed show transfer ratios about 20%, a wind front with a local duration of approximately half the inertial period leads to maximal energy transfer ratios of more than 60%. Excitation based on the beta effect were observed by imposing a spatially homogeneous wind pulse with a Gaussian profile in time. Vertical motion is induced due to a growing phase shift based on the increase of the local inertial period with latitude. The corresponding energy fluxes are limited by the damping time scale of the slab model and generally lead to small energy transfers of approximately 1.5%. However, the beta effect tends to destroy or prolong the coherence of motion induced by northward and southward moving fronts, respectively. It therefore decreases or increases the energy transfer depending on the moving direction of the front. Gradients in the wind stress field lead to a gradient in the magnitude of the excited inertial oscillation. The magnitude of the corresponding vertical motion and energy transfer crucially depend on the strength of the gradient. This effect is typically small but may lead to values above 10% for gradients on horizontal scales of the order 10 km. It is concluded that the structure of the wind stress (like the translation of atmospheric features such as fronts or hurricanes) play a major role in the excitation of internal gravity waves. But the dynamics are not captured by the slab model itself. Besides the structure of the wind stress field, the ratio of energy fluxes is influenced by resonant forcing effects. Also, it is linearly dependent on the mixed layer depth, the horizontal length scale and the buoyancy frequency N.

Spectral considerations reveal that the amplitude and width of the resonance and therefore the ocean response in the slab model depend on the damping parameter r. However, for physical damping time scales of several days, the resonance peak is very narrow while the flanks are non-zero. Thus, the spectral behavior is determined by the spectral power of the wind stress beyond the resonance frequency $-f$ and resonance plays a role only in the case of narrow wind stress spectra centered at the negative Coriolis frequency. For typically red wind stress spectra (Zhai, 2015) the wind power scales with the damping parameter but the kinetic energy density and thus the energy radiated from the mixed layer base is independent of it. Frequency independent damping

leads to the same ring down time scale across all frequencies. Plueddemann and Farrar (2006) pointed out that, as a consequence, mixed layer velocities may be systematically overestimated.

It is confirmed that the wind power is inversely proportional, and the ratio of energy fluxes is proportional, to the mixed layer depth. However, this dependency is based on the assumption of the equality of the mixed layer depth and the zero-stress level associated with the wind stress. This assumption may fail, e.g. in deep convection areas, and lead to lower estimates of wind power input and accordingly higher estimates of energy flux ratios. Some observations suggest that the maximum depth of wind penetration may be deeper than the mixed layer depth (Dohan and Davis, 2011; Forryan et al., 2015). In this case the wind power may be overestimated instead. Since the energy radiated from the mixed layer base is independent of the mixed layer depth it gives a more robust estimate in that perspective.

The horizontal length scale, L_h, or equivalently the horizontal wave number of the local vertical oscillation, is prescribed by the generation mechanism. For idealized simulations it can be approximated by analytic expressions depending on the investigated scenario. L_h has typical values of $100\,\mathrm{km} - 1000\,\mathrm{km}$ increasing with latitude. In the simulations of the North Atlantic, L_h was parameterized with the aid of boxed Fourier transform analysis. Nevertheless, the length scale is one of the most important sources of uncertainty here.

The energy flux radiated from the mixed layer base linearly depends on the buoyancy frequency N. The stratification is stronger near the equator and decreases with latitude. However, any effects based on this dependency are masked by the increase in horizontal length scale and mixed layer depth and are therefore not observed in the zonal averages.

Simulations of the North Atlantic are structured following the described dependencies on input parameters and structure of the wind field. Ratios of zonally averaged energy fluxes show an increase with latitude similar to the horizontal length scale L_h and the mixed layer depth H_m. This trend is partially compensated by the decrease of stratification with latitude. Moreover, the ratios of zonally averaged energy fluxes indicate several regimes of energy transfer in terms of latitude bands. The tropics (south of 20°N) are determined by rather steady structures with low variability. The excitation of inertial pumping is therefore dominated by the beta effect. Subtropical regions (20°N -

40°N) mark the transition between tropical and mid-latitude climate. Slowly advancing fronts associated with mid-latitude pressure systems and isolated hurricane tracks dominate the energy fluxes. In contrast, the mid-latitude and subpolar energy fluxes are determined by fast moving pressure systems with high variability.

Accordingly, the ratios of zonally averaged energy fluxes have values below 5% in the tropics, plateau at about 12% in the subtropics, with intermediate values around 10% north of 40°N. A peak reaching up to 14% around 58°N may be related to deep convection areas. It remains unclear whether this feature is an artifact related to the mixed layer depth data. The ratios of time-integrated energy fluxes in the whole domain average to 9%. The wind work and the energy radiated themselves are mainly dominated by the magnitude of the wind stress. The wind stress amplitude transfers its seasonal and spatial patterns to both the in- and outgoing energy fluxes. In particular, this can be seen in the zonally averaged energy fluxes from the two years. North of 40°N fluxes are enhanced by around 30% during the positive NAO phase in 1989. In that context, the very good agreement of the ratios of zonally averaged energy fluxes between the two years underlines the importance of the wind field structure. They are independent of the wind stress magnitude.

In summary the major advantage of the hybrid solution is the resolution of generation mechanisms of internal gravity waves with a direct quantification of energy radiated from the mixed layer base into the internal wave field. Errors are introduced by the usage of climatological input, the estimate of a dominant horizontal wavelength, and also by a frequency independent damping. These error sources remain to be improved to make quantitative statements more reliable.

Chapter 4

Response of the Hybrid Model to a Cyclone

In Chapter 2 the non-linear simulation of the ocean response to a storm in an axisymmetric geometry was presented. A major result was that very little energy was found to be transferred to internal gravity waves in the simulation. The parameterization of the vertical momentum flux through the surface in the form of a horizontal stress and the symmetry of the simulation were suggested to be the main reasons for the particularly low values. In this chapter, the analysis is extended by simulating a storm of the same geometry (cf. Section 2.1) in the framework of the hybrid slab model, in which the momentum transfer is implemented in the form of a body force (Chapter 3). Additionally, a laterally moving storm with the same geometry is simulated. The resulting energy fluxes are then compared.

First the setups are described (Section 4.1). Subsequently, a comparison of the hybrid model with the axisymmetric simulations is done (Section 4.2). Lastly, the impact of the lateral movement of the storm on the ocean response is discussed (Section 4.3).

4.1 The Hybrid Model Setup

One of the major differences between the physics of energy transfer in a slab model (cf. Chapter 3) and a full simulation (cf. Chapter 2) with a surface stress implementation is the nature of the forcing. The slab model predicts the average surface velocity resulting from the integrated stress profile. The wind stress is therefore forcing the whole slab simultaneously and has the character of a body force. In contrast, the consideration of a surface stress on a rigid lid only permits a downward propagation of momentum through internal stresses. For illustration, the vertical distribution of the related dissipation was calculated for the model runs presented in Section 2.2 (Fig. 4.1). The core of the

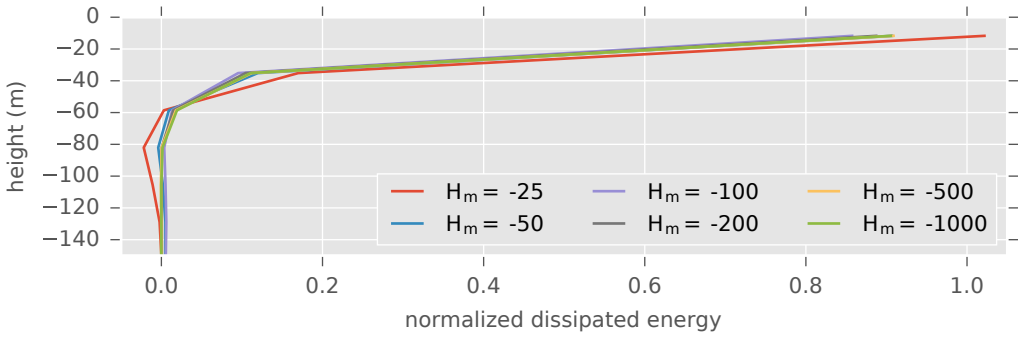

Figure 4.1: Dissipated energy within $R_c = 550\,\mathrm{km}$ as a function of depth for axisymmetric simulations (Chapter 2). The energy balance is estimated for every depth bin separately. Runs with different mixed layer depths H_m are depicted. The profiles are normalized by the total dissipation throughout the water column.

axisymmetric domain was divided into disks with a radius $R_c = 550\,\mathrm{km}$ and a height corresponding to the vertical resolution. For those disks the vertical energy transport at the top and bottom as well as the radial energy fluxes at the outer boundary were estimated. From the resulting energy balance the kinetic energy remaining in each disk was subtracted so that the dissipation is equal to the residual. This analysis revealed that almost all the dissipation takes place within the three topmost bins (Fig. 4.1). Note, that the profiles for several mixed layer depths, H_m, show a negative dissipation at a depth of around 80 m. Additionally, the profile associated to $H_\mathrm{m} = -25\,\mathrm{m}$ shows a dissipation of more than 100% close to the surface. This effect reflects the reduction but also increase of kinetic energy due to the harmonic mixing scheme. For the comparison of the approaches from the two models, a storm analogous to the simulation presented in Chapter 2 is implemented in the hybrid model. Moreover, a storm with the same structure but moving across the domain is considered so that the effect of the movement can be isolated.

The hybrid model is set up with a Cartesian grid with a size of $250 \times 500\,\mathrm{km}$ and a horizontal resolution of 1 km (Table 4.1). The time domain is 25 days with a temporal resolution of 180 s. For comparability the Coriolis frequency $f \equiv 10^{-4}\,\mathrm{rad\,s^{-1}}$ and the buoyancy frequency $N \equiv 10^{-2}\,\mathrm{rad\,s^{-1}}$ are constant throughout the domain. The damping parameter r corresponds to a time scale of 2 days, similar to the damping time scale of the radial velocities in the axisymmetric control run. Note that since the wind power is proportional to the damping parameter r, the shift of the damping time scale to a smaller value leads to larger estimates of the wind power (cf. Section 3.1). This increase is

Table 4.1: Fixed parameters of hybrid slab model setup for storm simulations.

parameter	value		comment
$x_{\max}$	250	km	domain size in x-direction
$y_{\max}$	500	km	domain size in y-direction
$dx = dy$	1	km	horizontal resolution
$t_{\max}$	25	days	model time
dt	180	s	temporal resolution
f	10^{-4}	rad s^{-1}	Coriolis frequency
N	10^{-2}	rad s^{-1}	buoyancy frequency
r	0.5	$days^{-1}$	damping parameter
ρ_0	1027	kg m^{-3}	density of sea water

related to a shift of the near-inertial response towards smaller frequencies in a red wind stress spectrum. The corresponding energy flux associated to the generation of internal gravity waves responds only to frequencies larger than the Coriolis frequency f and therefore does not experience an increase. This leads to reduced energy flux ratios compared to the simulations of the North Atlantic in Chapter 3 with a characteristic damping time scale equal to 5 days.

4.1.1 The Stationary, Axisymmetric Storm

Corresponding to the simulation described in Chapter 2 a stationary, axisymmetric storm with the same radial structure is set up. In particular, the wind has a Rankine vortex profile with radius $R_r = 50\,\text{km}$ and thus a constant vorticity for radii smaller than R_r and zero vorticity beyond. The wind stress is computed with the bulk parameterization introduced in Section 2.1 (Eq. 2.10). The storm is located at the center of the domain and has a pulse-like amplitude. Within 12 hours it increases linearly to its maximum, stays constant for 24 hours and then decreases linearly to zero within another 12 hours. The maximum wind speed at 10 m is $|\boldsymbol{u}|_{10} = 30\,\text{m s}^{-1}$. The horizontal length scale is set by the diameter of the Rankine vortex, that is $L_\text{h} = 100\,\text{km}$.

This setting is equivalent to the control experiment described in Chapter 2. However, a comparison must consider the particular differences of the simulations. Whereas Chapter 2 describes a non-linear model of the ocean with full depth and a non-constant stratification, the hybrid model is based on a linearized equation for a homogeneous surface slab. Any sink of energy is parameterized with a Rayleigh friction term. Due to these simplifications the hybrid slab model is independent of the symmetry of the forcing but may be

calculated on a regular x-y-grid here. Moreover, the slab model does not permit the propagation of internal gravity waves and therefore does not reproduce them. The corresponding local energy flux is derived from the vertical oscillations of the mixed layer base due to the divergence of the near-inertial surface response.

4.1.2 The Moving Cyclone

In addition to the setup described above, a cyclone with the same structure but moving across the domain with a speed of $v_{atm} = 5.79\,\mathrm{m\,s^{-1}}$ or equivalently $v_{atm} = 500\,\mathrm{km\,day^{-1}}$ is simulated. It starts 500 km south of the domain and moves north so that the critical radius from the center of the vortex enters the domain after 0.9 days. The strength of the cyclone is constant and corresponds to a maximum wind speed at ten meters height of $|\boldsymbol{u}|_{10} = 30\,\mathrm{m\,s^{-1}}$. In contrast to the stationary setup, the horizontal wavelength is set by the movement speed of the cyclone. Two adjacent points in the grid along the storm track, that is in the northward direction, experience exactly the same forcing but with a time lag Δt. This time lag is related to the translation speed of the storm by $\Delta t = \Delta y / v_{atm}$. Considering now the inertial period $\Delta t = 2\pi/f$ with a constant Coriolis frequency, the along track wavelength can be estimated by $L_y = 2\pi v_{atm}/f = 363.61\,\mathrm{km}$. This wavelength is equivalent to the moving speed of the storm multiplied with the inertial period and is characteristic to the wake of the storm.

4.2 Comparison of the two Models

Considering the north-south transect through the center of the storm in the hybrid model allows for the identification of azimuthal and radial component with respect to the center of the storm. These velocity components can then be compared to the azimuthal and radial velocity from the axisymmetric simulation, integrated over the mixed layer (Fig. 4.2). Recall that the classical slab model and hybrid slab model rely on a linearized set of equations in order to isolate the near-inertial response of the ocean (Eq. 3.1). Consequently, wind induced advection is neglected. Therefore, the azimuthal velocity computed with the slab model does not show the formation of a vortex underneath the storm. Instead, the momentum is transferred to the inertial motion only. The result is a purely oscillatory azimuthal response. In contrast, the azimuthal velocity from the axisymmetric simulation is dominated by the described vortex formation (Fig. 4.2c and d as well as Fig. 4.3b). Note that the azimuthal am-

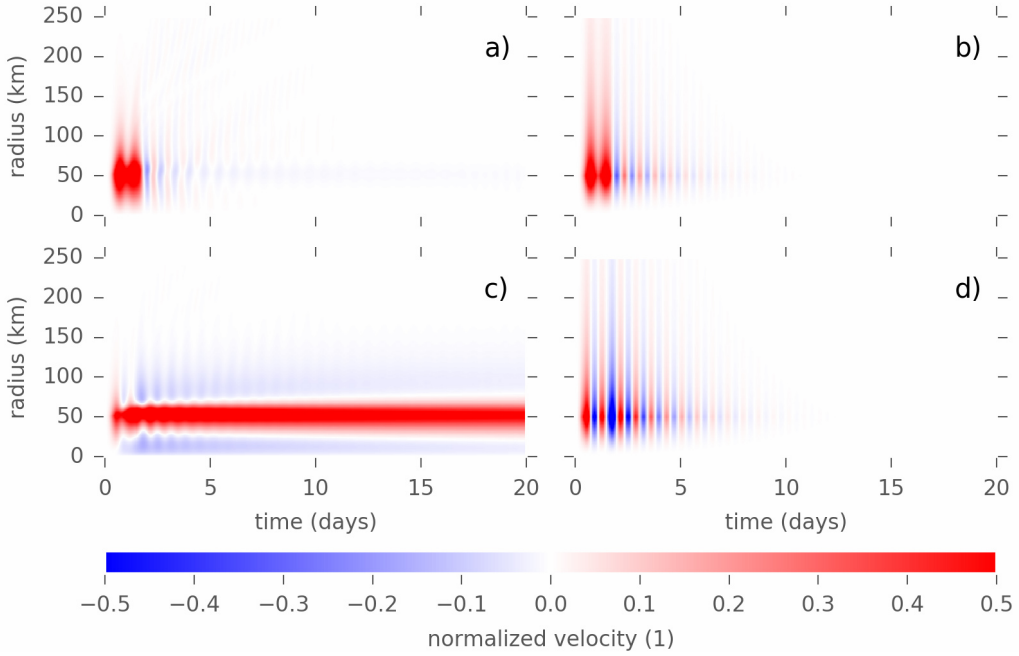

Figure 4.2: Azimuthal velocities from the axisymmetric (a) and hybrid slab model (b) simulations as well as radial velocities from the axisymmetric (c) and hybrid slab model (d) simulations. The velocities are normalized with their maximum value. To increase visibility of the structure in the decay phase, the colormap is limited to ± 0.5.

plitude is about two times larger in the hybrid slab model. However, this factor is masked by the velocities associated to the non-linear effects in the axisymmetric model and does not represent the difference of the inertial amplitudes. Band-pass-filtering the mixed layer azimuthal velocity from the axisymmetric simulation suggests that the azimuthal near-inertial response is smaller than half the hybrid slab model estimate (Fig. 4.3b).

As the radial velocity is not directly accelerated by the wind drag in the axisymmetric simulation it corresponds to the near-inertial response and therefore has a very similar structure compared to the hybrid slab model (Fig. 4.2a and b as well as Fig. 4.3a). During the forcing the response is dominated by the deflected acceleration due to the wind stress. The subsequent inertial oscillation then decays with a characteristic damping time scale. The amplitude of the radial velocity in the hybrid slab model is more than 6 times larger compared to the axisymmetric model. The vertical velocities have the same structure as the radial response described above (Fig. 4.3c). Similar to the other radial component, the vertical velocity estimated with the hybrid slab model is about 8 times larger. The analogy between the radial and vertical velocities in both

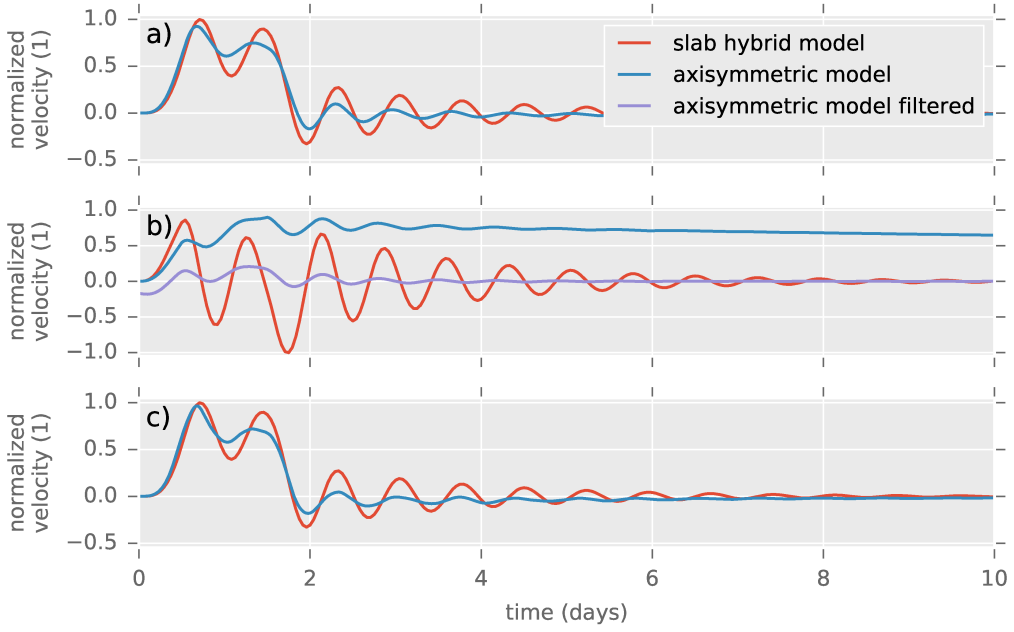

Figure 4.3: Normalized radial (a), azimuthal (b) and vertical velocity (c) from the hybrid slab model and the non-linear axisymmetric model at the radius $R_r = 50\,\mathrm{km}$. For comparison the azimuthal velocity is bandpass filtered around the Coriolis frequency with a Kaiser-Bessel window.

models is consistent with the estimate of the terminal velocity structure in the axisymmetric simulation with zero vertical and radial velocities (cf. Section 2.1). These two components are associated with the near-inertial response and decay in time due to dissipation and radiation of internal gravity waves.

The wind work for the two simulations is calculated following Eqs. (3.5) and (2.25). The hybrid slab model estimates a wind work of approximately $\Phi_{\mathrm{wind}}^{(\mathrm{hybrid})} \approx 355.1\,\mathrm{TJ}$ compared to the axisymmetric simulation with $\Phi_{\mathrm{wind}}^{(\mathrm{axisymm})} \approx 401.41\,\mathrm{TJ}$ (Table 4.2). Surprisingly, the result from the axisymmetric simulation is larger even though the azimuthal mixed layer velocity was observed to be smaller. There are two reasons for this scaling. First, the average mixed layer velocity was compared. In the axisymmetric simulation the horizontal velocities show a strong gradient within the water column and the wind power is estimated using the surface values. They are about 50 % larger than the average of the uppermost 50 m. Second, the azimuthal velocity estimated with the slab model does not form a vortex in the direction of the wind drag. Its oscillatory structure leads to subsequent phases of acceleration and deceleration of the azimuthal mixed layer velocity. The latter is characterized by a negative wind power and hence has a negative contribution to the wind work.

Table 4.2: Wind work and energy radiated as internal gravity waves as well as their ratio for all compared simulations.

	Φ_{wind} (TJ)	Φ_{IW} (TJ)	$\Phi_{\text{IW}}/\Phi_{\text{wind}}$
axisymmetric model	401.41	0.061	$1.52 \cdot 10^{-4}$
hybrid model (stationary)	355.1	3.91	$1.1 \cdot 10^{-2}$
hybrid model (moving cyclone)	2200.7	672.7	$30.6 \cdot 10^{-2}$

The hybrid slab model estimate of the energy transferred into the internal gravity wave field is approximately $\Phi_{\text{IW}}^{(\text{hybrid})} \approx 3.91\,\text{TJ}$. Compared to the axisymmetric simulation, with $\Phi_{\text{IW}}^{(\text{axisymm})} \approx 0.061\,\text{TJ}$, this is two orders of magnitudes larger (Table 4.2). In particular, this corresponds to a factor of about 64, the square of the difference in magnitude of the vertical velocities. This is consistent with the dependency of the energy flux on the square of the vertical velocity (Eq. 3.16). Hence, a larger near inertial amplitude in the hybrid slab model results in a correspondingly larger internal wave energy flux. However, the two models represent two competing views on the radiation of the internal gravity waves. The hybrid model does not directly produce the waves and it estimates the associated vertical energy flux through the structure of the inertial pumping. This energy is assumed to be locally radiated downward in the water column. In contrast, the axisymmetric internal gravity waves observed in the non-linear simulation have low mode structure and a radially outward group velocity. They move as cylindrical wave packets away from the center of the storm. The angle of propagation of internal gravity waves with a frequency close to the inertial frequency is close to horizontal so that the picture of the radially outward moving wave packet appears more complete.

The velocities and energy fluxes in the far field of the axisymmetric model are dominated by radiating internal gravity waves in the stratified layer and their surface manifestation in the mixed layer. This effect is not covered by the physics of the hybrid slab model.

4.3 The Influence of the Lateral Movement of the Storm

The structure of the ocean response to a stationary and a laterally moving storm are different in many aspects. A stationary storm creates a characteristic response with the shape of a ring with the radius of the Rankine vortex at $R_r = 50\,\mathrm{km}$. The horizontal velocities are structured so that they oscillate in normal direction to the circle and therefore lead to inertial pumping inside and outside the circle but with opposite sign (Fig. 4.4a - c). The vertical velocity amplitude A_w is largest close to the radius, R_r. It decreases to zero towards the center of the circle. Beyond this radius, the amplitude is generally smaller and decays strongly with distance from the center. In contrast to the symmetric case, the moving storm leaves an asymmetric wake. Both the northward and the eastward velocity components are intensified at the right side of the storm (Fig. 4.4a and b). This asymmetry originates in the local sense of rotation of the wind stress during the passage of the storm. To the left of the storm track it rotates in the counter clockwise direction whereas it rotates clockwise on the right. Note that this is equivalent to a positive and a negative sign of the wind stress curl, respectively. Hence, to the left side of the track the rotation of the wind stress vector is opposed to the inertial rotation and therefore counteracts the induced velocities. Even though the horizontal velocities are strongly asymmetric, their divergence and hence the vertical velocity is symmetric with respect to the cross-track component (Fig. 4.4c). It has zero amplitude at a cross-track distance of the radius, R_r and a periodic structure in the along-track direction. It therefore forms rectangular billows of upward and downward velocity following the storm. Similar to the stationary case, the vertical velocity decays for cross-track distances larger than the radius of the vortex, R_r. The along-track wavelength is set by the movement speed of the storm and equal to $L_{\mathrm{y}} = 363.61\,\mathrm{km}$ (cf. Section 4.1). The cross-track length scale is set by the width structure of the storm so that $L_{\mathrm{x}} \sim 100\,\mathrm{km}$. The former is assumed to be the dominant wavelength and therefore used to estimate the energy fluxes.

Whereas the wind power is proportional to the horizontal velocity, the internal wave energy flux scales with the square of the vertical velocity. Hence, the wind power is large where the wind stress and the horizontal velocities are strong and the energy flux into the internal gravity wave field is large where the divergence of the horizontal velocity has large amplitudes. The energy fluxes

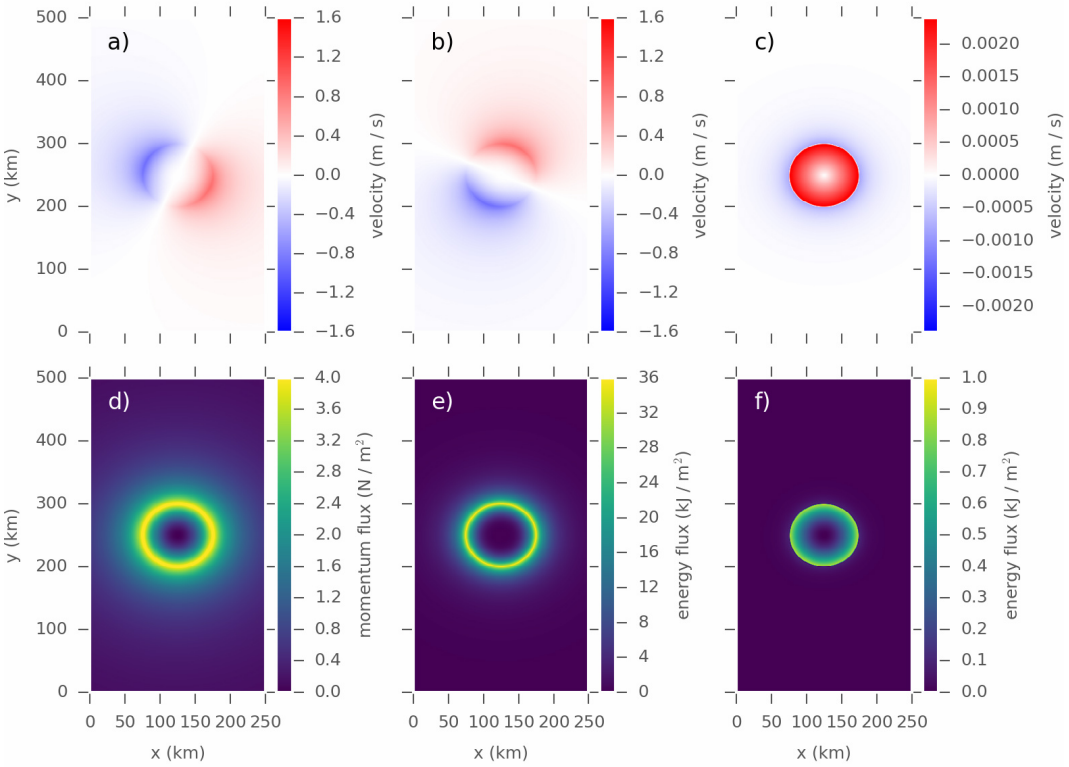

Figure 4.4: Eastward (a), northward (b) and vertical velocity (c) as well as wind stress (d) at time $t = 43.2\,\mathrm{h}$ for a stationary storm, simulated with the hybrid slab model. The wind work (e) and energy flux into the internal gravity wave field (f) represent integrals in time.

in both simulations are distributed correspondingly (Figs. 4.4e - f and 4.5e - f). In the stationary case the wind power is characterized by the ring structure of the Rankine vortex. Energy is transferred close to the radius of the vortex R_r. In comparison, the corresponding energy flux into the internal gravity wave field is dominated by radii close to but smaller than R_r. Compared to the stationary storm, the lateral shift in energy fluxes is more dominant for a moving storm. As described above, it leaves a wake with an asymmetry towards the right side of the storm track. The wind power has therefore the same shift and is dominated by the energy flux on the right side of the track. In contrast, the energy flux into the internal gravity wave field follows the symmetry of the vertical velocities. It is therefore largest at a cross-track distance close to the vortex radius - both on the left and the right side. Consequently, the ratio of energy transferred by the wind to the energy radiated away is larger on the right side of the storm track. That means that the energy transfer to the internal gravity wave field is more efficient on the left side of the storm track. Also, on the right side the energy available for turbulent motion, i.e. stirring

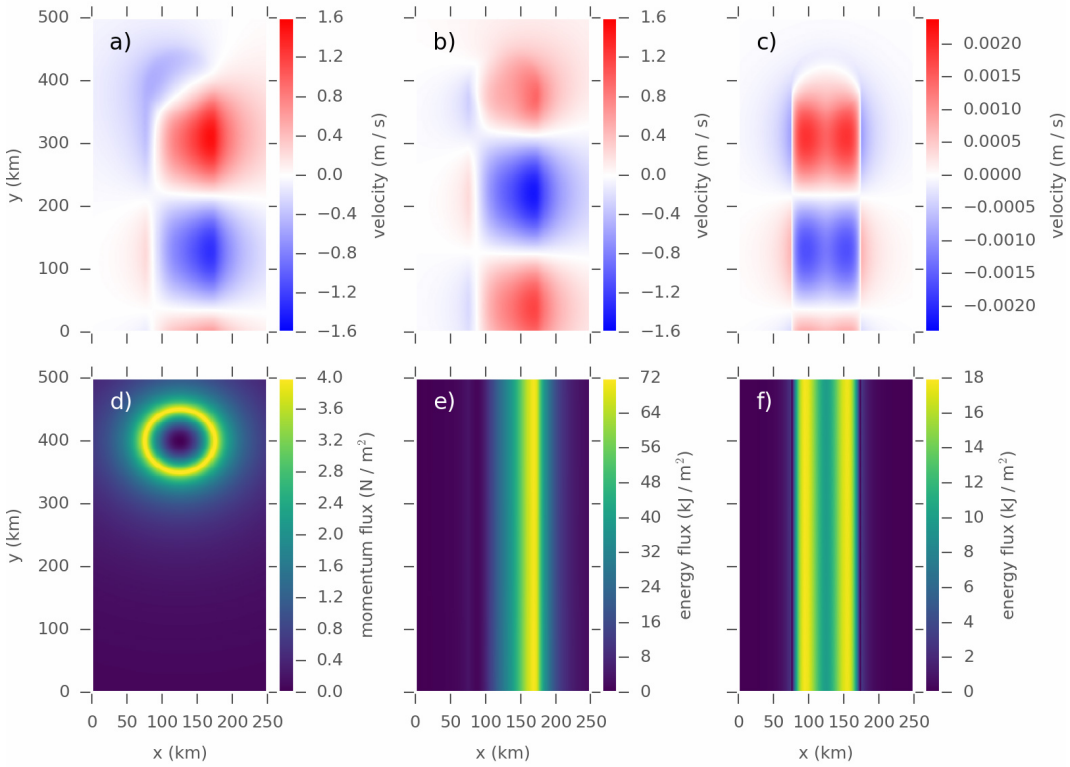

Figure 4.5: Eastward (a), northward (b) and vertical velocity (c) as well as wind stress (d) at time $t = 30.4\,\mathrm{h}$ for a laterally moving storm, simulated with the hybrid slab model. The wind work (e) and energy flux into the internal gravity wave field (f) represent integrals in time.

or deepening the mixed layer, is significantly larger. This asymmetry is consistent with observations and previous simulations (Price, 1981, 1983; Price et al., 1978; Shay et al., 1992) but may be modulated by the β-effect when considering storms moving in a β-plane (Gill, 1984; Niwa and Hibiya, 1997). Also, intensified shear at the mixed layer base and mixed layer entrainment shifted to the right side of the storm track have been observed and reproduced in simulations (Shay et al., 1992; Sanford et al., 2011). However, rapid mixed layer entrainment is not included in the slab model dynamics. The assumption that $\partial/\partial t(H_\mathrm{m}\boldsymbol{u}) \approx H_\mathrm{m}\partial/\partial t\boldsymbol{u}$ (cf. Section 3.1) leads to an over-estimate of the acceleration and thus the near-inertial currents. Consequently, the wind power is potentially overestimated. Since this effect may be frequency dependent it is not clear how it influences the energy transferred to internal gravity waves and subsequently the energy flux ratio.

In the stationary case, the wind work and the energy transferred to the internal gravity waves field are 355.1 TJ and 3.91 TJ, respectively. This gives a ratio

of approximately 1 %. The wind work corresponding to the moving storm is about 2200.7 TJ. The energy radiated is approximately 672.7 TJ. Thus, the ratio of energies is 31 % and the fraction of the inferred energy resulting in the generation of internal gravity waves is increased by a factor 30 due to the movement of the storm (Table 4.2). The phase shift of the horizontal velocities in the wake of the moving cyclone induces vertical velocities with amplitude similar to the inertial pumping induced by a stationary storm. However, the phase shift is based only on the movement of the storm so that the whole area in the wake of the storm is affected and the vertical oscillations are not as confined as in the stationary case. This results in a broader area of excitation of internal gravity waves (Fig. 4.5f). Moreover, a horizontal wavelength larger than the length scale of the storm itself induces a stronger energy flux into the internal gravity wave field due to a bigger vertical group velocity. This is true for any storm moving faster than $v_{atm} = 1.59\,\mathrm{m\,s^{-1}}$ and independent of the storm size. This threshold of the translation speed of the storm corresponds to approximately $5.7\,\mathrm{km\,h^{-1}}$ and is fairly slow compared to observations (Price et al., 1991).

In general, the energy transfer might be non-local on a scale of 100 km. However, the hybrid extension describes the local vertical energy flux of an internal wave with a prescribed vertical amplitude, wave number and frequency spectrum. Thus, a non-local energy transfer process is excluded *a priori* in the hybrid slab model formulation. Note, that the absolute values of the energy transfers can not be compared between the cases because the residence time of the moving storm inside the domain is longer than the duration of the pulse.

4.4 Conclusions

The comparison between the hybrid slab model and the non-linear, axisymmetric Boussinesq simulation visualized major differences between the two approaches.

The linearized slab equation (Eq. 3.3) does not allow for the formation of a vortex underneath the storm. Consequently, the estimate of the wind power does not include the wind driven advection and is therefore generally underestimated. That also means that all energy flux ratios concluded from the classical and the hybrid slab model are systematically too large. In contrast, a frequency independent damping may lead to a systematic overestimate of

the wind power (Plueddemann and Farrar, 2006). The implementation of the forcing as a body force and the transfer of all the momentum from the wind to near-inertial motions lead to a six to eight times larger near-inertial response. Nevertheless, the structure of the near-inertial oscillations is very similar with both approaches. The wind work estimated with the two models have similar magnitudes. However, the increased horizontal velocities lead to an increased vertical velocity and an estimate of the energy transferred to internal gravity waves is about 64 times larger compared to the axisymmetric simulation. The reason for the large factor is the square dependency of the energy flux on the vertical velocity.

The most important difference to a stationary cyclone is the asymmetry of the ocean response to the moving storm. In the stationary case, both the wind power and the energy flux into the internal gravity wave field are confined to a small circular area close to the critical radius of the forcing profile. The corresponding energy flux ratio is about 1 %. In contrast, the moving storm leaves an asymmetric wake with horizontal velocities having largest amplitudes to the right of the storm track. This is related to the sign of the wind stress curl and leads to a reduction of wind power on the left side of the storm track. However, the vertical velocity remains symmetric with respect to the track. As a consequence there is a lateral shift between the maxima of the wind power and the energy flux induced by radiated internal gravity waves. Note that there is no non-local energy transfer process possible in the used model formulation. For a movement speed of the storm larger than $1.59\,\mathrm{m\,s^{-1}}$ the wake is characterized by a wavelength larger than 100 km. The latter corresponds to the length scale set by the storm structure. Hence a moving storm with a speed above the named threshold leads to a wake with increased horizontal length scales and therefore enhanced energy flux leaving the mixed layer. All three effects - the reduction of wind power at the left side of the track, the nonetheless symmetric vertical velocity response and the increased horizontal length scale in the wake lead to an increased energy flux ratio by a factor 30. Thus, the movement of the storm appears vital to the generation of internal gravity waves.

Chapter 5

Outlook: 10 Years of Global Internal Wave Climate

The analysis of the hybrid slab model presented here showed that it is a suitable tool to study the excitation of internal gravity waves by inertial pumping (Chapter 3). It is capable of reproducing the oceans' response to mesoscale atmospheric features (Chapter 4) and sub mixed layer internal wave spectra (Jurgenowski et al., 2017). Moreover, the estimated energy fluxes agree with previous studies (Chapter 3). In contrast to global circulation models, it is a cost-efficient simulation of the energy radiated as IGWs from the surface mixed layer. Thus, the global implementation of the hybrid slab model has many potential applications. Some suggestions are a robust estimate for the energy imparted into the global internal gravity waves field or the statistical analysis of long time series. Regional and global climate phenomena like the North Atlantic Oscillation and the El Niño Southern Oscillation may be studied. However, a robust estimate of the characteristic damping time scale r^{-1} as well as the horizontal wave length L_h is needed.

Here, a preview of 10 years of global simulation with a constant horizontal wavelength is presented (Section 5.2). The damping time scales used for these simulations are inferred from satellite tracked surface drifters (Section 5.1; Park et al., 2009) and thus originate in direct measurements of inertial oscillations. A suggestion for improving the estimate of the horizontal wavelength L_h is made (Section 5.3).

5.1 Input Data and Model Setup

The formulation and assumptions of the hybrid slab model used for the present global setup was introduced in Chapter 3 and Appendix B.1. Here, it is recalled that the hybrid slab model needs the surface wind stress, $\boldsymbol{\tau}_0$, the local mixed layer depth, H_m, and the local buoyancy frequency at the mixed layer depth, N, as input parameters (Eqs. 3.3 and 3.3). Moreover, the dominant horizontal wave number, k_h, or equivalently the horizontal wavelength, L_h, of the vertical velocity field is needed (Eq. 3.16).

Wind stress data from the NCEP-CFSR global reanalysis from year 1989 to 1998 are used (Saha et al., 2010). The horizontal resolution of 0.312° corresponds to roughly 35 km close to the equator and about 15 km at a latitude of 65°N so that dominant horizontal wavelengths of the order 100 km are well resolved. The domain between 5°S and 5°N is omitted to satisfy the assumption of a small damping parameter with respect to the Coriolis frequency $r \ll f$. The hourly temporal resolution ensures the coverage of the inertial frequency up to high latitudes.

The mixed layer depth is obtained from the MIMOC climatology with 0.5° horizontal resolution (Schmidtko et al., 2013) and interpolated horizontally using a bilinear method. As in the test runs, the climatological values are set to mid-month time and linearly interpolated to match the wind stress time series (cf. Chapter 3). Accordingly, the buoyancy frequency is calculated from the conservative temperature and absolute salinity profiles provided with the MIMOC climatology where the density is obtained using finite differences and the Thermodynamic Equation of Seawater 2010 (McDougall and Barker, 2011). The profiles are linearly interpolated to the mixed layer depth and bilinearly interpolated in the horizontal to match the wind stress resolution.

The damping parameter is based on a global estimate from drifter track observations (Park et al., 2009). Since the values for the South Atlantic and Indian Ocean, the North and South Pacific are very similar they are averaged to avoid transition signals at the boundaries between the ocean basins (Fig. 5.1a). The North Atlantic has a very distinct characteristic damping time scale that is almost constant with a value close to 5 days. Therefore it is not averaged with the other basins. Instead, the North Atlantic is treated as isolated (Fig. 5.1b). Due to its location with respect to the model bounds there are no open ocean boundaries to other basins and artificial transition signals do not occur.

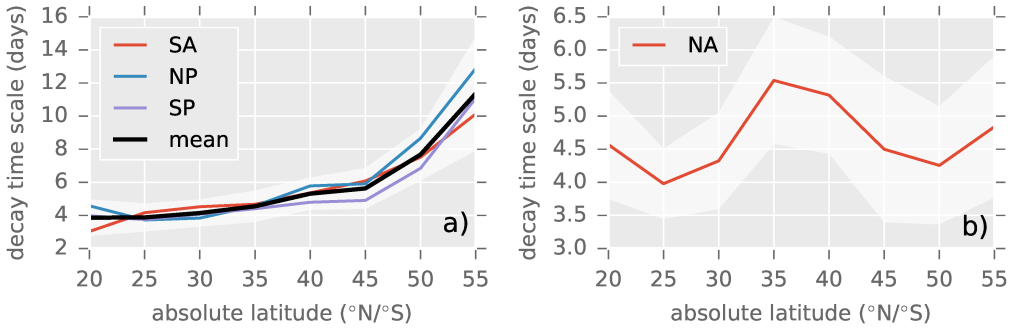

Figure 5.1: Damping time scales estimated from drifter trajectories in Park et al. (2009). (a) damping time scales for South Atlantic and Indian Ocean (SA), North Pacific (NP), South Pacific (SP) and mean. (b) damping time scales for North Atlantic (NA). The shaded areas depict the 95% confidence interval of the mean (a) and the error estimate for the North Atlantic (b).

The horizontal wavelength, L_h, is generally unknown and has to be extracted from the vertical velocity field. In this preliminary simulation the wavelength is set to $L_h = 400\,\mathrm{km}$ (cf. Section 5.2). This value is generally too small in mid-latitudes (Fig. B.2) and may lead to an over-estimate of the energy radiated in low latitudes and a corresponding underestimate in mid-latitudes. Since the storms of the mid-latitudes have a dominant role in the energy transfers, the radiated energy is most likely underestimated. In future setups the horizontal wave length may be deduced from the vertical velocities using a spatial autocorrelation method (Section 5.3).

5.2 10 Years of Global Simulation

Using the above-described input parameters and data, the global near-inertial response from 1989 through 1998 are simulated. The seasonally averaged wind power shows large areas of strong energy transfer in mid-latitudes in the North Atlantic and the North Pacific during the first and last quarter of the year (Fig. 5.2). This corresponds to the autumn and winter storm season on the northern hemisphere. Likewise, the mid-latitudes on the southern hemisphere show a broad band of enhanced wind power but with a weaker seasonal cycle and smaller magnitude compared to the north. Tracks from individual strong tropical storms are visible in the long time seasonal averages. Hence, they may play an important role in the energy supplied to the ocean surface in general. The average global wind power is approximately 0.5 TW. This is in agreement

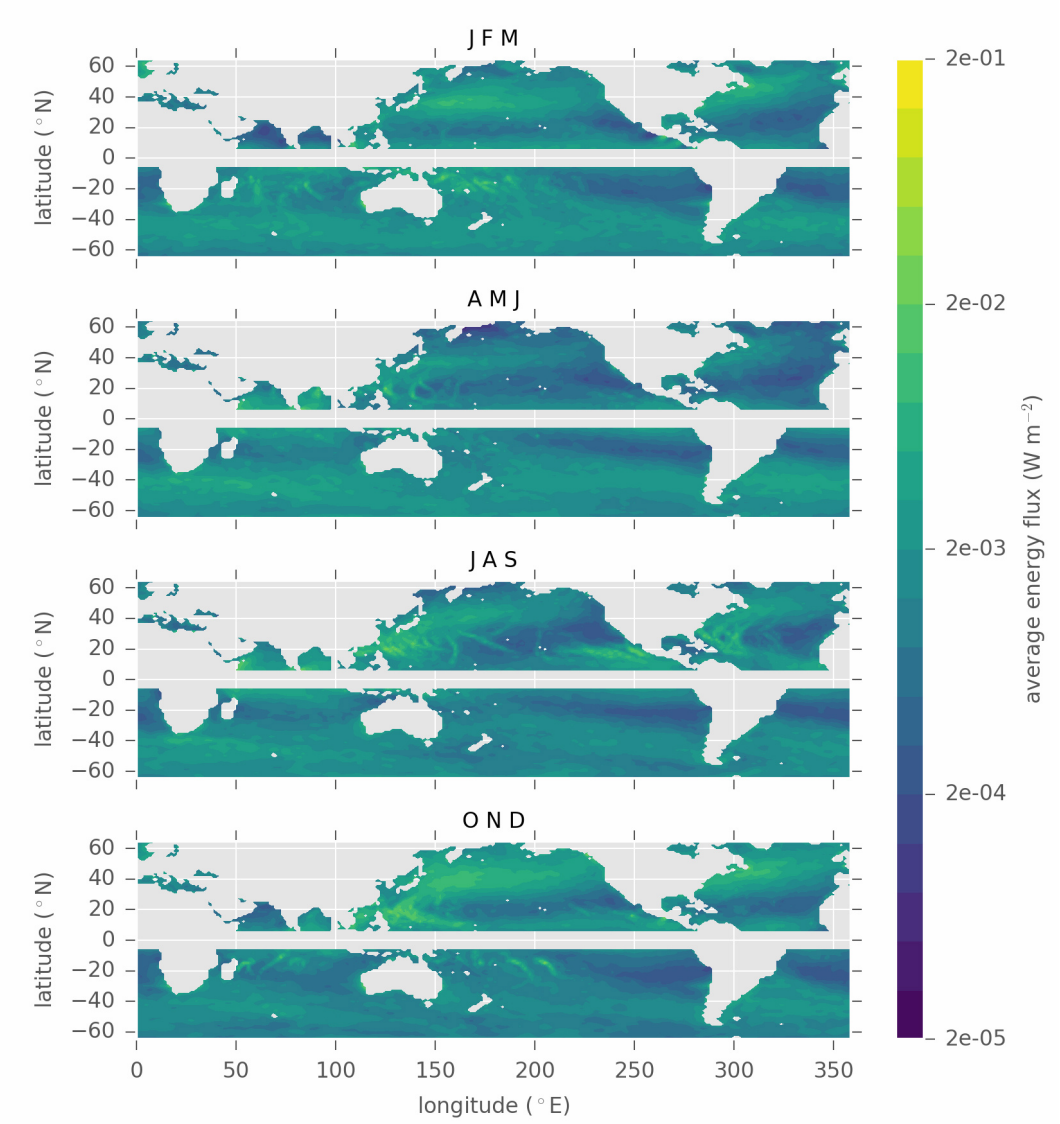

Figure 5.2: Seasonally averaged global wind power from 1989 to 1998. Latitudes between 5°S and 5°N are omitted to satisfy the assumptions of a small damping parameter with respect to the Coriolis frequency $r \ll f$.

with previous estimates (Alford, 2001; Watanabe and Hibiya, 2002; Alford, 2003; Rimac et al., 2013).

The seasonally averaged energy flux into the internal gravity wave field has a similar structure to the wind power (Fig. 5.3). Broad mid-latitude storm regions and strong tropical storms dominate the energy transfer. In comparison to the wind work, structures like the storm tracks tend to be more confined. Moreover, the amplitude is two orders of magnitude smaller, the total energy radiated from the mixed layer is about 7 GJ. Thus, the ratio of global wind

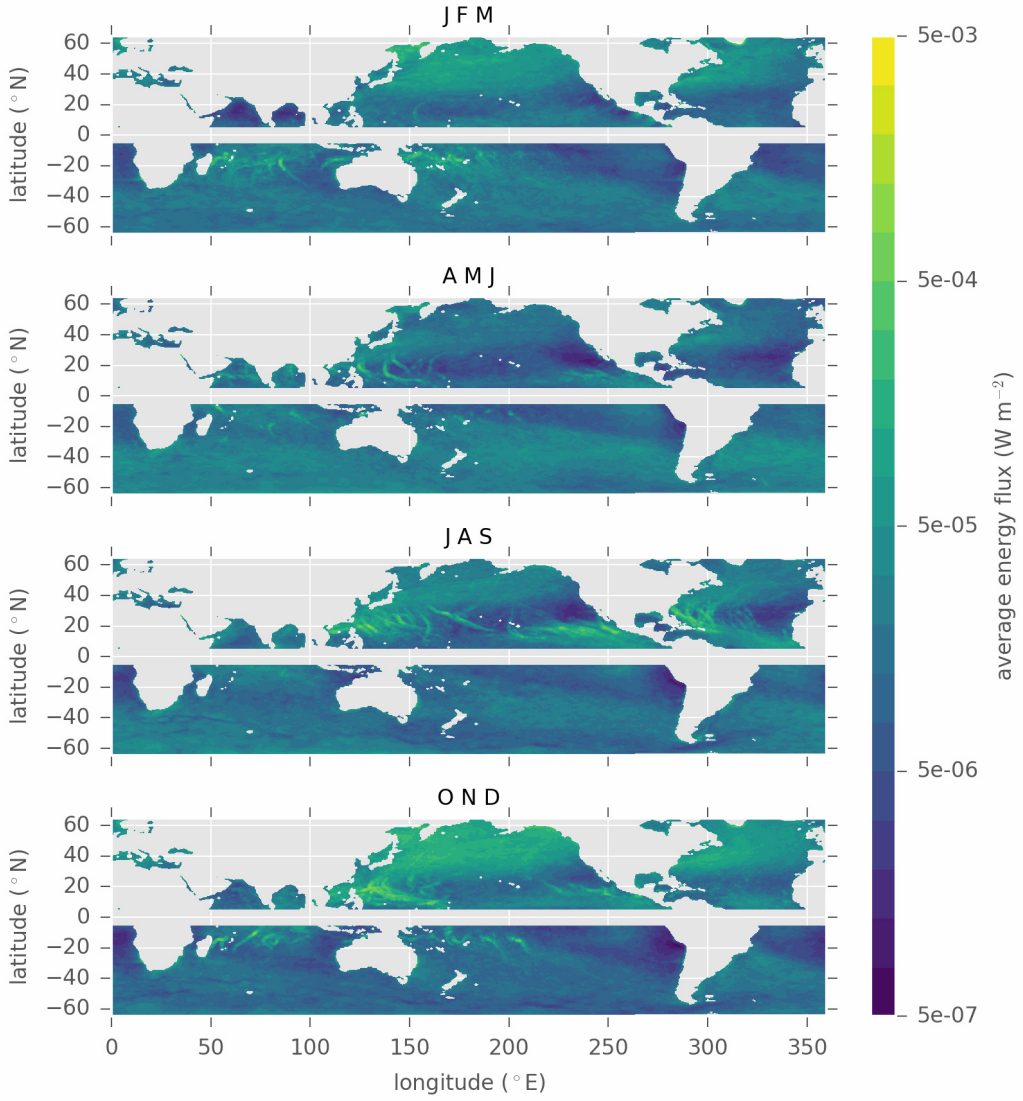

Figure 5.3: Seasonally averaged global energy flux transferred to the internal gravity wave field from 1989 to 1998. Latitudes between 5°S and 5°N are omitted to satisfy the assumptions of a small damping parameter with respect to the Coriolis frequency $r \ll f$.

work to the global energy radiated is equal to approximately 1.3 %, which is one order of magnitude lower than observed in the ocean and general ocean circulation models (e.g. Price, 1983; D'Asaro et al., 1995; Alford et al., 2012; Rimac et al., 2016). Also the ratio estimated with the hybrid slab model for the North Atlantic, 9 %, suggests higher results (Chapter 3). This difference may be associated to the constant wavelength used here.

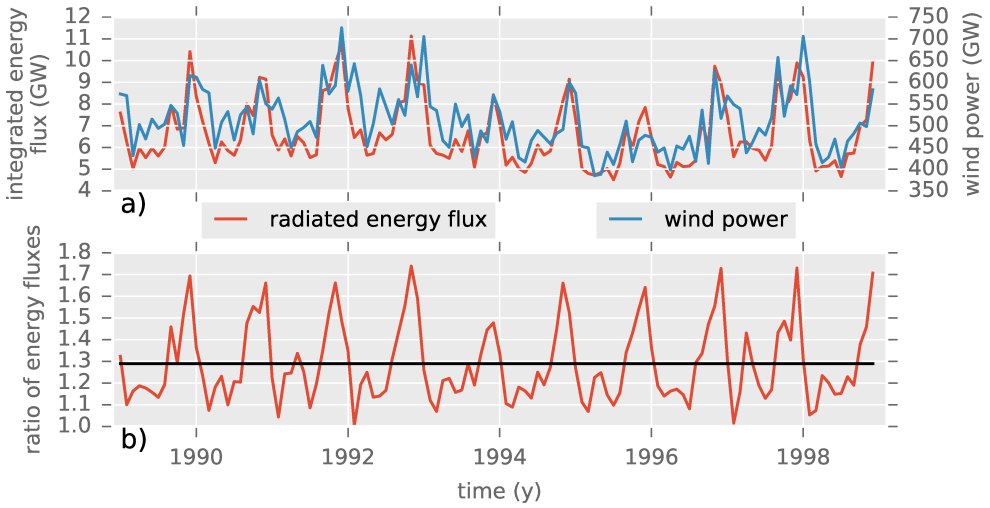

Figure 5.4: (a) Monthly averaged global energy flux transferred from the surface slab layer to internal gravity waves (left) and monthly averaged wind power (right). (b) Ratios of the monthly global energy transferred from the surface slab layer to internal gravity waves and the monthly global wind work. The black line marks the mean value.

Apart from the spatial distribution of the average energy fluxes, their temporal evolution may be another subject of investigation. For example, the ratio of the monthly integrated global energy fluxes shows a clear annual cycle with minima in early months and maxima in late months of the year (Fig. 5.4b). This suggests a dominant role of the storm season on the northern hemisphere. Even though the annual cycle has a similar shape, the year-to-year variation of the ratios does not follow the same trends as the monthly averaged wind power or the energy radiated as internal gravity waves (Fig. 5.4).

The visualizations of a first 10 years data set suggest a range of new research questions that may be studied with the hybrid slab model. *What are the dominant regions of energy flux from the mixed layer to the internal gravity waves? Do they differ from the regions characterized by large wind power? What determines the ratio of the global energy radiated from the mixed layer relative to the wind work? How does it vary on a long time scale?*

5.3 A New Approach to the Horizontal Length Scale

The energy flux from the mixed layer into the stratified layer below depends on the horizontal wave number k_h (Eq. 3.16). This wave number is associated to the horizontal structure of the vertical velocity. There have been several attempts to quantify L_h with different methods. Rimac et al. (2013) and Simmons and Alford (2012) estimated the wavelength in general circulation models resulting in a typical range between 200 km and 600 km. Park et al. (2009) estimated the horizontal length scale from the spatial autocorrelation of the wind velocity at 10 m height. They assume Gaussian-like spatial wind structures and determine the length scales of the wind by fitting a Gaussian to the correlation function depending on the distance to the point considered. This is an effective measure of the size of the wind structures under the application of the central-limit theorem for distributions. Their approach leads to values between 50 km and 400 km. However, the observation of coherent wave-like structures in the vertical velocity (cf. Chapter 3) suggests to measure the wavelength of these structures rather than their associated effective size. Hence, a spatial correlation coefficient following the scheme of Moran (1950) may be used to find the scale of recurrent structures in the vertical velocity. In particular, the autocorrelation coefficient I of a subset $\mathsf{B} \subset \mathsf{A}$ for a variable $y(\boldsymbol{x})$ with the deviation from the mean value $z_i = y_i - \bar{y}$ is given by

$$I = \frac{n_\mathrm{A}}{n_\mathrm{B}} \frac{\sum\limits_{\mathsf{B}} z_i z_j}{\sum\limits_{\mathsf{A}} z_i^2}. \tag{5.1}$$

Here, n_A and n_B are the number of points in the respective set of values. No weight function is applied. If the set B is defined so that all pairs of points in B have a distance within the interval $[r_k, r_{k+1})$ the coefficient I becomes a measure of autocorrelation of the variable y in a set A as a function of the distance. Equivalently, B can be defined as the set of points having a distance from a given point within the interval $[r_k, r_{k+1})$. This formulation with respect to the vertical velocity determined from the divergent near-inertial response of the surface slab may be used. The distance associated with the maximum of the autocorrelation is then a measure of the length scale of wave-like structures in the vertical velocity. It is equivalent to the wavelength of the structure around the given point. However, care must be taken since the autocorrelation with respect to a point on a local extremum may result in a maximal correlation close to the point itself. Thus, it may be of use to define a minimum distance to avoid the signal associated to the size of the structure around the given

point. Also, the formulation requires a constraint for choosing a distance in case of equally correlated rings around the point. It is worth mentioning, that a normally distributed random process would lead to an autocorrelation coefficient with a Gaussian shape and a maximum at zero. This is equivalent to the assumptions made by Park et al. (2009).

In summary, the procedure proposed tests all points in rings with defined radii around a given point for the autocorrelation with the central point. Where a wave like structure exists this leads to the corresponding wavelength.

5.4 Conclusions

A first set of 10 years simulation with a constant horizontal wavelength, $L_\mathrm{h} = 400\,\mathrm{km}$, was presented. Estimates of the global average wind work, 0.5 TW, and the spatial distribution of the average seasonal wind power agree well with previous studies (Alford, 2001; Watanabe and Hibiya, 2002; Alford, 2003; Rimac et al., 2013). However, the simulated average global energy flux radiated as internal gravity waves, 7 GJ, is one order of magnitude smaller than previously estimated (e.g. Price, 1983; D'Asaro et al., 1995; Alford et al., 2012; Rimac et al., 2016). This discrepancy may be related to the constant horizontal wavelength used and the subsequent underestimate of the mid-latitude energy fluxes. Thus, a robust method for determining the horizontal wavelength, L_h, is needed. A potential solution, the use of spatial autocorrelations, is suggested.

From these first global results of the hybrid slab model, a range of new research questions arise. These include, but are not limited to the spatial and temporal variation of the energy transfers on a global scale in long time series.

Chapter 6

Summary and Conclusions

The ocean's response to a surface wind stress was studied with the aid of two numerical models. First, a non-linear, axisymmetric and Boussinesq simulation was set up to investigate the ocean response to a wind stress associated to an isolated, idealized storm (Chapter 2). Then the commonly used slab model of Pollard and Millard (1970) was revisited and its parameter dependencies as well as its resonance behavior were analyzed (Chapter 3). An extension to the classical slab model introduced by Olbers et al. (2012) was presented, analyzed with respect to its model parameters and tested against a number of idealized scenarios (Chapter 3). The application of the resulting hybrid slab model to the North Atlantic showed its applicability. Results from the regional runs were interpreted in the context of the parameter dependencies of the model and the previously conducted idealized experiments. Forcing the hybrid slab model with the same axisymmetric wind stress, the responses of the hybrid slab and the axisymmetric models were compared (Chapter 4). Moreover, the influence of the lateral movement of the storm was analyzed. Finally, some suggestions for improving the applied methods were made and a first application of the hybrid slab model to a global setup was presented (Chapter 5).

The axisymmetric simulation revealed three phases in the response to the wind stress pulse. At first, an azimuthal vortex underneath the storm and a radially outward motion with a corresponding deeper return flow were formed. This structure was associated with a bottom intensified pressure anomaly. In the second phase, the structure was oscillating with the Coriolis frequency. Whereas the resulting vertical motion, i.e. the inertial pumping, excited low mode internal gravity waves, the oscillation of the pressure anomaly also excited higher modes. The last phase was governed by the diffusive adjustment of the vortex towards the geostrophic equilibrium. Most of the energy radiated in the IGW packets was contained in the low modes excited by the inertial

pumping. Approximately 90 % of the energy supplied by the wind was dissipated close to the surface. Around 10 % was transferred to the mechanical energy of the vortex. Surprisingly, the energy radiated as IGW was only about 0.01 %. This is $2-3$ orders of magnitude smaller than observed in circulation models and measured in the ocean (e.g. Price, 1983; D'Asaro et al., 1995; Alford et al., 2012; Rimac et al., 2016). Suggested drivers of stronger vertical motion and thus larger energy fluxes are a range of other processes like surface heat fluxes, turbulent motion, the collapse of mixed regions or the translation of the storm, not included in the model.

In addition to the detailed axisymmetric model, the simple and commonly used slab model (Pollard and Millard, 1970) was revisited (Section 3.1.2). From the response to a harmonic forcing and the dominant wind stress spectrum it could be shown that the wind power estimated with the classical slab model is linearly dependent on the damping parameter r. In contrast, the resonance peak at the negative Coriolis frequency $\sigma = -f$ is of minor importance for typical values of r. Hence, it was concluded that the choice for the damping parameter is more important than commonly argued. Another difficulty is related to the possible discrepancy between the mixed layer depth and the actual depth of wind penetration.

The hybrid slab model proposed by Olbers et al. (2012) incorporates the classical slab model. Additionally, the vertical velocity associated to the inertial oscillations is computed and assumed to be a boundary condition to an internal gravity wave field below. Thus, one can conclude on the resulting energy flux relation (Eq. 3.16). Besides the square of the vertical velocity, filtered between the Coriolis and the buoyancy frequency, it is linearly dependent on the horizontal length scale, L_{h}, and the buoyancy frequency just below the mixed layer base, $N(z = H_{\mathrm{m}})$. In contrast to the wind power, it is independent of the mixed layer depth H_{m}.

The application of the hybrid slab model to a range of idealized scenarios visualized the dependencies of the energy flux estimates on the wind field structure and the associated horizontal length scales (Section 3.3). It was found that laterally moving wind stress fronts drive large vertical velocities by generating phase shifts along their track. They are initiated by the time shifted, oscillatory response to the same forcing and depend on the local residence time of the wind stress and thus on the width of the front and its lateral speed. Ratios of energy leaving the mixed layer to wind work between 20 % and 60 % were

observed. The β-effect results in energy flux ratios of the order 1 % but can modify the response to a front by prolonging or destroying the coherence of the inertial oscillations in the wake of the front. Lastly, strong gradients in coherent wind stress structures may lead to energy flux ratios up to 10 %.

Simulations of the North Atlantic for the two years 1989 and 1996 were set up as examples for different wind forcing, related to the opposite phase of the North Atlantic Oscillation. Wind stresses from the NCEP-CFSR reanalysis and mixed layer depths as well as the associated buoyancy frequencies from the MIMOC climatology were used. The horizontal wavelengths, L_h, were estimated using boxed Fourier transforms of the vertical velocity field, the damping parameter, r, was assumed to be constant (Section 3.2 and Appendix B.2). In those runs the structures examined in the idealized scenarios were rediscovered. Moreover, it was found that there are meridional regimes in terms of latitude bands that are characterized by distinct energy flux ratios (Section 3.4). The tropics (i.e. south of 20°N) are governed by somewhat spatially coherent but variable wind stresses. The corresponding energy flux ratio was found to be below 5 % and associated to the β-effect. In subtropical regions (i.e. between 20°N and 40°N) the energy flux ratios plateau at about 12 %. They are associated to slowly advancing fronts related to mid-latitude pressure systems and isolated hurricane tracks. North of 40°N, the wind stress is characterized by fast moving pressure systems with high variability. They lead to intermediate energy flux ratios about 10 %. This behavior could only partially be correlated to the input parameters. In addition, the difference in the average wind stress amplitudes between the two years influenced the total energy radiated and the wind work but not their ratio. It is therefore concluded that the spatial distribution of energy transfer to IGWs depends very much on the structure of the wind stress.

The two models have been compared with a twofold aim (Chapter 4). On the one hand, the axisymmetric model may serve as a benchmark of what mechanisms the hybrid slab model can reproduce. On the other hand the hybrid slab model may give insights on the reasons why the axisymmetric simulation results in a radiated energy flux that is several orders of magnitude smaller than observed. The former was achieved by applying the hybrid slab model to the axisymmetric control setup. It was found that the inertial amplitude predicted with the hybrid slab model was larger by a factor of about 8. Moreover, the non-linear response, i.e. the formation of a vortex underneath the wind stress, was not reproduced. This led to a similar estimate of the wind work even

though the inertial amplitude was significantly larger. Despite the magnitude, the radial and vertical velocities were very similar in structure. The difference is associated with the distinct characters of surface forcing. Where the wind and internal stresses lead to 90 % dissipation within the topmost three bins in the axisymmetric simulation, the forcing of the classical slab model is effectively a body force - evenly distributed over the whole surface slab. Due to the square dependency on the vertical velocity, the flux into the internal gravity wave field was increased by a factor of 64.

However, it must be mentioned that the comparison of two models with fundamentally different underlying physics does not allow for any conclusion on the reproduction of nature. None of the two approaches claims to be *more true* than the other and the comparison can therefore only highlight differences and in the best case deliver indicators for strengths and weaknesses of the approaches. For instance, in the present case it remains unclear whether the surface stress parameterization in combination with the rigid lid is closer to nature than a body force implementation.

One of the suggested reasons why the internal wave energy radiated in the axisymmetric model was low compared to observations was the missing lateral movement of the storm structure. In order to characterize its role, the hybrid slab model is set up for a wind stress with the same structure as before but moving across the domain. It was found that the wind power in the wake of the moving storm was asymmetric with higher values to the right of the track. To the left, the wind stress and the inertial oscillation rotate in an opposite sense and counteract each other after roughly half a period. Hence, the wind work is reduced. The vertical velocity and thus the associated energy flux are not shifted with respect to the storm track and therefore do not experience the described reduction. Moreover, the wavelength in the wake is set by the lateral speed of the structure. For any storm faster than approximately $6\,\mathrm{km\,h^{-1}}$ the corresponding length scale is larger than the length scale given by the structure of the storm. This threshold for the translation speed is fairly slow compared to observations (Price et al., 1991). Both effects lead to an increase of the energy flux ratio from 1.1 % to 30.6 %. Thus, the lateral movement of the storm is likely to be an important factor for the efficiency of the energy transfer.

The analysis of the hybrid slab model with idealized scenarios and the example of a regional simulation in the North Atlantic as well as the comparison to the non-linear, axisymmetric simulation showed that the formulation can be used

to identify structures that efficiently generate inertial pumping and therefore IGWs. Furthermore, it is a cost-efficient, quantitative measure of the energy radiated into the internal gravity wave field that may be available for mixing the deep ocean. As an example, the integrals over the whole North Atlantic result in an energy flux ratio of approximately 9 % for both years. Within the error margins, this agrees e.g. with the estimates of Rimac et al. (2016) and Alford et al. (2012). However, both the parameters L_h and r are important sources of uncertainties in this approach.

A first application of the hybrid slab model in a global setup with 10 years data and a constant horizontal wavelength, $L_\mathrm{h} = 400\,\mathrm{km}$, was presented. The estimated global average wind work, 0.5 TW, and the spatial distribution of the average seasonal wind power agree well with previous studies (Alford, 2001; Watanabe and Hibiya, 2002; Alford, 2003; Rimac et al., 2013). Systematically too low estimates of the energy radiated as internal gravity waves and the higher values found for simulations of the North Atlantic suggest that a robust estimate of the horizontal wavelength, L_h, is needed. The method of spatial autocorrelations is proposed as a potential solution.

Robust global simulations of the hybrid slab model potentially answer a range of new research questions. These include, but are not limited to the spatial and temporal variation of the energy transfers on a global scale in long time series.

Appendix A

Appendix to the Axisymmetric Simulation

A.1 A 4^{th} Order Wave Number Cutoff Filter

The relation between the azimuthal vorticity ζ and the stream function ψ in the radius-depth plane is given by Eq. (2.6). In particular,

$$\Delta_r \psi - \frac{\psi}{r^2} = -\zeta \tag{A.1}$$

with the Laplace operator in radial coordinates $\Delta_r = r^{-1}\partial/\partial_r(r\partial/\partial_r) + \partial^2/\partial_z^2$. Note that this is the Poisson equation in cylindrical coordinates. The no-normal flow conditions on the top and the bottom boundary of the domain imply that the stream function is zero at both boundaries. Moreover, the stream function is zero at the inner boundary, i.e. at $r = 0$, due to the symmetry. Hence, the above equation can be solved using a Fourier-sine-transform in the vertical and a Bessel-transform of order $n = 1$ (Eq. 2.8) in the radial direction. However, strong gradients in the azimuthal vorticity may induce ringing in the discretized radial transform on a bounded interval. To suppress noise, a 4^{th} order exponential cutoff filter, adapted from LaCasce (1996), is introduced.

Consider the azimuthal vorticity ζ and its Fourier-Bessel transform

$$\mathcal{Z}(k_r, k_3) = \mathcal{F}_{\mathrm{FB}}(\zeta(r,z)) = \int_{-H}^{0}\int_{0}^{\infty} \sin(k_3 z) r J_1(k_r r)\zeta(r,z) dr\, dz, \tag{A.2}$$

in which J_1 is the Bessel function of the first kind of order $n = 1$, H is the depth of the domain, k_r is the radial and k_3 the vertical wave number. Due to the bounded domain and the no-normal flow boundary conditions, the vertical wave number is discretized so that $k_3 = l\pi/H$ with $l \in \mathbb{N}$. It is worth mentioning that the sine expansion in depth represents an orthonormal set of functions but is not equal to the vertical mode expansion in the present

stratification. With $\Psi = \mathcal{F}_{\mathrm{FB}}(\psi)$, Eq. (2.6) is solved by $\Psi = \mathcal{Z}/(k_r^2 + k_3^2)$ and the corresponding inverse transform. In the code, these are discretized transforms so that both the radial and the vertical wave number are discrete and have a maximum wave number corresponding to the Nyquist wave number - analogous to the Nyquist frequency. Suppose, a discrete transformed vorticity $\mathcal{Z}_n$ and maximal mode number n_{Ny} of the Fourier-Bessel series. The filter function is set up so that

$$\tilde{\mathcal{Z}}_n = \begin{cases} \mathcal{Z}_n, & 0 < n \leq n_{\mathrm{co}} \\ \mathcal{Z}_n \cdot \exp\left(-36.8(n - n_{\mathrm{co}})^4 (n_{\mathrm{Ny}} - n_{\mathrm{co}})^{-4}\right), & n_{\mathrm{co}} < n \leq n_{\mathrm{Ny}} \end{cases} \tag{A.3}$$

is the filtered coefficient of the azimuthal vorticity in the Fourier-Bessel space. The mode number n_{co} is equivalent to a radial cut-off length scale equal to 10 km. The factor -36.8 ($\ln(10^{-16})$) is determined by the double precision machine accuracy and the exponent, 4, is chosen so that the filter is smooth enough and does not cause ringing itself. This acts like a low pass filter for radial structures larger than the cut-off length scale.

Appendix B

Appendix to the Hybrid Model

B.1 Derivation of the Hybrid Slab Model (D. J. Olbers)

The following derivation and scale analysis was kindly supplied by Prof. Dr. Dirk J. Olbers.

We consider the equations of motion for the surface layer $-H_\mathrm{m} < z < 0$ with homogeneous density and constant Coriolis frequency,

$$\begin{aligned} \frac{\partial}{\partial t}\boldsymbol{u} + f\ \mathsf{R}\boldsymbol{u} + \boldsymbol{\nabla} p &= \frac{\partial \boldsymbol{\tau}}{\partial t} - r\ \boldsymbol{u} \\ \frac{\partial}{\partial t} w + \frac{\partial p}{\partial t} &= 0 \\ \boldsymbol{\nabla}\cdot\boldsymbol{u} + \frac{\partial w}{\partial t} &= 0 \end{aligned} \tag{B.1}$$

where p is the pressure, and w is the vertical velocity. The horizontal velocity $\boldsymbol{u}(x, y, z, t)$ may not be confused with the depth averaged horizontal velocity used in Section 3.1. For the wind-forced system the surface boundary condition at $z = 0$ is $\boldsymbol{\tau} = \boldsymbol{\tau}_0$ (the wind stress). Note that we have normalized here pressure and stress by the constant density. We are looking for a solution of the system (B.1) in Fourier space where the vertical velocity is represented as

$$w(\boldsymbol{x}, z, t) = \iiint\limits_{\mathbb{R}^3} \hat{w}(\boldsymbol{k}_h, z, \sigma) e^{i(\boldsymbol{k}_\mathrm{h}\cdot\boldsymbol{x}+\sigma t)}\, d\boldsymbol{k}_h\, d\sigma \tag{B.2}$$

and the other fields accordingly. The system of equations (B.1) is projected onto the vertical velocity (see also Olbers and Herterich, 1979; Olbers, 1986). The governing equation for $\hat{w}(\boldsymbol{k}_\mathrm{h}, z, \sigma)$ and the surface boundary condition, considered here as a rigid lid, are found to be

$$\frac{\partial^2 \hat{w}}{\partial z^2} - q^2 \hat{w} = \frac{\partial \mathcal{W}}{\partial t} \tag{B.3}$$

$$\hat{w} = 0 \qquad \text{at} \qquad z = 0 \tag{B.4}$$

with $q^2 = k_\mathrm{h}^2 \sigma^2/(\sigma^2 - f^2)$, $\sigma_r = ir - \sigma$ and the forcing term

$$\mathcal{W} \,=\, \frac{1}{\sigma_r^2 - f^2}\, \boldsymbol{\Omega}_r \cdot \frac{\partial \hat{\boldsymbol{\tau}}}{\partial t} \qquad \text{with} \qquad \boldsymbol{\Omega}_r \,=\, (\sigma_r + if\ \mathsf{R})\ \boldsymbol{k}_\mathrm{h} \tag{B.5}$$

We have omitted the small r-terms in the wave number quantity q appearing on the left-hand side of (B.3). The complete system (B.1) and also the $\hat{w}$-problem (B.3) require two vertical boundary conditions, i.e. apart from the surface rigid lid condition (B.4) we demand

$$\hat{w} \,=\, W \qquad \text{at} \qquad z = -H_\mathrm{m} \tag{B.6}$$

with a yet unknown pumping velocity $W = W(\boldsymbol{k}_\mathrm{h}, \sigma)$. To match the mixed layer field to the stratified interior below the mixed layer base we assume continuity of $\hat{w}$ and $\partial\hat{w}/\partial z$ at the mixed layer base $z = -H_\mathrm{m}$. The unknown W will then be determined by these matching conditions. Once the vertical velocity $\hat{w}$ is determined the remaining fields $\hat{\boldsymbol{u}}$ and $\hat{p}$ follow by diagnostic relations (not considered here).

In the stratified ocean below the mixed layer a perturbation with wave vector $\boldsymbol{k}_\mathrm{h}$ and frequency σ is an internal wave having a vertical velocity $\hat{w}_{iw} = \hat{w}_{iw}(\boldsymbol{k}_\mathrm{h}, z, \sigma)$. The equation governing $\hat{w}_{iw}$ is the same as (B.3), but with zero forcing and augmented by the appropriate stratification term, hence

$$\frac{\partial^2 \hat{w}_{iw}}{\partial z^2} + k_3^2(z)\, \hat{w}_{iw} \,=\, 0 \tag{B.7}$$

with the squared vertical wave number $k_3^2(z) \,=\, k_\mathrm{h}^2 (N^2(z) - \sigma^2)/(\sigma^2 - f^2)$. Locally the wave has the vertical dependence $\sim \exp i \int^z k_3(z')dz'$, propagating in the Brunt-Väisälä frequency profile $N(z)$. We require a positive k_3 to have downward group velocity (see e.g. Olbers et al., 2012). This is the radiation condition. The matching conditions become

$$\hat{w} \,=\, \hat{w}_{iw} \,=\, W \qquad \text{and} \qquad \frac{\partial \hat{w}}{\partial t} \,=\, \frac{\partial \hat{w}_{iw}}{\partial t} \qquad \text{at} \qquad z = -H_\mathrm{m} \tag{B.8}$$

and result in

$$\left.\frac{\partial \hat{w}}{\partial t}\right|_{z=-D} \,=\, ik_3 W \tag{B.9}$$

where k_3 is here the value of the vertical wave number just below the mixed layer base. The $\hat{w}$-problem (B.3) with the boundary conditions (B.4) and (B.6) can be solved by a Green's function approach, pursued in a companion paper (Jurgenowski et al., 2017, in preparation). Here we restrict the analysis to the long-wave approximation of (B.3) which leads to the hybrid slab model and is easy to solve. The long-wave approximation is the limit $(k_\mathrm{h}H_\mathrm{m})^2 \ll 1$, i.e. the wavelength must large compared to the mixed layer depth which is satisfied for any relevant forcing condition. To proceed with (B.3) we need, however, $(qH_\mathrm{m})^2 \ll 1$. Writing the long-wave condition in terms of q we find $(k_\mathrm{h}H_\mathrm{m})^2 = (qH_\mathrm{m})^2(1 - f^2/\sigma^2) \ll 1$. For $\sigma^2 \gg f^2$ the condition $(k_\mathrm{h}H_\mathrm{m})^2 \ll 1$ is thus equivalent to $(qH_\mathrm{m})^2 \ll 1$. For σ only slightly exceeding f, say $\sigma = (1+\epsilon/2)f$ with $\epsilon \ll 1$, the long-wave condition leads to $(qH_\mathrm{m})^2 \ll \epsilon^{-1}$. Observed near-inertial peaks occur typically at $\epsilon \sim 0.01$ so $(qH_\mathrm{m})^2$ might be much larger than 1 for near-inertial frequencies and an expansion of (B.3) is spoiled. To allow for a simple expansion of (B.3), requiring $(qH_\mathrm{m})^2 \ll 1$, we are faced with $(k_\mathrm{h}H_\mathrm{m})^2 \ll 1 - f^2/\sigma^2 \ll 1$ for all frequencies. Again, one may set $\sigma = (1 + \epsilon/2)f$ with $\epsilon \ll 1$ so that the stronger condition $k_\mathrm{h}H_\mathrm{m} \ll \epsilon \ll 1$ is required at very low frequencies. Taking a wavelength of 10 km, which is satisfied even for realistic mesoscale wind systems, and $H_\mathrm{m} \sim 100\,\mathrm{m}$ we obtain $(k_\mathrm{h}H_\mathrm{m})^2 = 0.004$. The condition $(qH_\mathrm{m})^2 \ll 1$ is thus consistent with the long-wave limit but not equivalent.

We thus consider (B.3) for the limit $(qH_\mathrm{m})^2 \ll 1$. Integrating twice with the boundary conditions (B.4) and (B.6) and the matching condition (B.9) we find

$$W = -K\frac{\Omega_r \cdot \hat{\boldsymbol{\tau}}_0}{\sigma_r^2 - f^2} \qquad \text{with} \qquad K = \frac{1}{1 + ik_3H_\mathrm{m}} \tag{B.10}$$

To determine the radiation flux $(WP^* + c.c.)/2$ at the mixed layer base we need the pressure field P. Here we use the relation of vertical velocity and pressure for a downward propagating internal wave (see e.g. Olbers et al., 2012), namely

$$\hat{p}_{iw} = -\frac{(N^2 - \sigma^2)^{1/2}(\sigma^2 - f^2)^{1/2}}{\sigma k_\mathrm{h}}\hat{w}_{iw} \tag{B.11}$$

At mixed layer base, with the continuity conditions $W = \hat{w}_{iw}(z = -H_\mathrm{m})$, $P = \hat{p}_{iw}(z = -H_\mathrm{m})$, the radiative energy flux becomes

$$\phi(\boldsymbol{k}_\mathrm{h}, -H_\mathrm{m}, \sigma) = \frac{1}{2}(WP^* + c.c.)$$
$$= -\frac{(N^2-\sigma^2)^{1/2}(\sigma^2-f^2)^{1/2}}{\sigma k_\mathrm{h}}\,(W(\boldsymbol{k}_\mathrm{h}, \sigma)W^*(\boldsymbol{k}_\mathrm{h}, \sigma)) \qquad \text{(B.12)}$$

which is Eq. (3.13) in the main text.

A closer inspection of the hybrid model, however, reveals that the slab model momentum equation (Eq. 3.1) and the continuity equation (Eq. 3.12) yield (B.10) with $K \equiv 1$. The hybrid slab model thus results if a further condition is satisfied, namely $(k_3 H_\mathrm{m})^2 \ll 1$. Phrased in terms of q this becomes $(qH_\mathrm{m})^2 \ll (\sigma/N)^2$, which implies $(k_\mathrm{h} H_\mathrm{m})^2 \ll \epsilon(f/N)^2$.

B.2 Technical Details of the Hybrid Slab Model Implementation

The implementation of the model follows a complex Fourier transform scheme based on the complex notation of Eq. (3.3) (D'Asaro, 1985). Since the discrete fast Fourier transform on bounded intervals, in this case one year, assumes periodicity of the input, transition signals occur after transforming back. To avoid these numerical errors the untransformed source function is zero padded corresponding to three decay time scales $t_d = 1/r$. That means the wind stress is virtually switched off at the end of the time series and the corresponding response of the horizontal velocity is an oscillating decay $\boldsymbol{u} = \exp(-rt)\ (u_0\cos(ft), v_0\sin(-ft))$. This decay is cut off so that time frames match and the best estimates for mixed layer velocities with initial conditions approximately zero are achieved. However, this procedure introduces a small ringing effect at the beginning of the time series, if the wind stress at model time $t = 0$ is non-zero. Vertical velocities were calculated with midpoint divergences according to Eq. (3.12).

It was shown that the energy flux into the surface slab depends linearly on the damping parameter r for a pink to red wind stress spectrum (cf. Section 3.1.2). For a consistent choice of the parameter r, data from 42 sites with 61 independently measured time series were analyzed. In particular, measured currents below the water surface were compared to modeled currents from measured wind speeds. The data sets were taken from the Global Tropical Moored Buoy Array (GTMBA) (McPhaden, 2010), the Woods Hole - Hawaii Ocean Time-series Site (WHOTS) (Karl and Lukas, 1996), the Stratus mooring, the

Monterey Ocean Observing System (MOOS) (Chaffey et al., 2001), and the ocean station Papa. Available data with both wind and current measurements is sparse for latitudes beyond 20° N. The method closely followed the procedure of Alford (2001). Measured mixed layer currents were correlated with modeled currents from measured winds at the buoy sites. A range of damping parameters was taken into account and the parameter corresponding to the highest correlation coefficient were considered optimal at the buoy position. To guarantee meaningful results time series with correlation coefficients smaller than 0.5, optimal damping parameters at the boundaries of the considered interval and damping parameters larger than half the local Coriolis frequency were disregarded. In total 38 time series remained after all filters were applied (Fig. B.1). This way an estimate for the damping parameter was achieved. However, this approach also has a number of problems.

The model does not resolve a variety of physical processes like surface wave dynamics, stirring of the mixed layer or entrainment at the mixed layer base. These mechanisms may result not only in temporal but also in spatial dependencies. Available data from buoys equipped with instruments measuring both wind and ocean surface currents are sparse and insufficient for evaluating neither the spatial nor the temporal variability. Evaluations of the damping parameter r with many independently measured time series from the same buoy results in a large spread of values. The consequently low precision is reflected in the large standard deviations in Fig. B.1. In addition, the model may become less reliable as the stability criterion $r \ll f$ is violated. Also, Alford (2003) pointed out that a frequency dependent damping might be necessary to achieve more realistic modeled ocean currents.

Averaging over time and grouping into ocean basins Park et al. (2009) showed that drifter tracks in the North Atlantic differ from the other oceans. They observed an almost constant e-fold damping time scale of approximately 5 days and thus no dependence on latitude in the North Atlantic. Despite the large spread, the present results correspond to their findings within the confidence interval (Fig. B.1). Since the calculations are done for the North Atlantic only, a constant damping parameter $r = 1/5$ days is used.

Additionally, the dominant horizontal wave number needs to be identified. The horizontal spectrum of the vertical velocity is evaluated with the aid of boxed Fourier transforms. Square boxes around an array of fixed positions were multiplied by Hamming windows in both meridional and zonal direction.

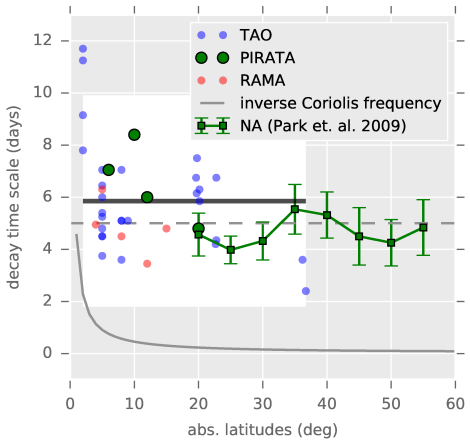

Figure B.1: Results from the evaluation procedure, inverse damping parameter r^{-1} plotted against absolute latitude. Round points originate in the present analysis whereas square points are inserted from Park et al. (2009). The black line is the arithmetic mean, the white shading depicts the 95% confidence interval. The dashed and solid grey lines mark a decay time of 5 days and the inverse Coriolis frequency. The results are color coded by ocean basin: red, blue and green points represent results from the Indian Ocean, the Pacific Oceans and the North Atlantic, respectively.

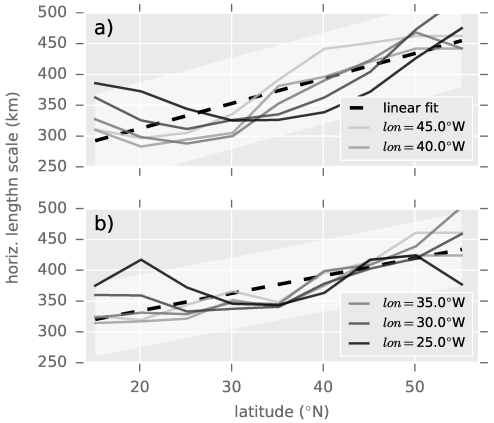

Figure B.2: Linear fits to horizontal length scales from boxed Fourier transform spectra for different longitudes for years 1989 (a) and 1996 (b). White shadings show 95% confidence intervals. Dominant length scales were derived with an asymptotic method to eliminate effects of limited box sizes.

The corresponding meridional and zonal wave number spectra were calculated and averaged over the box. Wave numbers corresponding to the maxima of these spectra were combined to a dominant horizontal wave number $2\pi/L_\mathrm{h}$. Since this estimate depends on the chosen box size the analysis was repeated for box lengths between 3 and 30 points. Moreover, it was done for every time step of the year and averaged temporally. In order to evaluate the horizontal length scale of a virtually infinite box an asymptotic function of the form $A_i \arctan(B_i\ d)$ with parameters A_i and B_i, and zonal width of the box d was fitted to the results. The amplitude A_i divided by $\frac{\pi}{2}$ was then assumed to be the asymptotic dominant length scale. A grid of 5x9 positions between $(15°\mathrm{N}, 45°\mathrm{W})$ and $(55°\mathrm{N}, 25°\mathrm{W})$ was taken into account to find a latitude dependent linear parameterization. The results for 1989 and 1996 are displayed

in Table 3.1 and visualized in Fig. B.2. The maximum deviations within the 95% confidence intervals from the linear fits lead to errors up to 26% and 19% for 1989 and 1996, respectively.

B.3 Design of the Fourier Filter in the Hybrid Model

The Fourier space energy fluxes from the mixed layer into the internal wave field are given by Eq. (3.13). Taking into account that $F(\sigma)$ is real one observes:

$$\begin{aligned}
&\int_f^N F(\sigma)\left(\hat{w}(\boldsymbol{k}_\mathrm{h},\sigma,H_\mathrm{m})\hat{w}^*(\boldsymbol{k}_\mathrm{h},\sigma,H_\mathrm{m})\right)d\sigma \\
&=\int_f^N \left(\sqrt{F(\sigma)}\hat{w}(\boldsymbol{k}_\mathrm{h},\sigma,H_\mathrm{m})\sqrt{F(\sigma)}^*\hat{w}^*(\boldsymbol{k}_\mathrm{h},\sigma,H_\mathrm{m})\right)d\sigma \\
&=\int_{-\infty}^{\infty}\left|\Theta(\sigma-f)\Theta(N-\sigma)\sqrt{F(\sigma)}\hat{w}(\boldsymbol{k}_\mathrm{h},\sigma,H_\mathrm{m})\right|^2 d\sigma,
\end{aligned} \tag{B.13}$$

where $\Theta(\sigma) = \Theta^2(\sigma)$ denotes the Heaviside function. Applying Parseval's theorem and defining

$$\hat{\eta} = \Theta(\sigma-f)\Theta(N-\sigma)\sqrt{F(\sigma)},$$

one has:

$$\int_{-\infty}^{\infty}\left|\hat{\eta}(\sigma)W(\boldsymbol{k}_\mathrm{h},\sigma,H_\mathrm{m})\right|^2 d\sigma = \int_{-\infty}^{\infty}\left|\eta(t)*w(\boldsymbol{k}_\mathrm{h},t,H_\mathrm{m})\right|^2 dt. \tag{B.14}$$

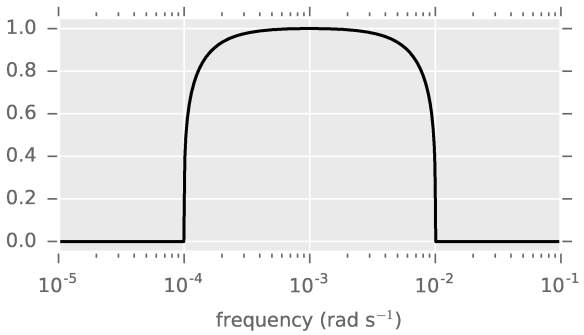

Figure B.3: The normalized window function $\hat{h}(\sigma)$ with $N = 10^{-2}$ rad s^{-1} and $f = 10^{-4}$ rad s^{-1}.

Normalizing so that $\max_\sigma(\hat{h}(\sigma)) = 1$ yields:

$$\hat{h}(\sigma) = \frac{\hat{\eta}(\sigma)}{\sqrt{N - |f|}}. \tag{B.15}$$

This way a classical Fourier transform filter, eliminating frequencies beyond N and f, is constructed. For visualization of the window function $\hat{h}(\sigma)$ see Fig. B.3.

Declaration of Originality

I, Georg S. Voelker, declare that this thesis is my own work except where acknowledged otherwise. Large parts of Chapter 3 are submitted to the *Journal of Physical Oceanography* and currently under review (Voelker et al., 2017). Appendix B.1 was contributed by Prof. Dr. Dirk J. Olbers and is appended here for reasons of completeness. His ownership is stated at the beginning of the corresponding Section.

Georg S. Voelker February 14, 2017

Bibliography

Alford, M. H., 2001: Internal swell generation: The spatial distribution of energy flux from the wind to mixed layer near-inertial motions. *Journal of Physical Oceanography*, **31 (8)**, 2359–2368, doi:10.1175/1520-0485(2001)031⟨2359:ISGTSD⟩2.0.CO;2.

Alford, M. H., 2003: Improved global maps and 54-year history of wind-work on ocean inertial motions. *Geophysical Research Letters*, **30 (8)**, 1424, doi:10.1029/2003GL018026.

Alford, M. H., M. F. Cronin, and J. M. Klymak, 2012: Annual cycle and depth penetration of wind-generated near-inertial internal waves at ocean station papa in the northeast pacific. *Journal of Physical Oceanography*, **42 (6)**, 889–909, doi:10.1175/JPO-D-11-092.1.

Alford, M. H., and M. C. Gregg, 2001: Near-inertial mixing : Modulation of shear , strain and wave in the banda sea at low latitude. *Journal of Geophysical Research*, **106 (C8)**, 16 947–16 968.

Alford, M. H., A. Y. Shcherbina, and M. C. Gregg, 2013: Observations of near-inertial internal gravity waves radiating from a frontal jet. *Journal of Physical Oceanography*, **43 (2012)**, 130305125949 003, doi:10.1175/JPO-D-12-0146.1.

Alford, M. H., and M. Whitmont, 2007: Seasonal and spatial variability of near-inertial kinetic energy from historical moored velocity records. *Journal of Physical Oceanography*, **37 (8)**, 2022–2037, doi:10.1175/JPO3106.1.

Bars, M. L., D. Lecoanet, S. Perrard, A. Ribeiro, L. Rodet, J. M. Aurnou, and P. L. Gal, 2015: Experimental study of internal wave generation by convection in water. *Fluid Dynamics Research*, **47 (4)**, 045 502, doi:10.1088/0169-5983/47/4/045502.

Chaffey, M., E. Mellinger, and W. Paul, 2001: Communications and power to the seafloor: Mbari's ocean observing system mooring concept. *OCEANS*

2001 MTS/IEEE: AN OCEAN ODYSSEY, VOLS 1-4, CONFERENCE PROCEEDINGS, MARINE TECHNOLOGY SOC, 1828 L ST NW,SUITE 906, WASHINGTON, DC 20035 USA, Marine Technol Soc; IEEE; OES; Minerals, Met & Mat Soc; Soc Explorat Geophysicists; Amer Geophys Union; Womens Aquat Network; Coasts, Oceans, Ports & Rivers Inst; Amer Meteorol Soc; Oceanog Soc, 2473–2481.

Chaigneau, A., O. Pizarro, and W. Rojas, 2008: Global climatology of near-inertial current characteristics from lagrangian observations. *Geophysical Research Letters*, **35 (13)**, 1–5, doi:10.1029/2008GL034060.

Condron, A., and I. a. Renfrew, 2012: The impact of polar mesoscale storms on northeast atlantic ocean circulation. *Nature Geoscience*, **6 (1)**, 34–37, doi:10.1038/ngeo1661.

D'Asaro, E. A., 1985: The energy flux from the wind to near-inertial motions in the surface mixed layer. *Journal of Physical Oceanography*, **15 (8)**, 1043–1059, doi:10.1175/1520-0485(1985)015⟨1043:TEFFTW⟩2.0.CO;2.

D'Asaro, E. A., and Coauthors, 1995: Upper-ocean inertial currents forced by a strong storm. part I: Data and comparisons with linear theory. *Journal of Physical Oceanography*, **25 (11)**, 2909–2936.

de Boyer Montégut, C., G. Madec, A. S. Fischer, A. Lazar, and D. Iudicone, 2004: Mixed layer depth over the global ocean: An examination of profile data and a profile-based climatology. *Journal of Geophysical Research C: Oceans*, **109 (12)**, 1–20, doi:10.1029/2004JC002378.

Dippe, T., X. Zhai, R. J. Greatbatch, and W. Rath, 2015: Interannual variability of wind power input to near-inertial motions in the north atlantic. *Ocean Dynamics*, **65 (6)**, 859–875, doi:10.1007/s10236-015-0834-x.

Dohan, K., and R. E. Davis, 2011: Mixing in the transition layer during two storm events. *Journal of Physical Oceanography*, **41 (1)**, 42–66, doi:10.1175/2010JPO4253.1.

Duck, P. W., and M. R. Foster, 2001: Spin-up of homogeneous and stratified fluids. *Annual Review of Fluid Mechanics*, **33**, 231–263.

Ekman, V. W., 1905: *On the influence of the earths rotation on ocean-currents*. Bd 2. n:o ed., Arkiv for matematik, astronomi u. fysik, Uppsala.

Elipot, S., R. Lumpkin, and G. Prieto, 2010: Modification of inertial oscillations by the mesoscale eddy field. *Journal of Geophysical Research: Oceans*, **115 (9)**, C09 010, doi:10.1029/2009JC005679.

Emanuel, K. A., 1986: An air-sea interaction theory for tropical cyclones. Part I: Steady-state maintenance. *Journal of the Atmospheric Sciences*, **43 (6)**, 585–605, doi:10.1175/1520-0469(1986)043⟨0585:AASITF⟩2.0.CO;2.

Firing, E., R.-C. Lien, and P. Muller, 1997: Observations of strong inertial oscillations after the passage of tropical cyclone Ofa. *Journal of Geophysical Research: Oceans*, **102 (C2)**, 3317–3322, doi:10.1029/96JC03497.

Forryan, A., A. C. Naveira Garabato, K. L. Polzin, and S. Waterman, 2015: Rapid injection of near-inertial shear into the stratified upper ocean at an antarctic circumpolar current front. *Geophysical Research Letters*, 3431–3441, doi:10.1002/2015GL063494.

Fu, L., 1981: Observations and models of inertial waves in the deep ocean. *Reviews of Geophysics*, **19 (1)**, 141–170, doi:10.1029/RG019i001p00141.

Furuichi, N., T. Hibiya, and Y. Niwa, 2008: Model-predicted distribution of wind-induced internal wave energy in the world's oceans. *Journal of Geophysical Research: Oceans*, **113 (9)**, C09 034, doi:10.1029/2008JC004768.

Garrett, C., and W. Munk, 1972: Space-time scales of internal waves. *Geophysical Fluid Dynamics*, **3 (October)**, 225–264, doi:10.1080/03091927208236082.

Gill, A. E., 1984: On the behavior of internal waves in the wakes of storms. *Journal of Physical Oceanography*, **14 (7)**, 1129–1151, doi:10.1175/1520-0485(1984)014⟨1129:OTBOIW⟩2.0.CO;2.

Gille, S. T., 2005: Statistical characterization of zonal and meridional ocean wind stress. *Journal of Atmospheric and Oceanic Technology*, **22 (9)**, 1353–1372, doi:10.1175/JTECH1789.1.

Griffies, S., 2004: *Fundamentals of Ocean Climate Models*. Princeton University Press, Princeton, N.J., 528 pp.

Griffies, S. M., and Coauthors, 2000: Developments in ocean climate modelling. *Journal of Computational Physics*, **2 (3-4)**, 123–192, doi:10.1016/S1463-5003(00)00014-7.

Haidvogel, D. B., and A. Beckmann, 1999: *Numerical ocean circulation modeling - Series on environmental science and management ; vol. 2)*. Imperial College Press, London.

Holdsworth, A. M., and B. R. Sutherland, 2013: Influence of lock aspect ratio upon the evolution of an axisymmetric intrusion. *Journal of Fluid Mechanics*, **735**, 1–11, doi:10.1017/jfm.2013.517.

Holte, J., and L. Talley, 2009: A new algorithm for finding mixed layer depths with applications to argo data and subantarctic mode water formation. *Journal of Atmospheric and Oceanic Technology*, **26 (9)**, 1920–1939, doi:10.1175/2009JTECHO543.1.

Hurrell, J. W., and C. Deser, 2009: North atlantic climate variability: The role of the north atlantic oscillation. *Journal of Marine Systemsystems*, **78 (1)**, 28–41, doi:10.1016/j.jmarsys.2008.11.026.

IPCC Working Group 1, 2014: Ipcc fifth assessment report (ar5) - the physical science basis. *IPCC*, doi:10.1017/CBO9781107415324.004, arXiv:1011.1669v3.

Jensen, T. G., 1998: Open boundary conditions in stratified ocean models. *Journal of Marine Systems*, **16 (3-4)**, 297–322.

Jung, T., S. Serrar, and Q. Wang, 2014: The oceanic response to mesoscale atmospheric forcing. *Geophysical Research Letters*, **41 (4)**, 1255–1260, doi:10.1002/2013GL059040.

Jurgenowski, P., D. Olbers, and C. Eden, 2017: Wind-driven radiation of internal gravity waves from the surface mixed layer. *in preparation*.

Kang, D., and O. Fringer, 2010: On the calculation of available potential energy in internal wave fields. *Journal of Physical Oceanography*, **40 (11)**, 2539–2545, doi:10.1175/2010JPO4497.1.

Karl, D. M., and R. Lukas, 1996: The Hawaii Ocean Time-series (HOT) program: Background, rationale and field implementation. *Deep Sea Research Part II: Topical Studies in Oceanography*, **43 (2)**, 129–156, doi:10.1016/0967-0645(96)00005-7.

Käse, R. H., and D. J. Olbers, 1980: Wind-driven inertial waves observed during phase III of gate. *Deep-Sea Research*, **26 (December)**, 191–216, doi:10.1016/B978-1-4832-8366-1.50015-7.

Kilbourne, B. F., and J. B. Girton, 2015: Quantifying high-frequency wind energy flux into near-inertial motions in the southeast pacific. *Journal of Physical Oceanography*, **45 (2)**, 369–386, doi:10.1175/JPO-D-14-0076.1.

Kundu, P. K., 1976: An analysis of inertial oscillations observed wear oregon coast. *Journal of Physical Oceanography*, **6 (6)**, 879–893, doi:10.1175/1520-0485(1976)006⟨0879:AAOIOO⟩2.0.CO;2.

Kunze, E., 1985: Near-inertial wave propagation in geostrophic shear. *Journal of Physical Oceanography*, **15 (5)**, 544–565, doi:10.1175/1520-0485(1985)015⟨0544:NIWPIG⟩2.0.CO;2.

LaCasce, J. H., 1996: Baroclinic vortices over a sloping bottom. Ph.D. thesis, MIT / WHOI.

Leaman, K. D., 1976: Observations on the vertical polarization and energy flux of near-inertial waves. *Journal of Physical Oceanography*, **6 (6)**, 894–908, doi:10.1175/1520-0485(1976)006⟨0894:OOTVPA⟩2.0.CO;2.

Leaman, K. D., and T. B. Sanford, 1975: Vertical energy propagation of inertial waves : A vector spectral analysis of velocity profiles. *Journal of Geophysical Research*, **80 (15)**, 1975–1978.

Lecoanet, D., M. Le Bars, K. J. Burns, G. M. Vasil, B. P. Brown, E. Quataert, and J. S. Oishi, 2015: Numerical simulations of internal wave generation by convection in water. *Physical Review E - Statistical, Nonlinear, and Soft Matter Physics*, **91 (6)**, 1–10, doi:10.1103/PhysRevE.91.063016, arXiv:1412.3109v2.

Levine, M. D., and V. Zervakis, 1995: Near-inertial wave propagation into the pycnocline during ocean storms: Observations and model comparison. *Journal of Physical Oceanography*, **25 (11)**, 2890–2908, doi:10.1175/1520-0485(1995)025⟨2890:NIWPIT⟩2.0.CO;2.

Lvov, Y. V., K. L. Polzin, and E. G. Tabak, 2004: Energy spectra of the ocean's internal wave field: theory and observations. *Physical review letters*, **92 (12)**, 128 501, doi:10.1103/PhysRevLett.92.128501.

Marshall, J., and F. Schott, 1999: Open-ocean convection: Observations, theory, and models. *Reviews of Geophysics*, **37 (98)**, 1–64, doi:10.1029/98RG02739.

McDougall, T. J., and P. M. Barker, 2011: Getting started with teos-10 and the gibbs seawater (gsw) oceanographic toolbox. *Scor/Iapso Wg127*, 28, doi: SCOR/IAPSOWG127.

McMillan, J. M., and B. R. Sutherland, 2010: The lifecycle of axisymmetric internal solitary waves. *Nonlinear Processes in Geophysics*, **17 (2010)**, 443–453, doi:10.5194/npg-17-443-2010.

McPhaden, M., 2010: The global tropical moored buoy array. *Proceedings of OceanObs'09: Sustained Ocean Observations and Information for Society*, 668–682, 1, doi:10.5270/OceanObs09.cwp.61.

Moran, P. A. P., 1950: Notes on continuous stochastic phenomena. *Biometrika*, **37 (1)**, 17–23, doi:10.2307/2332142.

Moulin, F. Y., and J.-B. Flór, 2004: On the spin-up by a rotating disk in a rotating stratified fluid. *Journal of Fluid Mechanics*, **516**, 155–180, doi: 10.1017/S0022112004000655.

Munk, W., and C. Wunsch, 1998: Abyssal recipes II: energetics of tidal and wind mixing. *Deep Sea Research Part I: Oceanographic Research Papers*, **45 (12)**, 1977–2010, doi:10.1016/S0967-0637(98)00070-3.

Munk, W. H., 1950: On the wind-driven ocean circulation. *Journal of Meteorology*, **7 (2)**, 80–93, doi:10.1175/1520-0469(1950)007⟨0080:OTWDOC⟩2.0.CO;2.

Niwa, Y., and T. Hibiya, 1997: Nonlinear processes of energy transfer from traveling hurricanes to the deep ocean internal wave field. *Journal of Geophysical Research*, **102 (C6)**, 12,464–12,477, doi:10.1029/97JC00588.

Olbers, D., 1986: Internal gravity waves. *Landolt-Börnstein - Numerical data and functional relationships in science and technology - New Series, Group V, Volume 3a*, J. Sündermann, Ed., Springer Verlag, Berlin, 37–82.

Olbers, D., and K. Herterich, 1979: The spectral energy transfer from surface waves to internal waves. *Journal of Fluid Mechanics*, **92 (2)**, 349–379, doi: 10.1017/S0022112079000653.

Olbers, D., J. Willebrand, and C. Eden, 2012: *Ocean Dynamics*. Springer, Hidelberg, doi:10.1007/978-3-642-23450-7.

Paduan, J. D., R. A. De Szoeke, and R. A. Weller, 1989: Inertial oscillations in the upper ocean during the mixed layer dynamics experiment (mildex). *Journal of Geophysical Research*, **94**, 4835–4842.

Park, J. J., K. Kim, and R. W. Schmitt, 2009: Global distribution of the decay timescale of mixed layer inertial motions observed by satellite-tracked drifters. *Journal of Geophysical Research: Oceans*, **114 (11)**, C11 010, doi: 10.1029/2008JC005216.

Pinkel, R., 2005: Near-inertial wave propagation in the western arctic. *Journal of Physical Oceanography*, **35 (5)**, 645–665, doi:10.1175/JPO2715.1.

Plueddemann, A. J., and J. T. Farrar, 2006: Observations and models of the energy flux from the wind to mixed-layer inertial currents. *Deep-Sea Research Part II: Topical Studies in Oceanography*, **53 (1-2)**, 5–30, doi: 10.1016/j.dsr2.2005.10.017.

Pollard, R. T., 1970: On the generation by winds of inertial waves in the ocean. *Deep-Sea Research and Oceanographic Abstracts*, **17 (4)**, 795–812, doi:10.1016/0011-7471(70)90042-2.

Pollard, R. T., 1980: Properties of near-surface inertial oscillations. *Journal of Physical Oceanography*, **10 (March)**, 385–398, doi:10.1175/1520-0485(1980)010⟨0385:PONSIO⟩2.0.CO;2.

Pollard, R. T., and R. C. Millard, 1970: Comparison between observed and simulated wind-generated inertial oscillations. *Deep-Sea Research and Oceanographic Abstracts*, **17 (4)**, doi:10.1016/0011-7471(70)90043-4.

Prasad, T. G., and P. J. Hogan, 2007: Upper-ocean response to hurricane ivan in a 1/25Â° nested gulf of mexico hycom. *Journal of Geophysical Research: Oceans*, **112 (4)**, 1–18, doi:10.1029/2006JC003695.

Price, J. F., 1981: Upper ocean response to a hurricane. *Journal of Physical Oceanography*, **11 (2)**, 153–175, doi:10.1175/1520-0485(1981)011⟨0153:UORTAH⟩2.0.CO;2.

Price, J. F., 1983: Internal wave wake of a moving storm. Part I. scales, energy budget and observations. *Journal of Physical Oceanography*, **13 (6)**, 949–965, doi:10.1175/1520-0485(1983)013⟨0949:IWWOAM⟩2.0.CO;2.

Price, J. F., C. N. K. Mooers, and J. C. Van Leer, 1978: Observation and simulation of storm-induced mixed-layer deepening. *Journal of Physical Oceanography*, **8 (4)**, 582–599, doi:10.1175/1520-0485(1978)008⟨0582:OASOSI⟩2.0.CO;2.

Price, J. F., T. B. Sanford, and G. Z. Forristall, 1991: Ocean response to a hurricane, part ii: Data tabulations and numerical modeling. Tech. rep., Woods Hole Oceanographic Institution, Woods Hole.

Rimac, A., J. S. V. Storch, and C. Eden, 2016: The total energy flux leaving the ocean's mixed layer. *Journal of Physical Oceanography*, **16**, doi:10.1175/JPO-D-15-0115.1.

Rimac, A., J. S. Von Storch, C. Eden, and H. Haak, 2013: The influence of high-resolution wind stress field on the power input to near-inertial motions in the ocean. *Geophysical Research Letters*, **40 (18)**, 4882–4886, doi:10.1002/grl.50929.

Rotunno, R., and K. a. Emanuel, 1987: An air-sea interaction theory for tropical cyclones. Part II: Evolutionary study using a nonhydrostatic axisymmetric numerical model. *Journal of the Atmospheric Sciences*, **44 (3)**, 542–561, doi:10.1175/1520-0469(1987)044⟨0542:AAITFT⟩2.0.CO;2.

Saha, S., and Coauthors, 2010: NCEP Climate Forecast System Reanalysis (CFSR) selected hourly time-series products, January 1979 to December 2010. Research Data Archive at the National Center for Atmospheric Research, Computational and Information Systems Laboratory, Boulder, CO, doi:10.5065/D6513W89.

Sanford, T. B., P. G. Black, J. R. Haustein, J. W. Feeney, G. Z. Forristall, and J. F. Price, 1987: Ocean response to a hurricane. Part I: Observations. *Journal of Physical Oceanography*, **17 (November)**, 2065–2083, doi:10.1175/1520-0485(1987)017⟨2065:ORTAHP⟩2.0.CO;2.

Sanford, T. B., J. F. Price, and J. B. Girton, 2011: Upper-ocean response to hurricane frances (2004) observed by profiling em-apex floats *. *Journal of Physical Oceanography*, **41 (6)**, 1041–1056, doi:10.1175/2010JPO4313.1.

Sanford, T. B., J. F. Price, J. B. Girton, and D. C. Webb, 2007: Highly resolved observations and simulations of the ocean response to a hurricane. *Geophysical Research Letters*, **34 (13)**, 1–5, doi:10.1029/2007GL029679.

Schmidtko, S., G. C. Johnson, and J. M. Lyman, 2013: MIMOC: A global monthly isopycnal upper-ocean climatology with mixed layers. *Journal of Geophysical Research: Oceans*, **118 (4)**, 1658–1672, doi:10.1002/jgrc.20122.

Schubert, W. H., J. J. Hack, P. L. Silva Dias, and S. R. Fulton, 1980: Geostrophic adjustment in an axisymmetric vortex. *Journal of the Atmospheric Sciences*, **37 (7)**, 1464–1484, doi:10.1175/1520-0469(1980)037⟨1464:GAIAAV⟩2.0.CO;2.

Shay, L. K., P. G. Black, A. J. Mariano, J. D. Hawkins, and R. L. Elsberry, 1992: Upper ocean response to hurricane Gilbert. *Journal of Geophysical Research*, **97 (C12)**, 20 227, doi:10.1029/92JC01586.

Simmons, H. L., and M. H. Alford, 2012: Simulating the long-range swell of internal waves generated by ocean storms. *Oceanography*, **25 (2)**, 30–41, doi:10.5670/oceanog.2012.39.

Skyllingstad, E. D., W. D. Smyth, and G. B. Crawford, 2000: Resonant wind-driven mixing in the ocean boundary layer. *Journal of Physical Oceanography*, **30 (8)**, 1866–1890, doi:10.1175/1520-0485(2000)030⟨1866:RWDMIT⟩2.0.CO;2.

Stommel, H., 1948: The westward intensification of wind-drive ocean currents. *Transactions, American Geophysical Union*, **29 (2)**, 202–206.

Sutherland, B. R., 2010: *Internal Gravity Waves*. Cambridge University Press, Cambridge, UK, 394 pp.

Sverdrup, H. U., 1947: Wind-driven currents in a baroclinic ocean; with application to the equatorial currents of the eastern pacific. *Proceedings of the National Academy of Sciences of the United States of America*, **33 (11)**, 318–326, doi:10.1073/pnas.33.11.318.

Thorpe, S. A., 2005: *The Turbulent Ocean*. Cambridge University Press.

Tsai, Y., C.-S. Chern, J. Wang, and P. O. Box, 2008: The upper ocean response to a moving typhoon. *Journal of Oceanography*, **64 (January 2007)**, 115–130.

Voelker, G. S., P. G. Myers, B. R. Sutherland, and M. Walter, 2016: Oceanic internal gravity waves radiated after a cyclonic surface stress disturbance. *VIIIth International Symposium on Stratified Flows*, **1 (1)**.

Voelker, G. S., D. Olbers, M. Walter, C. Mertens, and P. G. Myers, 2017: Wind work and radiative near-inertial internal wave flux in a hybrid slab model, with application to the north atlantic. *Journal of Physical Oceanography (under review)*.

Watanabe, M., and T. Hibiya, 2002: Global estimates of the wind-induced energy flux to inertial motions in the surface mixed layer. *Geophysical Research Letters*, **29(8) (8)**, 1239, doi:10.1029/2001GL014422.

Weller, R. A., 1982: The relation of near-inertial motions observed in the mixed layer during the JASIN (1978) experiment to the local wind stress and to the quasi-geostrophic flow field. *Journal of Physical Oceanography*, **12 (10)**, 1122–1136, doi:10.1175/1520-0485(1982)012⟨1122:TRONIM⟩2.0.CO;2.

Whitt, D. B., and L. N. Thomas, 2015: Resonant generation and energetics of wind-forced near-inertial motions in a geostrophic flow. *Journal of Physical Oceanography*, **45 (1)**, 181–208, doi:10.1175/JPO-D-14-0168.1.

Wunsch, C., and R. Ferrari, 2004: Vertical mixing, energy, and the general circulation of the oceans. *Annual Review of Fluid Mechanics*, **36 (1)**, 281–314, doi:10.1146/annurev.fluid.36.050802.122121.

Young, W. R., and M. Ben Jelloul, 1997: Propagation of near-inertial oscillations through a geostrophic flow. *Journal of Marine Research*, **55 (4)**, 735–766, doi:10.1357/0022240973224283.

Zedler, S. E., 2009: Simulations of the ocean response to a hurricane: Nonlinear processes. *Journal of Physical Oceanography*, **39 (10)**, 2618–2634, doi:10.1175/2009JPO4062.1.

Zhai, X., 2015: Latitudinal dependence of wind-induced near-inertial energy. *Journal of Physical Oceanography*, **45 (12)**, 3025–3032, doi:10.1175/JPO-D-15-0166.1.